Collapsing Bubble Dynamics and Cavitation Inside Injectors for Fuel Mixtures

Raffaele Bellini

PhD Thesis

City St George's, University of London

School of Science & Technology

Mechanical Engineering & Aeronautics

Supervisor: Dr Ioannis Karathanasis

September 2025

Contents

List of Figures

List of Tables

Nomenclature

Abbreviations

ΔH_V Latent heat of vapourisation

C_a Contraction coefficient

C_d Discharge coefficient

c_p Specific heat at constant pressure

c_v Specific heat at constant volume

CO_2 Carbon Dioxide

VoF Volume of Fluid

CFD Computational Fluid Dynamics

DF Dual-fuel

DFICE Dual-fuel internal combustion engine

DNS Direct Numerical simulation

ECN Engine Combustion Network

EDEM **E**xperimentally validated **D**NS and L**E**S approaches for fuel injection, **m**ixing and combustion of dual-fuel engines

EoS Equation of State

HLLC Harten–Lax–van Leer contact

IB Immerse Boundary

ICE Internal Combustion Engine

LTS Local Time Step

Ma Mach number

MUSCL Monotonic Upstream-centered Scheme for Conservation Laws

NOx Nitric oxides

p Pressure

PC-SAFT Perturbed Chain Statistical Associating Fluid Theory

PPM Part Per Million

PR Peng-Robinson

Re Reynolds number

RK Runge-Kutta

RKPR Redlich-Kwong-Peng-Robinson

sat Saturation Condition

SOD Stand-Off Distance

SOI Start Of Injection

VCO Valve Covered Orifice

VLE Vapour Liquid Equilibrium

Greek symbols

δ Dimensionless density

$\delta_i j$ Kronecker symbol

μ Viscosity

ρ Density

τ Dimensionless temperature

τ_0 Rayleigh Collapse time

Latin symbols

α Vapour fraction

$\alpha(\delta, \tau)$ Dimensionless Helmholtz energy

α^0 Dimensionless Helmholtz energy of the ideal gas

α^r Dimensionless residual Helmholtz energy

$\vec{q}$ Vector of conserved variables

R_0 Initial Radius

c Speed of sound

d Blending coefficient

E Specific total Energy

e Specific internal Energy

F Vector of fluxes

h Specific enthalpy

J Joule

kg kilograms

m meter

R Ideal gas constant

s Specific entropy

T Temperature

u	velocity
Y	Mass fraction

Subscripts and Superscripts

0	Subscript - initial condition
0	Superscript - Ideal gas
face	Face of a cell
i	i-th component of a vector
j	j-th component of a vector
L	Left
l	Liquid
R	Right
r	residual
v	Vapour

Acknowledgements

First and foremost, I wish to express my deepest gratitude to my wife Elena, whose constant encouragement sustained me during the most difficult moments of my doctoral studies and throughout the preparation of this thesis. The vitality and positive energy you have shared since the first day we met have had a transformative impact on my life. The past eleven years have been a period of intensity and contrasting emotions, yet together we have faced every challenge and emerged stronger, ready to confront whatever lies ahead, forever.

I am profoundly grateful to my supervisor, Dr. Ioannis Karathanasis, for his trust, guidance, and motivation. His encouragement was invaluable at times when my determination faltered, and his reflections on life and friendship served as a reminder that we are more than scientists: we are human beings, with strengths and limitations alike.

I would also like to extend my sincere thanks to Dr Carlos Rodriguez, with whom I collaborated closely for three years, albeit mostly in a virtual setting due to distance and the constraints of the COVID-19 pandemic. His intellectual curiosity, knowledge, and determination to improve continuously made our work together both enriching and rewarding.

My appreciation is also due to my colleagues at City, St George's, University of London, and within the Marie Curie Project. Despite the difficulties created by the pandemic, we were nevertheless able to share valuable experiences that I shall remember with gratitude.

I am indebted to Professor Manolis Gavaises, Professor Federico Piscaglia, and all the staff at City, St George's, University of London, for their technical support, scientific discussions and for inspiring me to pursue research with

dedication, thereby helping me to grow as both a scholar and an individual.

I also owe much to my family and friends, whose support and good humour sustained me throughout these years. Without their presence, this journey would have been far less colourful and fulfilling.

Finally, I wish to acknowledge the countless individuals worldwide who selflessly share their knowledge and expertise for the benefit of others. Their generosity of spirit makes possible the advancement of research, the dissemination of knowledge, and indeed the very existence of the internet as a common resource.

Raffaele Bellini, London, September 2025.

Declaration

I hereby declare that the contents of this dissertation are original and have not been submitted in whole or in part for consideration for any other degree or qualification in this or any other university. This dissertation is my own work, except where specific reference is made to a joint effort in the text accordingly. I grant powers of discretion to the University Librarian to allow the thesis to be copied in whole or in part without further reference to me. This permission covers only single copies made for study purposes, subject to normal conditions of acknowledgement.

Raffaele Bellini, London, September 2025.

Thesis Contributions

In the development of this thesis, a new multiphase solver has been developed with the following attributes:

- **Real-fluid thermodynamics modelling**: The Perturbed Chain Statistical Associating Fluid Theory (PC-SAFT) EoS has been employed, and a unified methodology is presented, suitable for both subcritical and supercritical regimes without the need for any parameter tuning. The solver results have shown *very good agreement* with commercial software and experimental data.

- **Mach-consistent numerical flux**: The hybrid numerical flux proposed here has been implemented in OpenFOAM V7 and tested for several cases. The new flux is a combination of approximate Riemann solvers and previously proposed flux functions. It enables the use of the density-based solver even for flow regimes with Mach numbers on the order of $O(10^2)$. Its performance has been tested for bubble clusters as well as in-nozzle and spray regimes.

- **Local time stepping**: To prevent the overall simulation time step from being limited by the smallest length scale in high-aspect-ratio cells, a modified Local Time Stepping (LTS) methodology has been implemented in OpenFOAM V7. Its behaviour has been assessed in both in-nozzle and spray simulations.

- **Immersed Boundary Methodology**: The IB methodology has been implemented in OpenFOAM V7 within a new density-based solver to

simulate needle movement inside an injector. This methodology has been tested for in-nozzle and spray simulations.

- **Tabulated-data technique**: A robust technique has been implemented, where instead of solving the PC-SAFT EoS at each time step, its solution is stored in a preliminary step in a 3D table, with the input parameters being density, internal energy, and mass fraction. Thus, the numerical simulation itself becomes computationally more effective.

The solver is particularly suited for injector flows under high-pressure and high-temperature conditions. Validation has been performed on the benchmark Spray C cases, supported by an extensive cross-validated database. Ultimately, the proposed methodology delivers accuracy and robustness comparable to commercial software, without requiring parameter tuning.

Abstract

The alarming rise in global greenhouse gas concentrations poses a serious threat to the Earth's ecosystems and, as a consequence, many scientists worldwide are striving to combat climate change. However, implementing green transitions remains particularly challenging in certain sectors. For instance, no electrification strategies are currently available for medium- and large-scale Diesel engines. A partial substitution of Diesel with high-octane fuels represents the only practical and immediate solution. In particular, Dual-Fuel Internal Combustion Engines (DFICEs) have demonstrated significant reductions in soot and CO_2 emissions. Nonetheless, cavitation, and specifically cavitation-induced erosion, can be strongly influenced by fuel properties and operating conditions.

Current state-of-the-art studies on cavitation and cavitation-induced erosion often rely on simplified thermodynamic equations of state (EoS), such as barotropic EoS, which rarely account for thermal effects. This limitation may hinder accurate analysis, particularly when comparing fuels that are strongly influenced by thermodynamic properties. The present work addresses this gap by examining pressure peaks and thermal effects during the collapse of a vaporous cavitating cloud using real-fluid thermodynamics. The closure of the numerical framework is achieved through a structured table that linearly reconstructs the thermodynamic properties of the working fluid based on the PC-SAFT EoS. Compared to solving complex EoS directly or employing unstructured finite-element-based tables, this structured database proves more efficient, with search speed independent of the table resolution.

The tabulated EoS has been incorporated into an explicit density-based

solver within OpenFOAM V7. OpenFOAM (Open Source Field Operation And Manipulation) is a powerful, free, and open-source computational continuum mechanics (CCM) C++ toolbox that primarily focuses on Computational Fluid Dynamics (CFD). Given the broad range of velocity and sound-speed values encountered in such simulations, a Mach-consistent numerical flux capable of handling subsonic to supersonic flow conditions has been implemented.

For the first time, real-fluid thermodynamics have been applied to study both the collapse of vaporous bubble clusters and injector flow simulations. Particular attention is devoted to cavitation near walls, enabling the sampling of both pressure peaks and thermal effects. This work contributes to a deeper understanding of cavitation phenomena and highlights how fuel properties influence cavitation-induced erosion and jet quality in injectors.

Building on previous contributions [Fathi et al., 2022, Matheis and Hickel, 2017], we propose a numerical framework that incorporates a multiphase large-eddy Eulerian model combined with Peng-Robinson (RP) EoS/Redlich-Kwong-Peng-Robinson (RKPR) EoS and Vapour Liquid Equilibrium (VLE) calculations. Our extended framework integrates internal nozzle flow, spray development, cavitation, and needle dynamics. Key advancements include the incorporation of the PC-SAFT EoS, the VT-flash algorithm [Vidal et al., 2020], the IB Method [Stavropoulos Vasilakis et al., 2019], and entropy-scaling techniques into the flow solver. Importantly, this framework maintains a tuning-parameter-free approach, recognising the challenges associated with property measurements of novel fuel blends.

Implemented in the widely adopted open-source CFD solver OpenFOAM V7, this advanced modelling strategy ensures enhanced robustness and reliability. The solver has been tested and used for bubble collapse dynamics, where extreme gradients are in place, as well as for injector flows. The scope of the project referred to dual-fuel engines also owing to the overarching objectives set by the MSCA DN. However, given the high range of validation cases performed on this solver, we are confident that the solver could be applied to any jet/spray flow with high velocities, temperatures and or pressure, such as turbomachinery flows, flows in components of materialising thermo-

dynamic cycles, as well as other types of industrial nozzles, e.g. for spray cooling. The solver can work well for any kind of flow involving cavitation and high pressure or velocity gradients. And it is particularly suited for injector flows under high-pressure and high-temperature conditions. Validation has been performed on the benchmark Spray C and Spray D cases, supported by an extensive cross-validated database. Ultimately, the proposed methodology delivers accuracy and robustness comparable to commercial software, without requiring parameter tuning.

Chapter 1

Introduction

For most of history, the composition of the Earth's atmosphere remained relatively stable. In the mid-19th century, however, this trend changed. Historical and geological records show that CO_2 levels began to rise unusually rapidly. More precisely, CO_2 concentrations had remained between 275 ppm and 285 ppm for millennia; by the 1910s, they had reached 300 ppm. By 2020, the concentration had risen to 412 ppm, as shown in Fig. 1.1. Remarkably, within the span of a single century, a fundamental parameter of Earth's environmental stability increased at a rate approximately two orders of magnitude greater than the maximum variability observed over the preceding millennium.

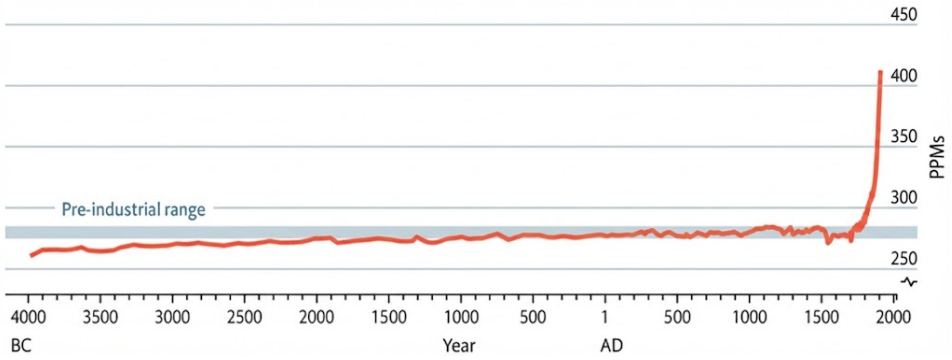

Figure 1.1: Global Atmospheric CO_2 concentration, parts per millions (PPMs) [*The Economist*, 2022].

Carbon dioxide constitutes a key greenhouse gas within Earth's climate system, primarily due to its strong absorption bands in the infrared spectrum. Terrestrial cooling occurs predominantly via the emission of longwave infrared radiation; however, elevated atmospheric CO_2 concentrations increase the op-

tical depth of the atmosphere, thereby reducing outgoing longwave radiation. This radiative forcing mechanism leads to a positive energy imbalance at the top of the atmosphere, ultimately driving an increase in global mean surface temperature. Indeed, the rise in CO_2, together with industrial and agricultural production and the release of other greenhouse gases such as methane, nitrous oxide, and industrial gases like chlorofluorocarbons and hydrochlorofluorocarbons, has increased the planet's average surface temperature by approximately 1.1℃–1.2℃ since the mid-19th century.

In 1992, when the CO_2 concentration had reached 356 ppm and evidence of anthropogenic warming was already discernible, all world leaders present at the UN Framework Convention on Climate Change committed themselves to the "stabilisation of greenhouse-gas concentrations in the atmosphere at a level that would prevent dangerous anthropogenic interference with the climate system"[United Nations, 1992]. This was to be achieved within a "time frame sufficient to allow ecosystems to adapt naturally to climate change, to ensure that food production is not threatened, and to enable economic development to proceed in a sustainable manner"[United Nations, 1992]. Today, however, scientists outline a range of possible scenarios if global society does not intervene promptly, as illustrated in Fig. 1.2.

In 2019, the scientific community signed a declaration ("World Scientists' Warning of a Climate Emergency" [Ripple, 2020]) warning of a climate emergency. They selected a number of vital planetary indicators to provide an objective outlook on the changes Earth is undergoing, which revealed concerning trends and very little effort by humanity over the last decades. In order to stop the surge of climate-related disasters since 2019, radical change is urgently needed. They observed that we may have already crossed the point of no return for the recovery of some critical Earth resources. A 2021 update to the 2019 climate emergency declaration [Ripple, 2021] focused on 31 vital planetary indicators (including greenhouse gases and temperature, rising sea levels, energy use, ice mass, ocean heat content, Amazon rainforest loss rate) and recent changes in them. Among these 31 indicators, 18 are reaching critical levels.

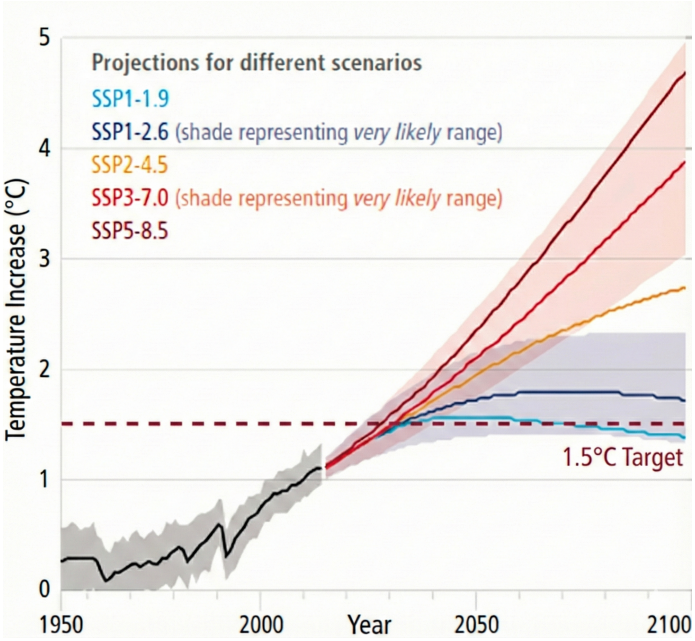

Figure 1.2: Climate change mitigation scenarios. Projected global mean temperature from 1950 to 2100 under different Shared Socioeconomic Pathways (SSPs): SSP1-1.9 ("very low greenhouse gas emissions"), SSP1-2.6 ("low emissions"), SSP2-4.5 ("intermediate emissions"), SSP3-7.0 ("high emissions"), and SSP5-8.5 ("very high emissions") [IPCC, 2022].

Recognising the need for an effective and progressive response to the urgent threat of climate change, in 2015 the Paris Agreement was signed by 196 parties, committing to limit global warming to below 2℃, preferably to 1.5℃ above pre-industrial levels. Following this line of thought, and considering economic, geopolitical, and social trends, the electrification of land, air, and marine vehicles is becoming increasingly urgent. However, this goal remains practically unattainable due to the constantly rising energy demands driven by urbanisation, population growth, and the ever-increasing transportation needs of developing economies. This is illustrated in Fig. 1.3, which shows global emissions by sector, with transport accounting for 16.2% of total emissions.

As visually explained in Fig. 1.3, considering transport emissions alone, 60% of road transport emissions (accounting for 11.9% of global emissions) come from passenger travel (cars, motorcycles, and buses), while the remaining 40% comes from road freight (lorries and trucks). This means that if the entire road transport sector were electrified and transitioned to a fully decarbonised electricity mix, global emissions would realistically be reduced by 11.9%.

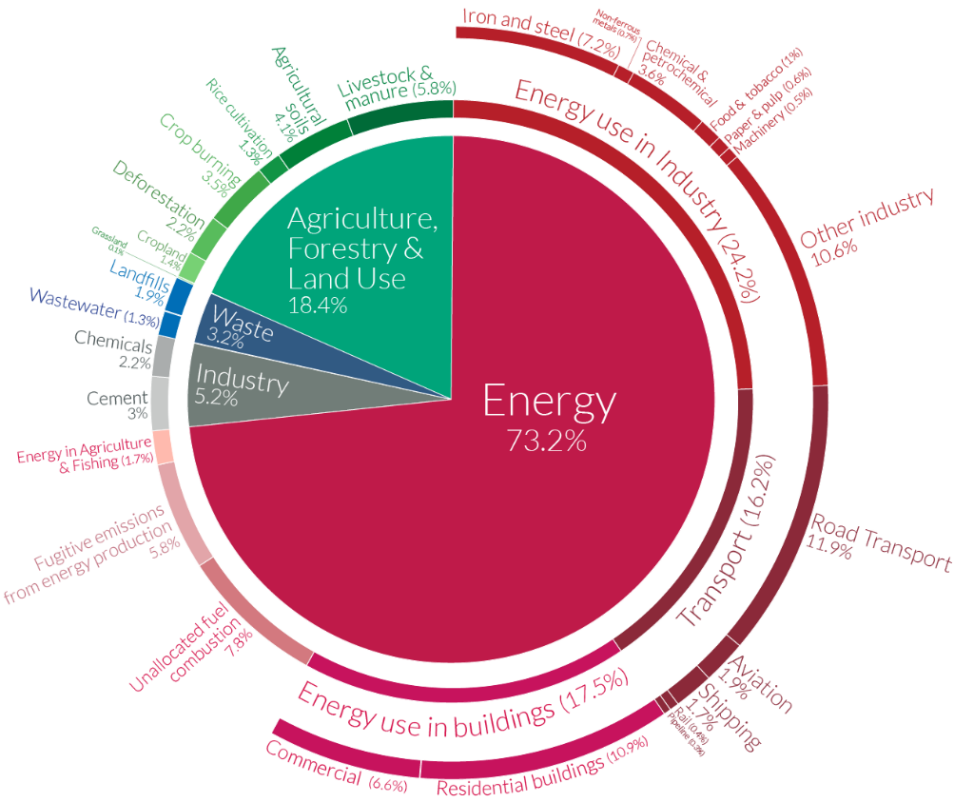

Figure 1.3: Global greenhouse gas emissions by sector. In 2016, total global greenhouse gas emissions amounted to 49.6 billion tonnes CO_2 equivalent [*Climate Watch - the World Research Institute*, 2022].

However, even if widespread efforts are made to scale up the production of electric vehicles, the use of medium- and large-scale Diesel Internal Combustion Engines (ICEs) will remain a reality, since no viable electrification strategy is currently in place for heavy-duty vehicles and marine vessels. As a consequence, hydrocarbon sources are expected to account for more than two-thirds of total energy usage over the next two decades [*Climate Watch - the World Research Institute*, 2022].

Currently, Diesel engines are responsible for approximately 30% of soot emissions and 17% of anthropogenic CO_2 emissions [*Climate Watch - the World Research Institute*, 2022]. Despite significant reductions achieved in recent decades, soot remains one of the deadliest forms of air pollution. To mitigate the inevitable environmental and health effects, partial substitution of conventional Diesel engines with high-octane liquid or gaseous fuels with a lower carbon-to-hydrogen ratio represents the only practical and immediate solution. The so-called Dual-Fuel Internal Combustion Engines (DFICEs) pri-

marily burn a premixed high-octane fuel/air mixture, or even hydrogen, while a moderate quantity of high-cetane fuel (pilot fuel) is used only as an ignition agent [Karimi et al., 2021].

As with conventional ICEs, the cost and time associated with the development of DFICEs—while pursuing high efficiency and long life cycles—can be effectively reduced by employing advanced simulation technologies. In particular, Computational Fluid Dynamics (CFD) tools can provide insights into dual-fuel injection and combustion phenomena, highlighting possible issues and facilitating improvements. In general, numerical methods can offer high-fidelity predictions in the design phase, reducing development efforts and costs.

To comply with regulatory standards and to reduce emissions, direct fuel injection has trended towards increased injection pressures in common-rail injection technologies, with many fuel-delivery systems exceeding 2000 bar [Ganser, 2000]. While these strategies contribute to emissions reduction, several critical issues remain. In particular, it is well known that cavitation-induced damage in fuel injectors, caused by elevated injection pressures, can affect performance and ultimately compromise the reliability of the engine after several thousand hours of operation [Tzanetakis et al., 2019, Moon et al., 2022], as well as considerably reducing the life cycle of powertrain components.

For this reason, this study focuses on cavitation and cavitation-induced erosion caused by high-pressure peaks in the vicinity of solid injector walls resulting from the collapse of vaporous (cavitation) clouds. Another objective of this investigation is to assess how cavitation affects the fuel jet exiting the injector orifices. Simulating both in-nozzle flow and jet evolution is a challenging task, as these processes involve a vast disparity of temporal and spatial scales [Brennen, 2013, Kim et al., 2014, Cervone et al., 2010]:

- High-velocity and cavitation phenomena inside the injector;
- The intact fuel jet at the injector exit;
- The formation of irregular liquid structures during primary atomization;
- The formation of finely atomised droplets at the end of secondary atom-

ization.

In accordance with the literature, the challenge in simulating in-nozzle flow and spray atomization simultaneously is indeed a multiscale problem. In simulation terms, "scales" refer to the differences in size (spatial) and time (temporal) between the smallest and largest events that must be calculated. In particular, to simulate cavitation, one must resolve microscopic vapor bubbles (micrometres in size). However, to simulate the spray, one must track the fuel moving several centimetres into the combustion chamber. If the simulation grid is sufficiently dense to resolve the bubbles, then discretising the entire spray chamber becomes prohibitively expensive. At the same time, cavitation bubbles collapse in microseconds (or even nanoseconds), while the full injection event might last milliseconds. Extremely small time steps (as low as nanoseconds) are required to capture the physics of cavitation, implying that millions of time steps are needed to simulate a fraction of a second of real time.

To capture this complex phenomenology, a dedicated in-house solver has been developed, incorporating the system's specific features and a Real-Fluid Thermodynamic model.

1.1 Thesis Objectives

This work is part of the "**E**xperimentally validated **D**NS and L**E**S approaches for fuel injection, **m**ixing and combustion of dual-fuel engines" (EDEM) Project Framework [*EDEM Projet*, 2019]. EDEM Project Framework funded this PhD, and, in particular, it aims to describe the cavitation of bubble clouds near solid walls for different fuels, as well as how cavitation-induced erosion affects both in-nozzle flow and the spray evolution of a fuel injector. It also seeks to develop a methodology for predicting pressure peaks and surface erosion in realistic geometries. It aims to accomplish the following three main objectives:

- To develop an algorithm capable of resolving the collapse of a single bubble as well as a cloud of bubbles.

- To validate the solver against experimental data and numerical databases for bubble dynamics and spray flows.
- To develop a numerical tool capable of providing insight and design guidelines for fuel delivery equipment in conventional and next-generation, multiple-fuel-powered powertrains.

More specifically, the envisaged outcome is a compressible, interface-capturing solver with real-fluid thermodynamics, capable of assessing cavitation in both bubble clusters and in-flow and spray simulations.

1.2 Thesis Outline

The thesis is structured as follows:

- **Chapter 2** provides a literature review on cavitation phenomenology and cavitation-induced erosion, with a particular focus on fuel injectors.
- **Chapter 3** outlines the methodology, numerical schemes, and thermodynamic closure for both single- and multiphase flows.
- **Chapter 4** presents detailed results for single-component cases. Four case studies are investigated: validation against the Riemann problem; validation against the Rayleigh-Plesset equation; validation against published data for a single bubble near a solid wall at different stand-off distances (S0D); and a cluster of bubbles near a solid wall. Finally, a comparative study of dodecane and two short-chain alcohols is performed.
- **Chapter 5** presents an in-depth analysis of multi-component mixtures, where the implemented methodology is validated against Engine Combustion Network (ECN) data for the Spray-C configuration, featuring fully cavitating multi-hole orifices.
- **Chapter 6** concludes with the findings of the simulations, highlights the novelty of the present work, and provides an overview of publications and future research directions.

Chapter 2

Literature Review

Understanding and controlling cavitation and its consequences remains a challenge, as, in most technical applications (apart from specific biomedical applications), it is an undesirable phenomenon, and the objective is to minimise its effects when it cannot be avoided altogether. Cavitation-induced erosion causes material loss and degrades hydraulic systems, such as pumps, turbines, injectors, and ship propellers. Therefore, prediction and control of cavitation and induced erosion are fundamental in the design of any hydraulic system, including injectors [Piehl and Bravo, 2018], propellers, or rocket engines [Dular and Petkovsek, 2018].

As explained in the following sections, cavitation inside an injector also affects spray atomization. This poses a real challenge both for experiments and simulations. In fact, studying nozzle cavitation and spray atomization simultaneously can be regarded as a multiscale problem. Scales refer to the differences in size (spatial) and time (temporal) between the smallest and largest events that must be calculated. In particular, to simulate cavitation, microscopic vapour bubbles (micrometres in size) must be resolved. However, to simulate the spray, the fuel transported several centimetres into the combustion chamber must be tracked. If the simulation grid is sufficiently dense to resolve the bubbles, it becomes computationally too expensive to cover the entire spray chamber. At the same time, cavitation bubbles collapse in microseconds (or even nanoseconds), while the full injection event might last for milliseconds.

Tiny time-steps have to employed (as low as ns) to capture the physics of cavitation, meaning millions of time steps are needed just to simulate a fraction of a second of real time. Similar comments could be made for experimental analysis.

As a consequence, cavitation constitutes a complex phenomenon which cannot be fully elucidated across scales solely by employing experimental or numerical means. For these reasons, this Ph.D. project focuses mainly on two aspects of cavitation:

- **Small-scale cavitation**, where the focus is on a cloud of bubbles collapsing close to a solid boundary.
- **Full-scale cavitation**, where the focus is on how cavitation influences fuel delivery in an injector device.

2.1 Cavitation Fundamentals

Cavitation can be generally defined as the generation of vapour within a liquid medium due to a drop of the static pressure below the vapour pressure [Franc and Michel, 2005]. Fig. 2.1 gives a schematic $P_v - T$ diagram, which helps in understanding this behaviour.

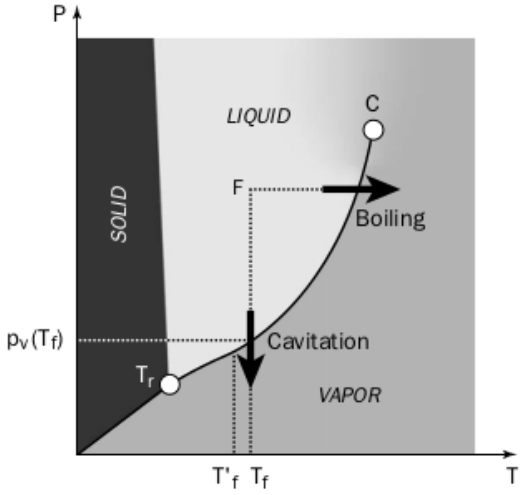

Figure 2.1: $P_v - T$ diagram for a general substance with emphasis on the cavitation and boiling processes [Franc and Michel, 2005].

For any specific substance, the stable liquid and vapour states are separated

by the coexistence line, which connects the triple point (Point T_r in Fig. 2.1) with the critical point (Point C in Fig. 2.1) [Brennen, 2005]. Two different thermodynamic changes of state can be defined, leading to the evaporation of a liquid:

- **Boiling**: when the temperature T of a liquid is increased at approximately constant pressure, vapour forms as soon as T is equal to the saturation temperature $T_{sat,v}$.
- **Cavitation**: when the pressure p in a liquid is decreased at approximately constant temperature, evaporation takes place as soon as p is equal to the saturation pressure $p_{sat,v}$.

Following this, when cavitation occurs, an isothermal transformation can be assumed (arrow pointing downward in Fig. 2.1) as the surrounding liquid shows only a minor temperature change. However, in reality, the process is associated with heat transfer, and a non-isothermal phase change occurs. In cavitation, the difference $T_f - T'_f$ is called the thermal delay and, overall, it corresponds to a reduction in temperature. This is because the surrounding liquid temperature decreases as the liquid behaves like a heat source to complete the vapourisation process. In order to resolve this behaviour, the energy balance must be taken into account in the modelling strategy.

In general, two distinct broad categories of cavitation dynamics exist:

- **Hydrodynamic cavitation**: moderate convective accelerations in liquid flows can result in strong "negative pressure" gradients or tensions, forcing the liquid to evaporate [Young, 1999].
- **Acoustic cavitation**: an oscillating pressure field or a moving expansion wave in static or nearly static liquid can cause the liquid to evaporate [Young, 1999].

In both types of cavitation, the driving mechanism is the drop of the local pressure below a threshold value at which liquid cohesion is no longer possible. This threshold value is the vapour pressure ($p_{sat,v}$) of the liquid at the given temperature. Therefore, the liquid immediately vapourises.

However, deviations from this value are possible, and the actual cavitation inception depends on various parameters such as fluid quality or initial gas content (which is unavoidable in systems such as fuel injectors). On the other hand, developed cavitation refers to a continuous, steady or unsteady cavity with a significant effect on the flow dynamics and performance of flow devices.

In general, evaporation is usually followed by condensation, which occurs when the ambient pressure rises or when vapour structures are transported to areas of higher static pressure due to the surrounding flow field. If the pressure difference between the vapour structures and the surrounding liquid is sufficiently high, condensation occurs as a form of implosion or collapse. Specifically, the collapse of vapour structures generates shock waves, which can excite vibration modes of structures [Brennen, 2013, Franc and Michel, 2005], or, in a more detrimental manner, if the collapse occurs near solid boundaries, it can lead to damage of surface material [Brennen, 1994, Arndt, 1981].

2.1.1 Collapse Dynamics of Cavitation Bubbles

A distinct feature of cavitating flows is the disruptive re-condensation (in the form of collapse) when vapour structures are advected into regions of higher static pressure, which compresses the vapour bubble until it implodes. When the pressure in the liquid exceeds the vapour pressure, condensation of the vapour begins at the phase boundary. The specific liquid density is usually several orders of magnitude greater than the specific vapour density for a given fluid. For this reason, the condensation of vapour results in an acceleration of the surrounding liquid.

A primary sketch illustrating the collapse mechanism, the consequent shock formation, and the associated cavitation-induced erosion effects is shown in Fig. 2.2 [Sezal, 2009].

Assuming a pure vapour bubble already exists in a flow domain, when a pressure imbalance occurs between the bubble and the surrounding liquid ($p_{\text{bubble}} \ll p_{\text{liquid}}$, as the bubble constitutes only a portion of the domain), it begins to shrink and eventually collapses. This mechanism is analogous to the

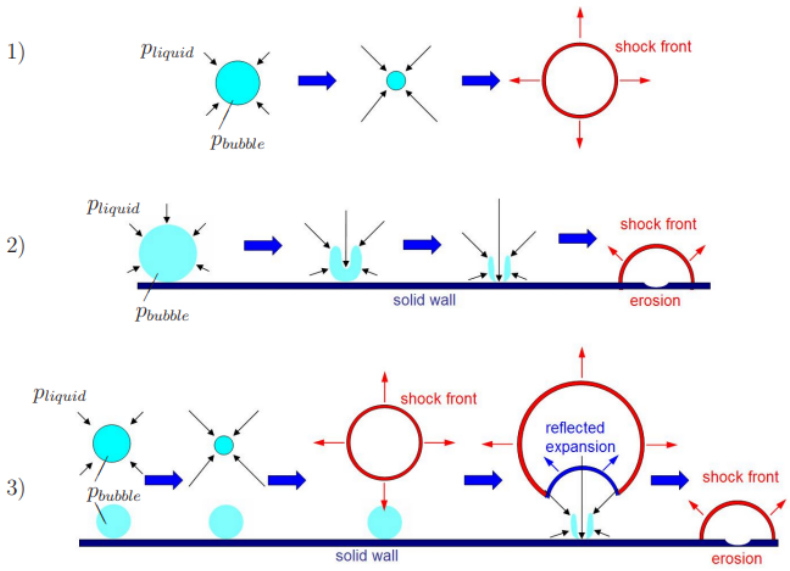

Figure 2.2: Representation of the collapse of a pure vapour bubble with $p_{\text{bubble}} \ll p_{\text{liquid}}$ at different distances from a wall: 1) isolated bubble, 2) bubble close to a solid surface, 3) interaction of two bubbles collapsing near a wall [Sezal, 2009].

water hammer problem [Franc and Michel, 2005], as the convective acceleration of the bubble surface during collapse drives liquid towards the centre of the bubble. When the bubble collapses completely, the resulting collision of the liquid at the centre generates a shock that propagates into the surrounding liquid [Plesset and Chapman, 1970].

Fig. 2.2 illustrates three different bubble collapse cases depending on the environment surrounding the bubble, which can be summarised as follows:

- Collapse of an isolated bubble resulting in a symmetrical shock front (Fig. 2.2a). The imposed pressure difference causes the bubble to shrink until it collapses completely, forming a shock wave that propagates symmetrically into the surrounding liquid. The liquid is accelerated towards the centre of the bubble uniformly. Once all vapour has condensed, the inertia of the liquid leads to the formation of a spherical shock wave originating from the collapse centre.

- Collapse of a bubble close to a solid surface and the resulting asymmetrical shock front (Fig. 2.2b). In this case, the wall restricts the acceleration of the liquid, inducing an asymmetrical collapse. One side of the bubble accelerates inward more rapidly than the side facing the

wall, generating a liquid re-entrant micro-jet that penetrates the bubble. The speed of this micro-jet is much higher than in the isolated bubble case. Combined with the collapse mechanism described above, a more intense shock forms at the surface and propagates into the surrounding flow. This highly localised, high-amplitude pressure increase at the solid surface due to the shock waves and micro-jet can result in material damage or erosion [Philipp and Lauterborn, 1998].

- Interaction of an isolated bubble collapse in the vicinity of another bubble near a solid surface and the reaction/interaction of the shock fronts (Fig. 2.2c). Here, the isolated bubble collapses, and its shock wave interacts with the bubble close to the wall. The interaction between different collapses further demonstrates how asymmetry in the problem produces micro-jets and shock waves impacting the wall [Philipp and Lauterborn, 1998].

More specifically, the flow field surrounding the bubble has an impact on the bubble shape during the recondensation process. The collapse sequence depends on the bubble's distance from the wall, known as the Stand-Off Distance (SOD). It is defined as the ratio of the bubble radius to its distance from the wall: SOD $= R_0/h$, where R_0 is the bubble radius and h is the distance from the bubble centre to the wall. A SOD of 0 indicates that the bubble centre lies on the wall, while a SOD > 1 indicates that the bubble is detached from the wall. Finally, SOD < 0 indicates that the bubble centre is below the wall.

Fig. 2.3a analyses the scenario in which SOD=0, meaning that the bubble's centre is exactly on the wall. In this case, the collapse resembles that of an isolated bubble, where the bubble uniformly shrinks until it collapses and the shock waves propagate symmetrically. This is due to the perfectly symmetrical pressure field surrounding the bubble.

In the case of SOD<0, which is the case when the bubble centre is below the wall, the wall is pinched at its maximum expansion in the circumferential direction, resulting in a mushroom shape [Lauer et al., 2012, Shima, 1997]

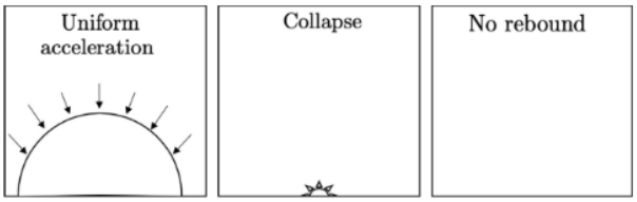

(a) $SOD = 0$

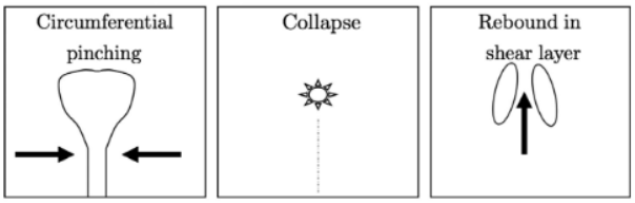

(b) $SOD < 0$

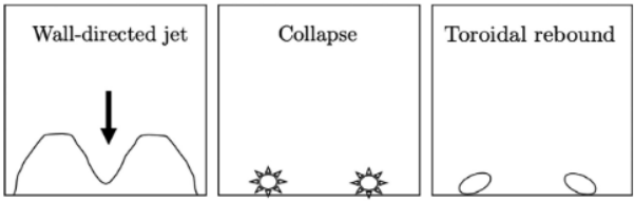

(c) $SOD > 0$

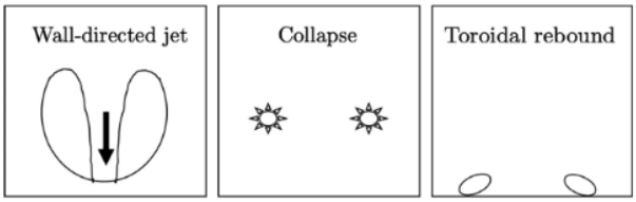

(d) $SOD > R_0$

Figure 2.3: Sketch of the collapse behavior of wall-attached bubbles with (a) bubble centre located on the wall (SOD=0), (b) bubble centre below the wall (SOD<0),(c) bubble centre above the wall (SOD>0), and (d) a wall-detached bubble (SOD>1). SOD is defined as the ratio of the bubble radius to its distance from the wall: SOD = R_0/h, where R_0 is the bubble radius and h is the distance from the bubble centre to the wall. [Trummler et al., 2021]

(Fig. 2.3b). The radially inward-directed flow reaches very high velocities, and the subsequent collision of these inward-moving liquid fronts induces a high-pressure peak. Shortly afterwards, the remaining upper part collapses and emits a pressure wave, weaker compared to the previous one.

In the last two cases, shown in Fig. 2.3c and 2.3d, a wall-directed jet forms during the initial collapse phase, resulting in a toroidal bubble. As the SOD increases, the bubble becomes more elongated in the wall-normal direction [Lauterborn and Ohl, 1998]. When the jet hits the wall, it induces a pressure peak and then moves radially outwards along the wall, pushing

the vapour away. Consequently, the remaining torus is compressed from inside and outside. Compression from the outside is then halted, causing an outward-propagating pressure wave and a first ring-shaped pressure impact on the wall. Subsequently, the collapse of the torus becomes increasingly non-uniform, with a portion near the wall being pinched away from the main torus [Lindau and Lauterborn, 2003, Trummler et al., 2020]. At later time steps, the bubble fragments into an inner bulged part and an outer pinched-away section. The inner part collapses first, emitting a pulse that travels radially inward, collides at the centre, and continues in the opposite direction. The collapse of the inner torus induces the largest wall pressure. Then, the outer torus collapses, emitting a less intense pressure wave propagating radially outwards. The main difference between the cases shown in Fig. 2.3c and 2.3d is that in the first case, the first collapse happens at the wall, since the bubble is attached to the wall. On the contrary, when SOD>1, the first collapse happens far from the wall. In any case, the rebound collapse will happen close to the wall for both cases.

2.1.2 Forms of Cavitation Structures

Once cavitation starts to develop, it can take different forms depending on the geometric shape of the surrounding environment, fluid quality and properties, and other external factors. To begin with, cavitation strongly depends on the non-cavitating flow field and, as it develops, on the interaction of vapour structures and main flow patterns. The basic types of cavitating flows can be categorised as follows [Franc and Michel, 2005]:

- **Bubble cavitation** (Fig. 2.4a): This type of cavitating flow consists of a small number of large vapourous bubbles in regions of low pressure, resulting from the rapid growth of initially present air nuclei. The bubbles are carried along with the flow until they collapse and disappear as they enter areas of higher pressure. Here, the dissolved gas content of the flow plays a crucial role in the quantity and topology of the bubbles.
- **Sheet cavitation** (Fig. 2.4b): These cavities are often formed in the

vicinity of the leading edge of wing-type bodies.

- **Cloud cavitation** (Fig. 2.4b): This cavitation regime consists of many small bubbles associated with intermediate pressure levels. It usually occurs when a partial or sheet cavity oscillates in length and periodically sheds clouds of vapour structures.

- **Super-cavitation** (Fig. 2.4c): As the velocity surrounding the object increases, the sheet cavity attached to the body grows and starts to enclose a larger part of the body.

- **Vortex cavitation** (Fig. 2.4d): Rotational structures generate low-pressure regions such as vortex cores or turbulent wakes inside the flow field. Such pressure drops can result in evaporation of the liquid and thus cavitation. In general, the characteristics of the vortex cavity depend on how the vortex is generated in the single-phase region.

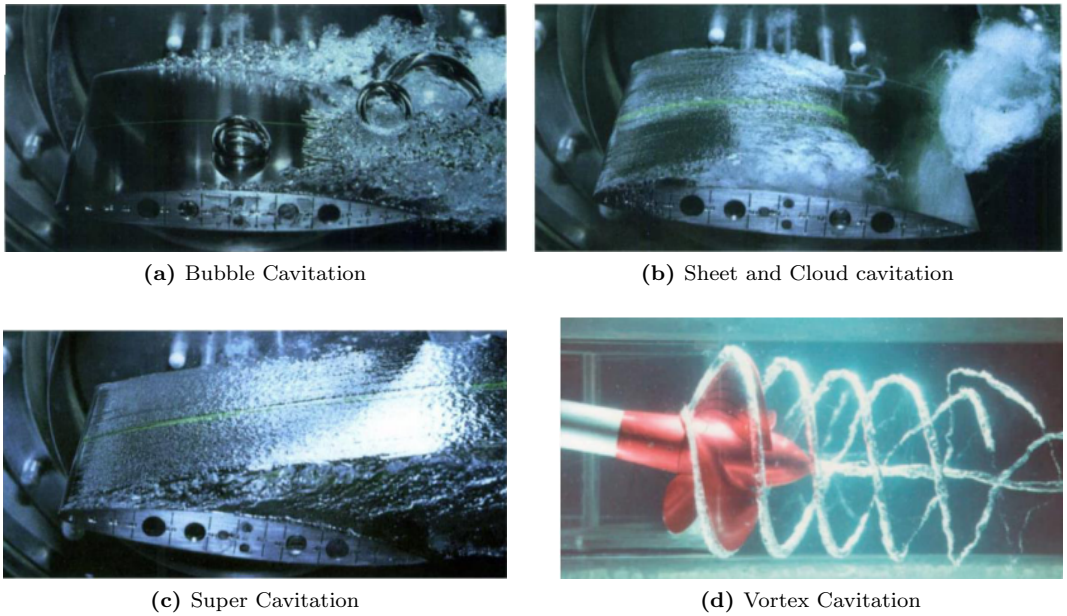

(a) Bubble Cavitation

(b) Sheet and Cloud cavitation

(c) Super Cavitation

(d) Vortex Cavitation

Figure 2.4: Cavitating flow around a *NACA16 012* hydrofoil under different flow conditions and angles of attack (a), (b), (c) [Franc and Michel, 1985], and vortex cavitation at a ship propeller at model scale (d) [Arndt, 2002].

It should be noted that, in the literature, except vortex cavitation, it is often not possible to have a clear distinction between cavitation regimes (as is clearly visible in Fig. 2.5, which shows cavitation inside an injector orifice).

In particular, the transition between cloud and bubble cavitation is not well-defined, and most sheet cavitation events are coupled with cloud cavitation and cloud-shedding structures.

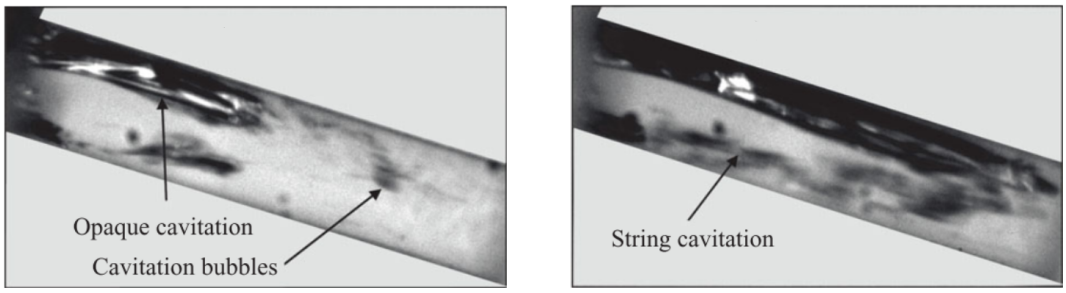

(a) Incipient cavitation **(b)** Fully developed cavitation

Figure 2.5: Vapour distribution inside an injector nozzle at different stages of cavitation development [Sun et al., 2019].

Another important effect of cavitation in hydraulic systems is related to the growth and collapse of vapour, which alters the flow characteristics, particularly the pressure field in wall-bounded flows. These effects can be summarised as follows [Sun et al., 2019]:

- Reduced performance of the system or device due to operation under off-design conditions.
- Generation of noise and vibration.
- Instantaneous pressure loads on the body resulting from bubble-collapse-induced shocks, which may ultimately lead to erosion of solid surfaces.

2.1.3 Theoretical Studies Bubble Collapse

Past research focused in sheding light on the tension characteristics of liquids, and hence on cavitation inception, through theoretical and experimental studies. The first theoretical formulations on single-bubble dynamics were introduced by Besant [Besant, 1859]. His studies focused on the motion of an empty spherical bubble in an incompressible and inviscid liquid, for which he predicted the pressure field in the liquid and the collapse time of the empty bubble. Subsequently, Rayleigh [Rayleigh, 1917] studied the same flow process

theoretically and derived an analytical formulation describing it. Later, Plesset [Plesset and Chapman, 1970] modified the equation derived by Rayleigh to include surface tension and viscous effects. The resulting equation is known as the "Rayleigh-Plesset Equation" [Plesset and Chapman, 1970] (refer to Eq. 2.1) and describes the growth and collapse of a spherical bubble under the effect of a surrounding pressure field, filled with the vapour of the surrounding liquid (treated as an incompressible fluid, i.e. $\rho_{liq} = const$) and a non-condensable gas content.

Eq. 2.1 describes the temporal evolution of the bubble radius R, where $\dot{R}$ is the bubble radius rate of change and $\ddot{R}$ its acceleration.

$$R\ddot{R} + \frac{3}{2}\dot{R}^2 = \frac{p_{sat} - p_{\inf}(t)}{\rho_{liq}} + \frac{p_{g0}}{\rho_{liq}}\left(\frac{R_0}{R}\right)^{3k} - \frac{2S}{\rho_{liq}R} - 4\nu_{liq}\frac{\dot{R}}{R} \tag{2.1}$$

The two terms of the left-hand side of Eq. 2.1 represent the inertia of the surrounding liquid as it accelerates or decelerates due to the changing bubble radius.

The terms on the right-hand side of Eq. 2.1 represent:

- The first term represents the driving force, which is the net difference between the pressure inside the bubble (P_{sat}) and the pressure far from the bubble (P_∞), which is the surrounding liquid pressure as a function of time, and ρ_{liq} is the liquid density.

- The second term accounts for the non-condensable gas content inside the bubble, where p_{g0} is the initial gas pressure, R_0 is the initial bubble radius, and k is the polytropic constant of the gas.

- The third term represents the surface tension S of the liquid.

- The fourth term describes the effect of the liquid viscosity ν_{liq}.

The Rayleigh-Plesset Equation is commonly used to analyse the behaviour of bubbles under different conditions. Generally, this equation is solved numerically and subsequently used to validate simulations of a single bubble collapsing far from walls.

In 1980, Keller and Miksis [Keller and Miksis, 1980] extended the Rayleigh-Plesset equation to include acoustic considerations, taking into account not only the influence of vapour pressure inside the cavitation bubble, liquid viscosity, and surface tension, but also acoustic radiation effects and the compressibility of the liquid. Additionally, they introduced a delay time term of $t + R/c$ during the cavitation bubble collapse process, resulting in the so-called Keller–Miksis model, with the relevant equation expressed in 2.2.

$$\ddot{R}R(\dot{R} - c) = \frac{1}{2}\dot{R}^3 + \dot{R}\frac{p_{sat} - p_{\inf}(t)}{\rho_{liq}} - c\left(\frac{3}{2}\dot{R}^2 - \frac{p_{sat} - p_{\inf}(t)}{\rho_{liq}}\right) + R\dot{R}\frac{p_{sat} - p_{\inf}(t)}{\rho_{liq}} + 2\left(1 + \frac{\dot{R}}{c}\right)\left(t + \frac{R}{c}\right) \tag{2.2}$$

Where c represents the speed of sound. In general, the Keller–Miksis equation expands on the Rayleigh–Plesset equation by incorporating the compressibility of the surrounding liquid and acoustic radiation effects, making it more suitable for modelling cavitation phenomena with larger bubble oscillations and higher acoustic pressures. The Rayleigh–Plesset equation, on the other hand, assumes an incompressible liquid and is often used for smaller-amplitude oscillations.

For the cases studied in this thesis, the two equations provide identical results. Indeed, considering pure Dodecane at the specific initial conditions shown in Table 2.1, Fig. 2.6 shows that the two equations behave in the same way.

Variable	Vapour Condition	Liquid Condition
ρ	$0.0015\,\mathrm{kg/m^3}$	$744.36\,\mathrm{kg/m^3}$
e	$-142\,760\,\mathrm{J/kg}$	$-488\,540\,\mathrm{J/kg}$
p	$19.64\,\mathrm{Pa}$	$101\,325\,\mathrm{Pa}$

Table 2.1: Initial conditions for the Rayleigh-Plesset and Keller-Miksis equations.

The initial conditions, including the initial radius, have been chosen following the work of [Trummler et al., 2021].

According to the theory [Franc and Michel, 2005], the bubble collapse ve-

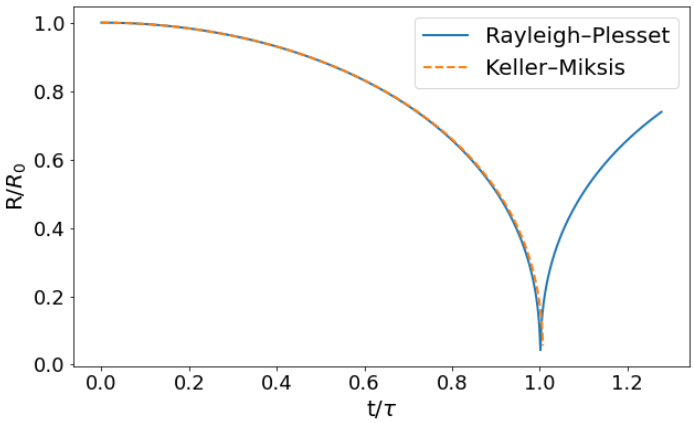

Figure 2.6: Comparison between the Rayleigh-Plesset and Keller-Miksis equations

locity can be approximated by Eq. 2.3.

$$\frac{dR}{dt} = -\sqrt{\frac{2}{3}\frac{p_{\text{inf}} - p_{vap}}{\rho_{liq}}\left[\left(\frac{R_0}{R}\right)^3 - 1\right]} \tag{2.3}$$

Then the characteristic Rayleigh collapse time τ_0, which can be defined as the time a bubble needs to collapse, or more in general to reach its minimum volume, under specific conditions, is defined by Eq. 2.4.

$$\tau_0 = 0.915 R_0 \sqrt{\frac{\rho_{liq}}{p_{\text{inf}} - p_{vap}}} \tag{2.4}$$

In Fig. 2.6, the radius has been normalised by the initial bubble radius, $R_0 = 400\mu$m, and the time has been non-dimensionalised by dividing it by the Rayleigh time, τ_0. Therefore, it is reasonable to use the Rayleigh–Plesset equation for the validation of the code presented in this manuscript.

2.1.4 Collapse Dynamics in Experimental Studies

Experimental studies of cavitating flows can be divided into two categories:

- Single or multiple bubble dynamics, where experiments focus on analysing bubble growth, collapse, and interaction mechanisms.
- Flow applications, where the focus is on the hydrodynamic cavitation topology and on how cavitation clouds are generated and affect the flow

field.

The collapse mechanism of a single isolated bubble has been extensively studied through experimental investigations, demonstrating how violent shock structures develop during the collapse of both individual bubbles and bubble clouds [Gilmore, 1952]. A notable example of an experimental study showing the collapse of a single isolated bubble was conducted by Lauterborn [Lauterborn and Ohl, 1998], as illustrated in Fig. 2.7.

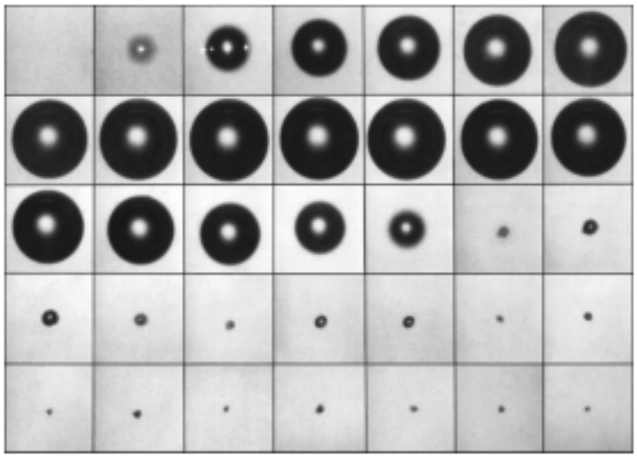

Figure 2.7: Growth and collapse evolution of an isolated spherical bubble initiated by a laser pulse in water. The bubble contains water vapour and non-condensable gas [Lauterborn and Ohl, 1998].

The sequence of high-speed images illustrates the production of a spherical bubble (generated using a laser pulse), its growth, and subsequent collapse. The bubble contains water vapour and non-condensable gas, initially dissolved in the water. The bubble reaches its maximum size before the pressure field imposed by the surrounding liquid forces it to shrink and eventually collapse. In this case, however, the bubble does not collapse completely due to the presence of the trapped non-condensable gas, resulting in subsequent growth and weakened collapses, as if the bubble is rebounding [Lauterborn and Ohl, 1998].

Another notable investigation was conducted by Philipp [Philipp and Lauterborn, 2000, 1998], where the authors focused on bubble collapse near a solid wall (Fig. 2.8). In this experiment, the vapour bubble was again initiated using a laser pulse and, similar to the previous case, contained some non-condensable

gas initially dissolved in the water. While the bubble's growth behaviour is similar to the previous case, the collapse characteristics are influenced by the presence of the wall, following the patterns illustrated in Figs. 2.2 and 2.3.

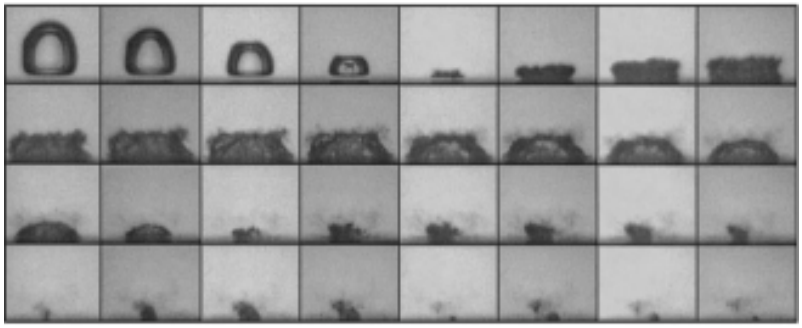

(a) Collapse evolution of a bubble near a solid surface.

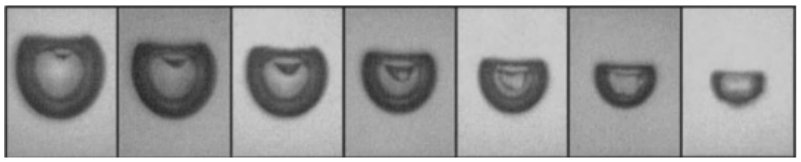

(b) Focus on the bubble collapse evolution in the vicinity of the solid surface; here the re-entrant jet is clearly visible.

Figure 2.8: Collapse of a bubble close to a solid surface. The bubble contains water vapour and non-condensable gas [Philipp and Lauterborn, 2000][Philipp and Lauterborn, 1998][Yunfei et al., 2018].

As previously described, during the collapse, the bubble interface near the wall flattens while the opposite side is pierced. Consequently, a re-entrant jet forms, directed towards the solid wall, and eventually impinges upon it. Due to the high velocity of the re-entrant jet, a shock wave is generated and propagates through the liquid. As a result, the solid surface experiences a strong pressure load (from both the re-entrant jet and the shock wave), which is widely considered a plausible mechanism for cavitation-induced erosion.

As one might expect, experiments specifically on clusters of bubbles are relatively rare, as they are difficult to replicate and introduce significant complexities in both setup and analysis.

The second class of experimental investigations focuses on cavitation in hydrodynamic applications, with emphasis on injection nozzles in high-pressure systems such as fuel-delivery equipment. Cavitation in injection systems is particularly challenging and complex to observe due to the small scale of the nozzle, which is very hard to access without modifying the flow characteristics.

Observations in larger-scale nozzles have demonstrated the presence of cavitation bubbles and bubble clouds [Sato and Saito, 2001, Chaves et al., 1995, Piehl and Bravo, 2018].

Many authors have noted the presence of shedding cavitation regions and that unsteady behaviour [Schmidt et al., 1999] may arise in injectors. Chaves et al. also concluded that it is difficult to identify the precise structure of the cavitating flow, whether it is sheet-type cavitation or cloud cavitation [Chaves et al., 1995]. Other investigations have confirmed that different types of cavitation structures can occur simultaneously inside the nozzle [Martynov, 2005].

Current injector systems for modern Diesel, gasoline, and Dual-Fuel engines operate under pressure differences ($\Delta p = p_{in} - p_{out}$) up to 2000 bar, with characteristic time scales for the relevant flow processes of $\Delta\tau \leq 10^{-4}$ s. Under such conditions, cavitation is unavoidable. Moreover, cavitation has a strong effect on spray formation and atomisation, as the geometry of the injector may be significantly affected by erosion (Figs. 2.10 and 2.11), which in turn influences combustion efficiency [Young, 1999]. It has also been shown that super-cavitation and turbulence induce disturbances that promote atomisation at the nozzle exit [Chaves et al., 1995, Sun et al., 2019]. For these reasons, controlling cavitation in injection nozzles is critical to maintain the injector system at its optimal performance. For instance, employing swirling flow can stabilise cavitation regions and shift them away from solid walls, thereby mitigating erosion concerns.

Focusing on cavitating flow inside an injector, it is well established that it significantly affects the resulting spray characteristics [He et al., 2016]. Other studies have provided quantitative insights into cavitation in fuel injector nozzles. For example, Chaves et al. [Chaves et al., 1995] and He et al. [He et al., 2013] observed that as injection pressure increases, the cavitation region lengthens. When it reaches the nozzle exit, the flow enters the Super-cavitation regime. The liquid jet is now partially or fully surrounded by vapor as it leaves the hole. In particular, they observed that the Discharge Coefficient C_d stops behaving like a liquid flow variable and it collapses to a constant value and will

not change even if you increase the injection pressure further. The flow is now "choked"—mass flow only increases because of higher density/velocity, not because of better flow efficiency. Moreover, if the cavitation bubbles reach the exit and collapse immediately upon hitting the high-pressure air of the cylinder, they create violent microscopic shockwaves. These shockwaves "shred" the liquid jet from the inside out causing a dramatically increases the Spray Cone Angle and reduces droplet size. The spray looks "bushy" and wide.

Generally, the sudden contraction of the cross-section leading into the orifice and the abrupt change in flow direction (due to pressure gradients) cause the boundary layer to separate from the nozzle wall, creating the vena-contracta. Between the vena-contracta and the orifice wall, a recirculation flow is observed [Bergwerk, 1959]. In this recirculation zone, local pressure decreases due to flow centrifugation. Once the pressure drops below the saturation pressure, the liquid vaporises and cavitation forms, as depicted schematically in Fig. 2.9.

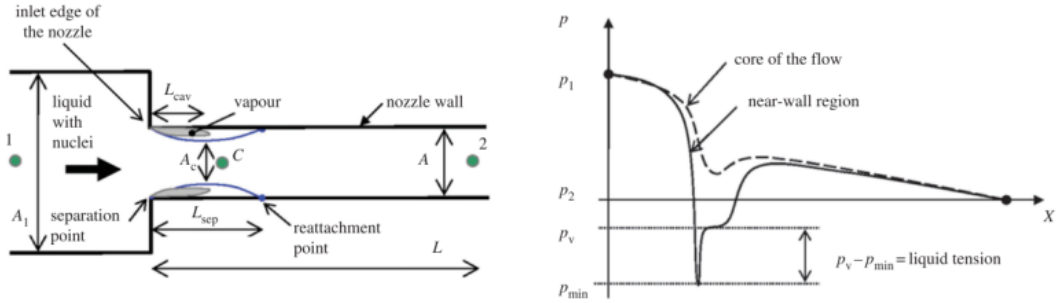

(a) Cavitation formation inside a nozzle **(b)** Pressure evolution inside a nozzle

Figure 2.9: Sketch of cavitation formation and pressure evolution inside an injector [Ferrari, 2017].

The strong decrease in pressure near the solid wall leads to the formation of cavitation, as the local pressure drops below the saturation pressure. Further along the streamline, the fluid reattaches to the nozzle wall, and a boundary layer gradually develops from the reattachment point to the nozzle exit. Downstream of the separation point, the lost pressure is partially recovered; however, wall friction continues to cause a substantial pressure reduction in the subsequent section of the straight nozzle.

Even though cloud cavitation only occurs in a small region of particularly

low ambient pressure, its presence significantly alters the spray characteristics and enhances the primary breakup of the resulting spray. It has been verified that finite jet disturbances due to cloud cavitation and turbulence within the nozzle initiate atomisation immediately at the nozzle exit [Yuan and Schnerr, 2003]. The liquid jet near the nozzle exit depends primarily on the cavitation regime; indeed, it is influenced more by the cavitation number than the Reynolds number. Finally, strong turbulence induced by the collapse of cavitation clouds near the exit plays an important role in ligament formation. Moreover, Sou et al. [Sou et al., 2007] concluded that nozzle cavitation and the liquid jet can be classified into four regimes: no cavitation (wavy jet), developing cavitation (wavy jet), super-cavitation (spray), and hydraulic flip (flipping jet).

Recent experimental work has shifted focus from simple cloud shedding to the complex topology of vortex-induced "string" cavitation and its interaction with real-world fuel properties. High-speed optical and X-ray studies by Cao et al. [Cao, 2020] and Shen et al. [Shen et al., 2025] have distinguished between "geometric" wall cavitation and "string" cavitation, confirming that the latter originates from vortical flows in the sac volume and can extend through the nozzle center without touching the walls. Unlike wall-bound clouds, these strings are surprisingly stable and less erosive, yet they drastically alter the spray structure by inducing a hollow-cone effect that increases the spray angle. Complementing this, Mitroglu et al [Mitroglou et al., 2016]. and recent work using synchrotron X-ray imaging (e.g., at Argonne National Laboratory) has effectively resolved the "optical blackout" region, proving that internal needle wobble creates transient eccentricities that drive these string structures, a phenomenon previously invisible to standard optical techniques [Mamaikin et al., 2021].

Simultaneously, the focus on erosion-induced mechanisms has matured to include fluid property effects beyond simple vapour pressure. Experimental campaigns by Magnotti and Som [Magnotti and Som, 2022] and others utilizing X-ray tomography have quantified that while high vapour pressure fuels increase cavitation volume, it is the fuel viscosity that dominates the erosion

severity; lower viscosity fuels reduce dampening, allowing collapse shockwaves to impact nozzle walls with greater intensity. This is supported by Zhang et al. [Zhang, 2025], who investigated methanol in scaled-up nozzles, observing that methanol's unique saturation properties lead to more violent, albeit shorter, cavitation zones compared to diesel. Furthermore, Butcher [Butcher, 2020], and Balz et al. [Balz, 2021] provided critical insights into hardware geometry, experimentally verifying that the microscopic roughness from laser-drilling versus spark-erosion (EDM) significantly alters the inception point of cavitation, with smoother laser-drilled holes unexpectedly promoting earlier hydraulic flip.

The main points highlighted in the literature regarding cavitation in injectors and sprays are:

- Cavitation increases the spray cone angle. Concerning the internal flow, the maximum outlet velocity rises when cavitation occurs. This is due to the reduction in the cross-sectional area of the liquid phase at the outlet section of the orifice [Payri et al., 2004].

- Needle movement can induce a highly transient and potentially chaotic cavitating flow in nozzles, especially during near-closure periods. The cavitation morphology at low needle lift differs significantly from that at high needle lift [He et al., 2013].

- The extent of cavitation regions is slightly affected by fuel type, but is strongly dependent on nozzle geometry [Battistoni and Grimaldi, 2012]. Indeed, vorticity generated upstream in the sac caused by the movement of the needle must be taken into account because those cavitation strings can extend right through the hole and completely change the spray angle and atomization quality

- Cavitation is sensitive to changes in injection conditions. Specifically, cavitation increases with the nozzle output angle and decreases with the nozzle length-to-diameter ratio [Jiang et al., 2015].

Cavitation-Induced Erosion

Experimental results of the catastrophic cavitation-induced erosion on injector orifices and needles can be observed in Fig. 2.10 and Fig. 2.11. VCO (Valve Covered Orifice) and Sac-type nozzles are two possible types of diesel engine injectors. In the VCO nozzle, the needle tip sits directly over the spray holes, effectively sealing them shut; in fact, there is no sac volume. In this kind of nozzle, the fuel turns sharply into the hole, which creates chaotic, asymmetric flow and varies extensively if the needle wobbles. The main benefit is that it minimises the trapped fuel volume, significantly reducing dribble and HC emissions. The sac-type nozzle has a small volume below the needle seat where fuel is collected before entering the spray holes. The sac stabilises the flow, making the spray more uniform and symmetric hole-to-hole. After the injection ends, fuel trapped in the sac evaporates or 'dribbles' out, causing high Hydrocarbon (HC) emissions.

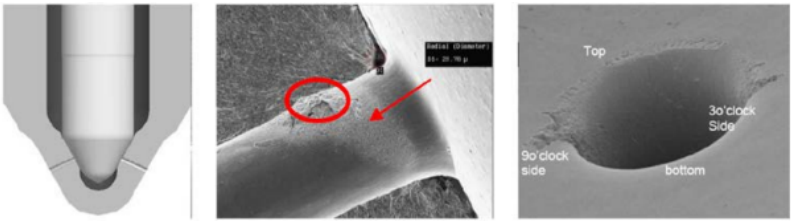

Figure 2.10: Cavitation-induced erosion damage in a VCO nozzle focusing on the erosion damage at the top part of the injection hole and at the two sides of the injection hole [Piehl and Bravo, 2018].

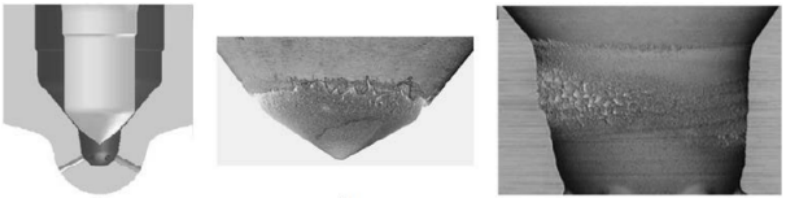

Figure 2.11: Cavitation-induced erosion damage in a sac-type nozzle focusing on the erosion damage both on the needle and on the sac volume[Piehl and Bravo, 2018].

In general, cavitation-induced erosion is a complex phenomenon, which can be divided into three stages:

- **Incubation period**: no material is removed during this stage.
- **Acceleration period**: mass loss begins and increases over time.

- **Steady-state period**: characterised by constant mass loss.

These phases can be more or less pronounced, depending on the application and the eroded material. Some authors [Patella et al., 2000, Franc, 2009] used pitting tests to describe the aggressiveness of a cavitating flow during the incubation period. However, a particular study [Okada et al., 1994] combined two techniques by analysing single pits on a pressure sensor and comparing them to the recorded pressure signal. Okada found a linear relation between the pit diameter and the corresponding peak pressure. Hattori et al. [Hattori and Nakao, 2001] analysed the particles removed from the material using a device that generates cavitation through a vibrating horn. They reported that, during the initial stage, the volume loss was dominated by small particles ($\approx 3\mu m$) due to impact fracture, while larger particles ($\leq 10\mu m$) were generated by fatigue fracture, which dominates the erosion process in the steady-state period. Similar results were reported earlier by Endo [Endo et al., 1969]. It was stated that the two mechanisms are triggered by impacts of different strengths, namely, single high-intensity impacts in the case of impact fracture, and a large number of lower-intensity impacts in the case of fatigue fracture. The experimental studies indicate that, for a comprehensive quantification of the erosive potential of a flow, the complete load spectrum on the material must be determined.

In summary, cavitation-induced loads are characterised by short duration, high amplitude, and a small affected area [Kim et al., 2014]. Cavitation-induced erosion is challenging to quantify experimentally due to its spatially localised influence. However, two different approaches have been employed in the literature:

- **Pressure sensors** to measure pressure peaks [Franc et al., 2011, Hattori et al., 2010, Streller et al., 2005]: while high-frequency sensors allow for temporal resolution of the peaks, they also introduce low-pass spatial filtering down to the finite sensor size, and their placement can influence the flow field.

- **Pitting tests**: these tests are usually of short duration, and the flow

is made to cavitate on soft, ductile materials to identify pits formed by single impacts. While these tests provide spatial information about the load, they do not capture the time-dependent characteristics of the impact. Moreover, the results obtained are always a combination of the impact load and the material properties [Jayaprakash et al., 2012, Franc, 2009, Hattori and Nakao, 2001, Patella et al., 2000].

Although these results are very important for classifying and understanding cavitation-induced erosion, their applicability is limited as they depend on specific operating conditions and the choice of materials.

Recent experimental work has moved beyond simple mass-loss measurements to spatially resolved quantification using X-ray diagnostics. Magnotti and Som [Magnotti and Som, 2022] utilized X-ray tomography to demonstrate that erosion is not uniform but highly localized to specific "incubation" zones where the re-entrant jet frequency matches the material's fatigue limit. Furthermore, Perera [Perera, 2025] provided critical direct visualisation evidence that severe erosion is not limited to the nozzle holes but also degrades the needle seat area within the sac volume. This internal degradation alters the needle sealing and lift dynamics over time, leading to leakage and "drift" in injection quantity even when the nozzle holes themselves remain intact.

The transition to alternative fuels has introduced new erosion risks governed by fluid properties rather than just operating pressure. While it is classically understood that higher vapour pressure increases cavitation volume, Magnotti and Som [Magnotti and Som, 2022] and Zhang et al. [Zhang, 2025] experimentally decoupled these factors to prove that fluid viscosity is the dominant variable in erosion severity. Their work indicates that while low-viscosity "green" fuels (like methanol and ammonia) are more prone to cavitate, they lack the viscous dampening of diesel, allowing collapse shockwaves to impact the wall with significantly higher intensity. Zhang et al. [Zhang, 2025] further highlighted that in methanol injectors, this leads to a "shorter but more violent" erosion zone that requires specific structural reinforcement (e.g., inlet rounding) to prevent rapid failure compared to traditional heavy-fuel counter-

parts.

2.1.5 Cavitation Effects on Spray Formation

Cavitation within diesel injector nozzles is an important hydrodynamic phenomenon that significantly influences spray formation, atomisation quality, and combustion efficiency. As modern injectors operate at increasingly high pressures and feature refined geometries, cavitation becomes both an inevitable challenge and a potential tool for optimising spray behaviour. The review by [Sun et al., 2019] presents a comprehensive analysis of how cavitation inside high-pressure fuel injector nozzles promotes liquid jet breakup, summarising the formation and regimes of cavitation and correlating discharge coefficients to flow dynamics. Using high-speed imaging and 3D simulations, [Mitroglou et al., 2016] identified "string cavitation" vapour structures rooted in recirculation zones, which can cause up to a 10% variation in instantaneous injected mass due to their influence on nozzle exit conditions.

Multiple studies converge on the beneficial role of cavitation in enhancing atomisation. Patel's recent review [Patel and Bambhania, 2023] highlights how cavitation-induced bubble collapse near nozzle exits enhances liquid fragmentation and spray quality, while also examining geometric and operational parameters that impact cavitation development. A combined numerical–experimental study [Yan et al., 2016] demonstrated that, with increasing injection pressure, spray penetration increases, spray angle widens, and Sauter Mean Diameter (SMD) decreases by approximately 9% per 20 MPa increment.

A study from Mohamed et al. found that, in the absence of cavitation, the liquid jet exhibits poor atomisation and extended breakup lengths. Conversely, cavitation induces turbulent mixing ("churning flow"), shorter breakup lengths, smaller droplets (lower SMD), wider cone angles, and increased jet velocity [Mohamed et al., 2021]. Transparent nozzle experiments by Shibata et al. similarly documented the synchronised progression of cavitation and atomisation phenomena, revealing strong correlations and suggesting that controlled cavitation can be used to optimise nozzle design for superior atomisation [Shi-

bata et al., 2015].

Finally, Soteriou et al. (and then Mithun et al.) discussed the relationships between cavitation, hydraulic flip, spray irregularities, and differences in atomisation between single-hole and multi-hole nozzles [Soteriou et al., 1995] [Mithun et al., 2018]. Additionally, a study from Payri et al. employed optical-engine experiments to show that cavitation alters injection rates and can induce flow choking, thereby influencing spray and combustion patterns captured in high-resolution imaging [Payri et al., 2006].

2.2 Collapse Dynamics in Numerical Studies

As discussed in the previous section, experimental measurements of cavitating flows are considerably challenging, especially in injection systems, because of the micro-scale nature of the process. Moreover, the quality of the liquid and the accuracy of the measurement instruments affect the overall results. For that reason, parallel to experimental investigations, numerical modelling of cavitating flows has gained significant momentum and sophistication over the last two decades.

Notwithstanding, the aforementioned spatiotemporal complexities, as well as additional flow and heat transfer processes ranging from compressibility effects to viscous dissipation, render the modelling and simulation of two-phase flows with phase change challenging. No CFD approach has sufficient robustness and accuracy across all flow scenarios where cavitation onset and evolution are critical [Rodriguez et al., 2021].

Three categories of cavitation models, based on their fundamental assumptions, are presented here. The first group is based on transport equations, where the multiphase flow is treated as a homogeneous mixture. One set of continuity and momentum equations is used to calculate the mixture flow, along with a transport equation to capture the vapour–liquid interface. The transport equation can be based on the volume-of-fluid (VOF) method [Singhal et al., 2002] or on a level-set method [Lauer et al., 2012]. In addition, mass transfer between the phases is defined as an explicit source term in the

transport equation. This approach, known as the Finite Mass Transfer (FMT) method [Kubota et al., 1992] [Bohbot et al., 2009], requires a numerical model to estimate vapourisation and condensation rates.

Most models in the literature [Schnerr and Sauer, 2001] estimate the phase-change rate using a simplified form of the Rayleigh–Plesset equation (Eq. 2.1), in which the second temporal derivative of the bubble radius and the effect of non-condensable gas are neglected. To improve model accuracy, some empirical constants are included, which must be tuned for each simulation to adjust the mass transfer rate. However, the uncertainty associated with these constants is a limitation of the FMT approach. The transport equation method is commonly implemented in pressure-based algorithms, and the fluids are usually assumed to be incompressible. A few studies [Koukouvinis, Gavaises, Supponen and Farhat, 2016, Koukouvinis, Gavaises, Li and Wang, 2016, Yakubov et al., 2014] consider fluid compressibility, showing that incorporating compressibility into the pressure correction equation can lead to ill-conditioned coefficient matrices and numerical issues in steady-state or large-time-step transient simulations. Nevertheless, compressible and incompressible simulations generally exhibit similar cavitation behaviour. Therefore, for large-scale problems, incompressible transport-equation models are more common, as they are less computationally expensive and allow larger time steps, compared with equilibrium-based models (the third approach described below). Finally, cavity structures smaller than the grid size, such as cavitation nuclei or sparse bubble clouds, may be under-resolved and diffused, potentially reducing simulation accuracy in predicting cavitation-induced erosion.

The Discrete Bubble Model (DBM) [Giannadakis, 2005, Giannadakis et al., 2008] constitutes the second approach. In this methodology, cavity structures are tracked in a Lagrangian framework, while the continuum flow is calculated using Eulerian governing equations. Cavity structures are considered individual bubbles, and groups or parcels of bubbles are tracked by solving Lagrangian equations of motion. To capture cavity dynamics more accurately, various interactions—such as flow forces on bubble trajectory and dynamics, turbulence effects on bubble motion and break-up, and bubble–bubble inter-

actions—must be modelled appropriately. DBMs are limited in representing large or non-spherical vapour structures. To overcome this, hybrid multi-scale models have been developed, representing large cavities using a transport-equation model, while tracking small-scale structures in a Lagrangian framework. Ghahramani et al. [Ghahramani et al., 2019] demonstrated the capability of an Eulerian–Lagrangian cavitation model to estimate the dynamics of collapsing bubbles by coupling an Eulerian FMT model with a Lagrangian model. Here, vapour–liquid mixture properties are obtained via a volume-fraction methodology, tracking cavities in the Lagrangian framework rather than solving an Eulerian transport equation. Generally, Lagrangian or hybrid models provide a less precise estimation of the liquid–vapour interface than fully Eulerian models, but require a coarser mesh and thus fewer computational resources.

The third category treats the two-phase cavitation regime as a single fluid under the assumption of mechanical and thermodynamic equilibrium, implying that the mass transfer rate at the vapour–liquid interface is infinitely fast. These models are mostly implemented in density-based algorithms with various approaches to determine the pressure–density relationship. Schnerr et al. [Schnerr et al., 2008] used an EoS to find flow pressure as a function of temperature, identifying different phases and the interface based on local density. Kyriazis et al. [Kyriazis et al., 2017] introduced an explicit density-based solver with real-fluid thermodynamic properties for n-dodecane, demonstrating heating effects in bubble collapse. When flow temperature variations are small, the EoS can be temperature-independent, simplifying the pressure–density relation; this leads to the barotropic EoS. Barotropic models can be implemented in both density- and pressure-based algorithms. Goncalves et al. [Goncalves et al., 2010] compared incompressible pressure-based solvers with compressible density-based solvers using barotropic cavitation models and highlighted the need to account for fluid compressibility for accurate cavitation dynamics.

Single-fluid EoS models typically require no empirical parameters; however, the captured liquid–vapour interface is often diffuse, necessitating high grid resolution and very small time steps to predict sharp interfaces accurately.

Capturing pressure-wave propagation also demands small time steps. Consequently, these models are computationally expensive and are usually applied to cavitating flows in small-scale geometries [Wrona et al., 2003]. When coupled with real thermodynamic EoS, they can avoid some simplifications present in the first two categories [Dumbser et al., 2013] [Kyriazis et al., 2017].

This is why the algorithm presented here represents a step forward in numerical analysis and thermodynamics. This methodology can capture both small-scale and full-scale cavitation. It is among the first works implementing a Mach-consistent numerical flux coupled with real-fluid properties for various fuels, demonstrating heating effects in bubble collapse and in-nozzle flow problems. The only comparable work is by Dumbser et al [Dumbser et al., 2013], which focuses on water/vapour behaviour in benchmark (e.g., shock tube, explosion/implosion, forward step) and macroscopic (e.g., hydrofoil) cases, and the work of Kyriazis et al. on single-component fuel surrogates [Kyriazis et al., 2017].

2.2.1 DNS Approaches in In-Nozzle Flows and Their Limitations

In order to complete the literature review on Collapse Dynamics in Numerical Studies, a brief discussion on DNS and its limitations is given in this section. In general, Direct Numerical Simulation (DNS) is defined as a simulation in which the Navier-Stokes equations are solved without any turbulence modelling or averaging, resolving all continuum spatial and temporal scales. For the specific case of in-nozzle cavitation and primary atomization, a genuine DNS approach implies two simultaneous requirements:

- The resolution of the smallest turbulent scales (Kolmogorov length, η)
- The full resolution of the topological evolution of the multiphase interface, including phase change dynamics and surface tension forces, down to the smallest stable bubble or droplet size (Hinze scale) [Gorokhovski and Herrmann, 2008].

Consequently, the interface is treated not as a modelled continuum mixture (as in Volume of Fluid or Level Set methods with sub-grid models), but as a sharply resolved discontinuity where boundary conditions for mass, momentum, and energy conservation are explicitly satisfied.

Despite the theoretical rigour of DNS, its application to industrial fuel injectors remains computationally intractable due to the extreme disparity of scales inherent to high-Reynolds and high-Weber number flows. Regarding turbulence scaling (Re), in modern high-pressure diesel or GDI injectors, exit velocities often exceed $500\,m/s$, yielding Reynolds numbers in the range of $Re \approx 20,000 - 50,000$ within micrometre-scale geometries. The computational cost of resolving single-phase turbulence scales with the Reynolds number (Re) as $N_{grid} \propto Re^{9/4}$. While single-phase DNS at these Reynolds numbers is achievable on massive supercomputers (e.g., channel flows), the geometric complexity of real nozzles, including needle movement and wall roughness ($\sim 1\,\mu m$), imposes grid requirements that currently exceed exascale capabilities [Pope, 2000]. Furthermore, considering interface and capillary scaling (We), the limiting factor in spray simulations is not the turbulence, but the interface. In the primary atomization region, the high aerodynamic shear forces generate droplets orders of magnitude smaller than the local nozzle diameter. To resolve the interface physics "genuinely," the grid spacing (Δx) must be smaller than the smallest relevant length scale of the liquid structures. This is governed by the Weber number (We). As noted by Tryggvason et al., resolving the thin boundary layers around deforming droplets and the capillary waves on the jet surface requires grid resolutions that scale prohibitively with We [Tryggvason et al., 2011]. Finally, for cavitating flows, "Genuine DNS" faces a thermodynamic impossibility at the continuum level. Cavitation inception is driven by nucleation sites (micro-bubbles or wall crevices) that are typically on the order of nanometers to micrometres (10^{-6} to 10^{-9} m). Resolving the inception and growth of individual cavitation bubbles from these nuclei, along with the subsequent collapse-induced shock waves (which require compressible solvers with extremely small acoustic time steps), is impossible for macroscopic nozzle geometries. As a result, even high-fidelity studies typically resort to

"quasi-DNS" or highly resolved Large Eddy Simulation (LES) coupled with homogeneous mixture models or discrete bubble tracking, rather than fully resolving the phase boundary of every cavitation event [Koukouvinis, Gavaises, Li and Wang, 2016].

2.3 Wall-bounded cavitating flow and spray mixing in multi-component environments

The development of high-pressure common-rail systems, initially introduced to the market in 1997, has led to an approximate 50 % reduction in NO_x and soot emissions, irrespective of the emission after-treatment technology utilised; such systems are now employed in most vehicle types. This reduction in emissions is due to enhanced mixing achieved by increasing injection pressures beyond 2000 bar, which facilitates the atomisation of the injected fuel and consequently reduces vapourisation time. Along these lines, a significant further reduction of emissions can be achieved by injecting fuel against the air charge at pressure and temperature (P-T) conditions well above the fuel's critical point, as this reduces fuel heating time and enhances air–fuel mixing under conditions where the liquid–gas phase boundary disappears, as in supercritical fluid conditions [Anitescu et al., 2012, Lin, 2011].

Utilisation of NZE fuels, biofuels, and relevant additives could lead to a further decrease in soot formation during combustion in all types of IC engines [Baran, 2023, Hawi et al., 2019, Kook and Pickett, 2012, Lemaire et al., 2009]; at the same time, multiple injections of short duration that modulate fuel delivery via the fast opening and closing of the injector's needle valve, combined with exhaust gas recirculation, can significantly reduce both soot and NO_x emissions, as demonstrated decades ago [Han et al., 1996].

Relevant to the present work, experimental data have shown that increasing the injection pressure even up to 500 MPa causes a reduction in soot formation [Nishida et al., 2017, Pickett and Siebers, 2004, Vera-Tudela et al., 2020]. The latter detailed experimental work analysed the behaviour of vapourisa-

tion, mixing, and combustion, revealing improved mixing due to higher spray velocities. However, the μ-scale of injectors makes experimental flow characterisation inside the injector challenging, especially under such high injection pressures.

Increasing the injection pressure and multiple injections of short duration result in very high fuel velocities combined with an increase in in-nozzle fuel temperature [Vidal et al., 2021], as recently reported by the group at City. Under such transient and elevated rail pressure conditions, the sharp pressure and temperature gradients lead to the formation of cavitation, which tapered nozzles cannot compensate for. Although cavitation collapse may remove surface deposits and improve primary jet break-up [Sou et al., 2007], it may also damage the injector material [Dular et al., 2004, Mitroglou et al., 2016, Zhang et al., 2018*a*] and reduce the injector's fuel delivery capacity.

As experimentation under such conditions is rather limited, the vast majority of studies relevant to fuel injection utilise CFD models, which have been applied in this field for more than 30 years. Early studies conducted since the mid-'80s have decoupled the in-nozzle phase-change effects from the subsequent atomisation/mixing of the injected fuel (although, in reality, they are strongly linked), yet still represent the most frequently used approach in industrial design. This is because flow methodologies adopting a multi-scale and multi-physics approach, coupling the in-nozzle flow development with fuel atomisation and subsequent mixing, are computationally demanding.

The well-known Eulerian-Lagrangian approach for modelling spray development utilises inlet/boundary condition information relevant to the fuel injection rate. The latter can be either predicted or measured. The first attempt at a phenomenological model introduced to capture the effects of in-nozzle cavitation on spray formation was reported in [Arcoumanis et al., 1997]. Subsequent, but still early, studies utilised the volume of fluid (VOF) model to simulate simultaneously the in-nozzle flow and the subsequent spray development, but for non-cavitating nozzle configurations and assuming constant fuel properties. Probably the first works addressing the strong dependence of fuel properties on pressure and temperature via real fluid thermodynamics effects in fuel injec-

tion are those from the City group (e.g. [Strotos, 2014]); still, only in-nozzle flow simulations using RANS were performed, which greatly under-resolved turbulence effects and lacked correlation to subsequent spray formation. The adverse effect of turbulence in Diesel injector operation has been analysed in [Salvador et al., 2013], showing the generation of highly transient cavitation structures that can travel even beyond the orifice exit, affecting the injected spray.

Numerical works attempting to compute the in-nozzle flow simultaneously with the jet/spray formation have only recently appeared. In [Devassy et al., 2015], a multi-level simulation of a Diesel injector was performed. The flow distribution at the injector outlet was subsequently used for spray modelling inside the engine cylinder; while this enabled prediction of the jet, coupling between the jet and in-nozzle flow was weakly enforced in a one-way manner.

The numerical work of [Orley et al., 2015] on Diesel injectors involved a stronger coupling of in-nozzle flow and jet atomisation in a unified framework; however, the thermodynamic model omitted temperature-dependence effects. Works from the group at City and collaborators [Gavaises et al., 2022, Santos et al., 2020] have utilised barotropic-type models to simulate simultaneously and in a fully-coupled manner the in-nozzle flow, nozzle wall wetting, fuel dribbling, and spray formation, but for low injection-pressure conditions not requiring strong variation of fuel properties with P-T to be taken into account.

Recent works [Cristofaro et al., 2018] have investigated the effect of cavitation and fuel properties on nozzle flow, spray formation, and induced erosion in fuel injectors. However, in these studies, although an Eulerian-Eulerian two-fluid model was utilised in AVL Fire, a weak coupling between the in-nozzle flow and the subsequent spray was imposed by splitting the computational domain at the injector exit and performing separate simulations for the in-nozzle flow and the subsequent spray formation. These fully-coupled in-nozzle flow and spray evolution simulations are not applicable under Supercritical Fluid Conditions (SFC) in fuel injection, which are promising for increasing engine performance while reducing emissions [Dahms and Oefelein, 2015, Falgout et al., 2016, Qiu and Reitz, 2015]. Investigations of supercritical injection

of Diesel fuel and its components were recently reported in [Lin and Tavlarides, 2012], showing enlarged cone angles and improved mixing. An inherent advantage of SFC injection is the absence of the enthalpy of vaporisation and the low (or zero) surface tension. This is observed whether the SFC fuel is a single-component, a surrogate fuel, or a more realistic, multi-component mixture [Arai et al., 2002].

Finally, an additional complexity in fuel-injector simulations arises from the motion of the needle valve. Successfully simulating the needle movement in liquid-fuel injection systems is another crucial element in capturing cavitation phenomena and spray development [Manin et al., 2020, Torelli, 2018, Battistoni et al., 2019].

2.4 Fuel Property Variation and Relevant Modelling Approaches

One limitation in studying SFC injection is the absence of databases for the fuel properties over the extreme P-T conditions required. The published database for Diesel surrogates from Sandia National Laboratories [Mueller and et al., 2016], which was specifically derived to overcome the uncertainties in relevant modelling activities, is limited to conditions below the fuel's critical point. NIST databases [Lemmon et al., 2013, *NIST Refprop Database*, 2022] include hydrocarbon data from methane only up to dodecane (C_{12}); however, Diesel composition involves hydrocarbons up to n-docosane (C_{22}), for which data are missing.

Since Diesel fuel is a complex hydrocarbon mixture, one needs not only the properties of the components but also mixing relations that depart from idealised thermodynamics [Harvey and Lemmon, 2004]. As NIST or other databases are not applicable, it is commonplace to either employ an advanced cubic Equation of State (EoS) [Lacaze and Misdariis A, 2015] with relevant mixing rules [Matheis and Hickel, 2017] or employ a semi-empirical Helmholtz energy model (PC-SAFT) [Bamgbade, 2015]. The issue is that, due to the

complexity of the phase diagram, even advanced cubic EoS may not be sufficiently accurate.

Thus, modifications have been developed to improve the accuracy of EoS, e.g., the "Volume Translation" method for the Peng-Robinson (PR) and Soave-Redlich-Kwong [Matheis and Hickel, 2017] equations. Especially for heavy hydrocarbons, measurements are limited up to 523 K [Wu, 2011], which is $\approx$ 130 K lower than the critical point, necessitating additional measurements describing critical conditions for Diesel fuel blends, including biofuels. New experiments and simulations on the properties of Diesel fuel at elevated pressures and temperatures have been performed, selectively for pressures up to 450 MPa [Rokni et al., 2019, Rowane et al., 2020, Vidal et al., 2020]. Relevant to this study, the thermophysical properties, such as density and viscosity, were modelled by the team at City using the PC-SAFT theory for pressures up to 450 MPa [Vidal et al., 2021]. Tabulated data were derived for various fuel surrogates covering the range of properties occurring within high-pressure fuel injectors, thus allowing for an accurate estimation of the effects of the various fuel properties (more detailed information can be found in Appendix A). Such data have also been used for coupling the in-nozzle flow with spray simulations in past studies, but without considering cavitation [Koukouvinis et al., 2020], or by using a simplified mass transfer rate cavitation model [Vaz et al., 2022].

Novel methodologies utilising implicit pressure-based finite-volume frameworks, incorporating real-fluid EoS, multi-component vapour-liquid equilibrium (VLE) calculations [Koukouvinis et al., 2020], and diffuse interface methodologies have been presented. However, these face difficulties in achieving convergence when dealing with internal flows under cavitating conditions. This difficulty stems from the representation of density as a function of pressure and temperature, leading to a discontinuous density field that renders the implicit iterative solution unstable.

In the study by [Matheis and Hickel, 2017], it was shown that an explicit multiphase, density-based, large-eddy Eulerian model can be utilised to simulate liquid-fuel injection and mixing under high-pressure conditions. The model

incorporates the PR equation of state and vapour-liquid equilibrium calculations. To identify single-phase and two-phase states, an isobaric-isothermal algorithm (PT-flash) and a Tangent Plane Distance (TPD) function are employed. In the case of a two-phase state, the PT-flash algorithm determines the composition of the liquid and vapour phases by minimising the Gibbs free energy of the system. This approach yielded precise results for the baseline case of the ECN Spray A fuel injector [*Sandia National Laboratories - Spray A*, 2024] under various operating conditions. In [Fathi et al., 2022], the CFD approach described in [Matheis and Hickel, 2017] was employed along with an optimised iso-energetic/iso-choric algorithm (UV-flash) [Fathi and Hickel, 2021] to simulate both inert and reactive sprays under trans-critical conditions. The Redlich-Kwong-Peng-Robinson (RKPR) equation of state was utilised to address the density prediction error associated with the Peng-Robinson (PR) equation of state, as mentioned in [Matheis and Hickel, 2017]. While the framework discussed in [Fathi et al., 2022] can simulate cavitating in-nozzle flows, no validation was performed for these conditions.

The implementation of explicit density-based solvers with real-fluid EoS is complicated by the high non-linearity of the thermodynamic model. This frequently results in spurious pressure oscillations across phase boundaries [Ma et al., 2019]. Although quasi-conservative (primitive variable) formulations can suppress these oscillations, they typically violate strict total energy conservation, leading to artificial temperature drift, a critical source of error when modelling fuel heating [Matheis and Hickel, 2017, Rodriguez et al., 2021]. However, recent work by Fathi et al. [Fathi et al., 2022] demonstrated that these oscillations can be effectively suppressed within a fully conservative framework, ensuring both numerical stability and thermodynamic consistency. The accuracy of the EoS is another relevant aspect in accurately simulating liquid-fuel injection systems. The PC-SAFT model has superior performance over cubic EoSs, a fact that has been well-established in the literature and confirmed in numerous studies [Leekumjorn and Krejbjerg, 2013, Liang et al., 2012, Salimi and Bahramian, 2014].

The primary advantage of the PC-SAFT model, especially relevant to this

context, lies in its capability to predict derived properties. These include critical attributes such as compressibility and speed of sound, which play an important role in density-based explicit CFD formulations. Once the computation of residual entropy is performed, the transport properties of the mixture can then be determined using entropy scaling methodologies and multiphase mixture rules [Rodriguez, Rokni, Koukouvinis, Gupta and Gavaises, 2019].

Central to this concept are the Group Contribution (GC) methodologies [Gross and Sadowski, 2002], enabling the estimation of input parameters by considering the contributions from individual molecular groups. This predictive approach eliminates the need for expensive experimental measurements to calibrate thermophysical models, allowing for accurate estimates of the thermodynamic properties of new multi-component mixtures. In a recent publication from the group [Geber et al., 2023], this approach was utilised to analyse the fuel properties of various substances, including oxymethylene dimethyl ethers (OME3-4) and alcohol blends with gasoline and diesel. Model results were benchmarked against experimental and computational data, observing good agreement with minor deviations [Geber et al., 2023].

2.4.1 Methodologies for Needle Movement in Transient Nozzle Simulations

Accurately capturing the transient motion of the injector needle is critical for predictive in-nozzle flow simulations, as the needle lift dictates the effective flow area, turbulence generation, and cavitation inception mechanisms. However, incorporating this moving boundary into the computational domain presents a significant numerical challenge. The topology of the fluid domain changes drastically during an injection event, transitioning from a hermetically sealed state (zero volume at the seat) to a fully developed flow channel. Methodologies to address this dynamic topology can be broadly categorised into Body-Fitted (Arbitrary Lagrangian-Eulerian) approaches, Immersed Boundary methods, and techniques utilising Adaptive Mesh Refinement (AMR).

The traditional approach to needle movement relies on body-fitted meshes

that deform to accommodate the changing geometry. In the Arbitrary Lagrangian-Eulerian (ALE) framework, the computational grid moves with the boundary velocity, maintaining a sharp interface between the fluid and the solid wall. Methodologies within this category are diverse. Some approaches rely on mesh morphing, where the internal grid points are stretched or compressed based on the boundary displacement [Santos et al., 2020]. While computationally efficient for small displacements, morphing is limited by mesh quality degradation; excessive stretching leads to highly skewed cells that induce numerical errors or divergence. To mitigate this, topological changes such as layer addition/removal are often employed. As the needle lifts, new layers of cells are inserted into the domain, and as it closes, layers are collapsed and removed [Koukouvinis, Gavaises, Li and Wang, 2016]. Alternatively, complete re-meshing strategies generate an entirely new grid at specific time steps [Huang et al., 2013]. The primary limitation of body-fitted ALE methods is the "topology problem" at closure. Finite volume methods require cells to have a positive, non-zero volume. Consequently, these methods cannot simulate the needle fully closing (touching the seat), as this would collapse the cells at the gap to zero volume. This necessitates a minimum lift approximation, where the simulation must start and end with the needle slightly hovering above the seat (typically 2%–8% of maximum lift) [Orley et al., 2015, Zhang et al., 2018*b*]. This artificial gap allows leakage and prevents the simulation of the true hydraulic impact and water-hammer effects that occur during needle closure.

To circumvent the topological constraints of body-fitted meshes, Immersed Boundary (IB) and Cut-Cell methods have gained prominence. In this framework, the background fluid mesh remains stationary (typically a Cartesian grid), and the solid needle geometry "immerses" or cuts through the existing cells. The governing equations in the cells intercepted by the solid boundary are modified to enforce the no-slip condition, often by modifying the discretisation stencil or adding a forcing term to the momentum equation.

Cut-cell approaches [Orley et al., 2015, Pickett and Siebers, 2004] offer a potential solution to the minimum lift problem. Since the background grid

does not deform, the solid boundary can theoretically pass entirely through a fluid cell, effectively " closing" the valve without collapsing the mesh. A notable application is found in [Stavropoulos Vasilakis et al., 2019], where the full cycle of a diesel injector needle was simulated using an IB method, demonstrating its efficacy in handling complex cavitating flows without the need for mesh morphing. The trade-off for IB methods is the resolution of the near-wall physics. Because the grid is not aligned with the wall, the boundary layer is often represented by a "staircase" approximation or requires complex wall-model interpolation. In high-Reynolds-number nozzle flows, accurate prediction of wall shear stress and near-wall turbulence is critical for capturing cavitation inception, which can be compromised if the cut-cells are not sufficiently resolved.

Adaptive Mesh Refinement (AMR) is frequently coupled with both ALE and IB methods to optimise computational cost. In this approach, the solver automatically refines the grid in regions of high gradients (e.g., velocity, density, or volume fraction) and coarsens it elsewhere. This is particularly attractive for nozzle simulations, where the scales of interest (cavitation bubbles, high-velocity jets) are localised and transient. AMR allows for the resolution of sharp interfaces, such as the liquid-vapour boundary in cavitating flows, without the prohibitive cost of a uniformly fine mesh. It dynamically concentrates resources where the physics demands it, such as the vena contracta region or the needle seat gap.

Despite its efficiency, AMR introduces specific challenges for in-nozzle multiphase flows. One major issue involves **conservation errors**. The mapping of flow variables (mass, momentum, energy) from a coarse cell to fine cells (and vice versa) can introduce interpolation errors. In conservative cavitation solvers, these small errors can manifest as artificial pressure oscillations or non-physical "numerical cavitation" at the refinement boundaries [Berger and Colella, 1989].

Another significant challenge is the conflict between **isotropy and boundary layers**. Standard AMR algorithms (like octree refinement) typically split cells isotropically (creating cubes). This is non-ideal for wall-bounded flows,

where the boundary layer requires thin, high-aspect-ratio prisms to resolve the gradients normal to the wall efficiently [Ghosn et al., 2018].

Finally, there is an inherent **time-lag** associated with this method. The refinement criteria are calculated based on the previous time step. In highly transient nozzle flows (where velocities exceed 500 m/s), a cavitation cloud or shock wave may propagate into a coarse region before the mesh has time to refine, leading to a loss of accuracy or "smearing" of the interface [Senecal et al., 2013].

2.5 Summary of Findings and Research Implications

The review of the state-of-the-art regarding cavitation and cavitation-induced erosion reveals a complex interaction between fluid thermodynamics, structural dynamics, and phase-change kinetics. While significant progress has been made in visualising and predicting cavitation regimes, accurately capturing and simulating the erosive potential and the subsequent influence on spray atomization remains a substantial challenge. Synthesising the experimental and numerical evidence presented in this chapter, three critical requirements for high-fidelity injector simulations emerge. These findings directly inform the modelling choices adopted in this thesis.

First, regarding the sensitivity of spray topology to internal flow, the literature consistently demonstrates that cavitation structures within the sac and nozzle holes do not merely reduce the effective flow area; they fundamentally alter the downstream jet dynamics. Specifically, cavitation inside an injector can drastically affect the spray cone angle and atomization quality. Consequently, it is imperative to correctly model the cavitation inside an injector with the fewest possible approximations—avoiding simplified "homogenous equilibrium" assumptions where distinct phase boundaries are critical for predicting the jet exit angle.

Second, there is an absolute need for thermodynamic versatility and geo-

metric dependence. While the topology of cavitation regions is strongly governed by the nozzle geometry (and micron-scale manufacturing deviations), the phase-change inception and collapse intensity are driven by fluid properties. The extent of cavitation regions is affected by fuel type—ranging from conventional diesel to volatile alternative fuels—and their specific saturation pressures and viscosities. Consequently, a thermodynamic model capable of simulating various fuel types and properties without recalibration is fundamental. This necessitates the use of robust Equations of State (EOS) rather than simplified look-up tables restricted to single-component fluids.

Finally, the critical role of transient needle motion must be addressed. Static simulations fail to capture the most aggressive cavitation events. Needle movement has been shown to induce highly transient and potentially chaotic cavitating flows, particularly during the needle opening and closing phases (near-closure periods). These throttle-dependent stages are often where the most violent bubble collapse and erosion risk occur. Therefore, it is a strict requirement that the numerical framework must account for dynamic needle movement to simulate these transient effects accurately, rather than relying on quasi-steady-state approximations.

Despite the consensus on these three points, few existing studies simultaneously address all of them within a single numerical framework. This gap, this thesis proposes a methodology that integrates Immersed Boundary methods with a the use of Real-Fluid thermodynamic EoS. This combination aims to resolve the dynamic boundary changes of the needle while maintaining the thermodynamic rigour required to predict cavitation and erosion across a spectrum of modern fuel types.

Chapter 3

Numerical Methodology

In this chapter, an overview of the developed CFD methodology is provided. The methodology has been developed in OpenFOAM V7 [*OpenCFD Ltd*, 2022], and the numerical framework introduced by Kyriazis et al. [Kyriazis et al., 2017] (who were previously part of the group at City) has been used as a baseline. As a future reference within this document, the new solver has been named multiCompTabFoam. This new solver's thermodynamic closure is based on the PC-SAFT EoS. The methodology's validity is demonstrated through various benchmark cases but, perhaps more importantly, via the high-fidelity simulations of the Spray C [Sandia, 2023] injector under various realistic operational conditions, also mirroring experimental data available in the ECN database.

3.1 Governing Equations

The three-dimensional Navier-Stokes equations for a multi-component, non-reacting mixture of n species were solved using the finite volume method.

- **Continuity Equation**:

$$\frac{\partial \rho}{\partial t} + \nabla \cdot (\rho \vec{u}) = 0 \tag{3.1}$$

Where ρ is the density of the mixture, $\vec{u}$ is the velocity vector of the mixture, and t is the time.

- **Species conservation equation**:

$$\frac{\partial \rho Y_i}{\partial t} + \nabla \cdot (\rho Y_i \vec{u}) = 0 \tag{3.2}$$

where Y_i is the mass fraction of species i. In simulations of highly turbulent fuel injections using explicit solvers, the effect of species diffusion is negligible relative to convective mixing, justifying its exclusion [Vaz et al., 2022].

- **Momentum equation**:

$$\frac{\partial \rho \vec{u}}{\partial t} + \nabla \cdot (\rho \vec{u}\vec{u} + p\vec{I}) = \nabla \cdot \vec{\tau} \tag{3.3}$$

where τ is the viscous stress tensor, p is the pressure, and $\vec{I}$ is the identity tensor. The viscous stress tensor is given by Eq. 3.4.

$$\vec{\tau} = (\mu + \mu_t)\Big(\nabla \vec{u} + (\nabla \vec{u})^T\Big) - \frac{2}{3}\vec{I}\nabla \cdot \vec{u} \tag{3.4}$$

Where μ_t is the turbulent eddy viscosity.

- **Energy equation**:

$$\frac{\partial E}{\partial t} + \nabla \cdot [(E + p)\vec{u}] = \nabla \cdot (\vec{\tau}\vec{u} - \vec{q}) \tag{3.5}$$

where E is the total energy and $\vec{q}$ is the heat flux vector, which is given by the Fourier Law expressed by Eq. 3.6.

$$\vec{q} = -\lambda \nabla T \tag{3.6}$$

λ is the thermal conductivity of the mixture and T is the temperature.

3.1.1 Numerical Methods

To effectively handle the Navier-Stokes equations, a common approach is to employ operator splitting to separate the physical processes into hyperbolic and parabolic sub-steps that correspond to the left and right-hand sides of the equations, respectively. Concerning the hyperbolic sub-step, the multicomponent HLLC (Harten-Lax-van Leer-Contact) solver [Toro, 2009] is applied to

solve the Riemann problem. The fluxes definition are given in Eq. 3.7.

$$\vec{F}_{HLLC} = \begin{cases} \vec{F}_L, & \text{if } 0 \leq S_L \\ \vec{F}_{*L} = \vec{F}_L + S_L(\vec{U}_{*L} - \vec{U}_L), & \text{if } S_L \leq 0 \leq S_* \\ \vec{F}_{*R} = \vec{F}_R + S_R(\vec{U}_{*R} - \vec{U}_R), & \text{if } S_* \leq 0 \leq S_R \\ \vec{F}_R, & \text{if } 0 \geq S_R \end{cases} \tag{3.7}$$

Where $\vec{U}^*_{R,L}$ are the star states [Toro, 2009], which refer to the two intermediate regions of the wave structure that are separated by a contact discontinuity. In addition to that, $\vec{F}_{L,R}$ denote the left and right numerical fluxes, respectively, and S represents the wave speed. The formula utilised to calculate the speed in the middle wave, denoted as S_*, is given by Eq. 3.8

$$S_* = \frac{p_R - p_L + \rho_L \vec{u}_L(S_L - \vec{u}_L) - \rho_R \vec{u}_R(S_R - \vec{u}_R)}{\rho_L(S_L - \vec{u}_L) - \rho_R(S_R - \vec{u}_R)} \tag{3.8}$$

The left and right wave speeds, S_L and S_R, are calculated in Eq. 3.9 and 3.10 respectively.

$$S_L = min(\vec{u}_L - \vec{c}_L, \vec{u}_R - \vec{c}_R) \tag{3.9}$$

$$S_R = max(\vec{u}_L + \vec{c}_L, \vec{u}_R + \vec{c}_R) \tag{3.10}$$

$\vec{u}_R$ and $\vec{u}_L$ represent the velocity components in the right and left states, respectively. Furthermore, $\vec{c}_R$ and $\vec{c}_L$ correspond to the local speed of sound in the right and left states. This way of implementing the HLLC solver has been chosen as it shows good stability and it has been proven so in [Rodriguez et al., 2021]. The MUSCL scheme, together with the van Albada limiter available in OpenFOAM V7, was used to reconstruct the conservative variables at the cell faces. Pressure and speed of sound were calculated at cell centres and reconstructed at cell faces using the upwind scheme [Rodriguez, Koukouvinis and Gavaises, 2019]; this is done to smoothen out the spurious pressure oscillations that might be generated due to the high non-linearity of the EoS (such as the PC-SAFT). The integration of the hyperbolic terms in time was performed

using a third-order Runge-Kutta method [Spiteri and Ruuth, 2002], as shown in Eqs. 3.11, 3.12, and 3.13.

$$\vec{U}^{(1)} = \vec{U}^n + \Delta t \vec{H}(\vec{U}^n) \tag{3.11}$$

$$\vec{U}^{(2)} = \frac{3}{4}\vec{U}^n + \frac{1}{4}\Big[\vec{U}^{(1)} + \Delta t \vec{H}(\vec{U}^{(1)})\Big] \tag{3.12}$$

$$\vec{U}^{(n+1)} = \frac{1}{3}\vec{U}^n + \frac{2}{3}\Big[\vec{U}^{(2)} + \Delta t \vec{H}(\vec{U}^{(2)})\Big] \tag{3.13}$$

where $\vec{U}$ represents the vector of conservative variables, and $\vec{H}$ corresponds to the numerical approximation of the flux function. To advance the parabolic terms in the momentum equation, an implicit diffusion correction equation for velocity [Greenshields et al., 2009] was employed, as shown in Eq. 3.14.

$$\frac{\partial \rho \vec{u}}{\partial t} - \nabla \cdot (\mu \nabla \vec{u}) - \nabla \cdot \vec{T}_{ext} = 0 \tag{3.14}$$

The inter-component coupling present in the stress tensor ($\vec{T}_{ext}$) is handled explicitly and is expressed in Eq. 3.15

$$\vec{T}_{ext} = \mu\Big((\nabla \vec{u})^T - \frac{2}{3}\vec{I}\nabla \cdot \vec{u}\Big) + f_{ib} \tag{3.15}$$

Where f_{ib} represents the volumetric source term of the Immersed Boundary (IB) model. The IB volumetric source term is determined by calculating the difference between the fluid velocity and the IB solid velocity, divided by the time step (as described in Eq. 3.16).

$$f_{ib} = \alpha_{ib}\frac{\vec{u}_{ib} - \vec{u}_{fluid}}{\Delta t} \qquad \text{where } \alpha_{ib} \in [0, 1] \tag{3.16}$$

To localise the effect of the source term, it is multiplied by the IB mask, which distributes the impact to all cells within the IB region, rather than just at the interface. For a more comprehensive understanding of the implementation specifics, please refer to the details provided in [Stavropoulos Vasilakis et al.,

2019] and Appendix B. This feature was not present in OpenFOAM V7, and it has been succesfully implemented and validated in this thesis.

To discretise the time derivatives, a straightforward Euler implicit method was employed, first-order accurate in time. The solution accuracy was ensured by utilizing the CFL (Courant-Friedrichs-Lewy) criterion for the hyperbolic operator to determine the global time step. The Green-Gauss theorem was applied to evaluate the divergences, gradients, and Laplacians in the parabolic terms. Linear interpolation was used to interpolate variables from cell centres to cell faces, enabling the calculation of Gaussian integrals in parabolic terms. The parabolic terms in the energy equation are explicitly solved.

3.2 Local Time Stepping

To prevent the overall simulation time-step from being limited by the smallest length scale in high aspect ratio cells, a modified Local Time Stepping (LTS) methodology has been implemented in OpenFOAM V7. The implementation follows the previous work from [Espinoza et al., 2015], which is explained in more detail in Appendix C.

In this approach, each cell undergoes a local time-step update according to Eq. 3.17.

$$\Delta t_{cell} = \min_{face \in cell} \left(min \left(\frac{V_{cell}/A_{face}}{(c + \vec{u}_{face} \cdot \vec{n}_{face})d} \right), \Delta t_{sim} \right) \tag{3.17}$$

V_{cell} is the volume of the cell, A_{face} is the area of the face, $\vec{u}_{face}$ is the velocity of the fluid, $\vec{n}_{face}$ is the normal vector of the face, c is the speed of sound, d are the geometrical dimensions of the cell, and Δt_{sim} is the maximum time step specified at the initialization of the simulation.

3.3 Turbulence Closure

The Wall Adaptive Large Eddy (WALE) model, known for its favourable performance near walls [Nicoud and Ducros, 1999], was utilised to provide the

required turbulece closure for the turbulent viscosity, which is given in Eq. 3.18.

$$\mu_t = \rho L_s^2 \frac{\left(S_{ij}^d S_{ij}^d\right)^{3/2}}{\left(S_{ij} S_{ij}\right)^{5/4} + \left(S_{ij}^d S_{ij}^d\right)^{5/4}} \tag{3.18}$$

S_{ij} represents the rate of strain tensor, while S_{ij}^d stands for the traceless symmetric portion of the squared strain in the velocity gradient tensor. The length scale, L_s, is determined based on the filter size and the distance from the cell to the wall, d_{wall}, as expressed in Eq. 3.19

$$L_s = min(kd_{wall}, C_w V^{1/3}) \tag{3.19}$$

Where the model constants comprise the Von Karman constant, $k = 0.41$ and $C_w = 0.325$, V is the physical size of the mesh element at that location and, more in general, $V^{1/3}$ is the filter width that is the characteristic length of the grid cell (effectively the "diameter" of the cell).

3.4 Thermodynamic Closure

The thermodynamic closure is based on the PC-SAFT EoS, a derived theoretical model based on perturbation theory [Gross and Sadowski, 2001].

The main assumption of the PC-SAFT Eos is that it separates the intermolecular potential energy of a fluid into repulsive and attractive interactions. To calculate the repulsive contribution, the model defines a reference fluid composed of spherical segments that form molecular chains. The attractive interactions, represented as perturbations to the reference system, are accounted for using a dispersion term [Gross and Sadowski, 2001]. Additionally, the model can include an association term [Gross and Sadowski, 2002] to consider intermolecular bonds formed between segments with association sites, such as proton donors and acceptors. An example of self-association is the formation of hydrogen bonds by the -OH group in alcohols [Chapman et al., 1990]. The PC-SAFT is based on the Helmholtz free energy, which is derived as the sum

of the contributions from the hard chain $\tilde{a}_{hc}$, dispersion $\tilde{a}_{disp}$, and association term $\tilde{a}_{assoc}$.

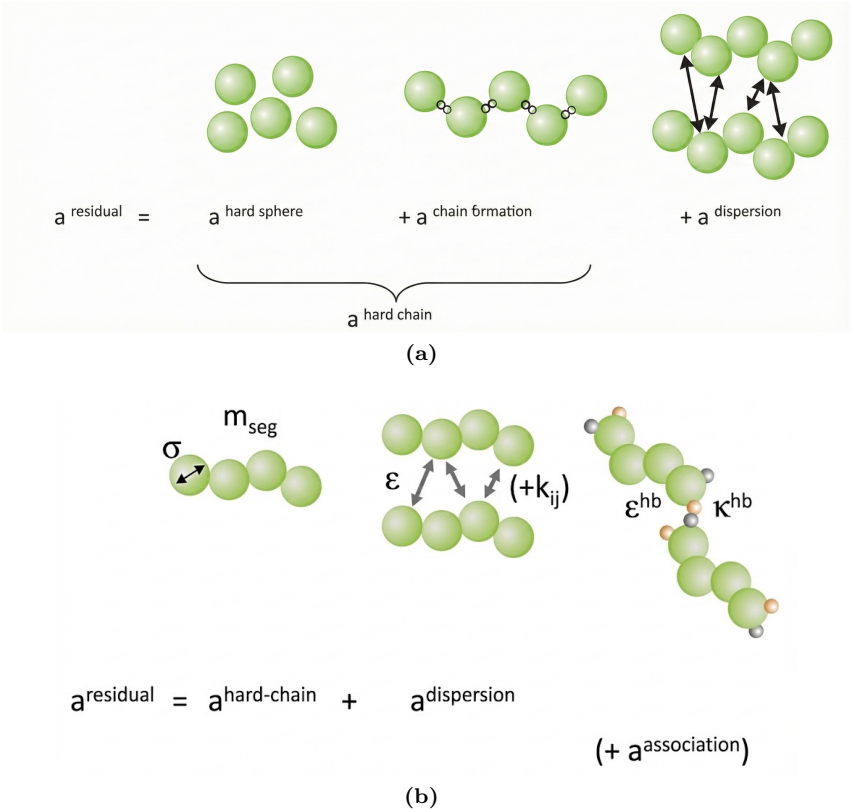

Figure 3.1: Schematic representation of the different Helmholtz free energy terms in the PC SAFT [Arndt and Sadowski, 1994]

A schematic view of these contributions is given in Fig. 3.1 and their mathematical representation is shown in Eq. 3.20.

$$\widetilde{a}_{res} = \widetilde{a}_{hc} + \widetilde{a}_{disp} + \widetilde{a}_{assoc} \tag{3.20}$$

the hard-chain term $\widetilde{a}_{hc}$ of a mixture of n_c components is given by Eq. 3.21.

$$\widetilde{a}_{hc} = \bar{m}\widetilde{a}_{hs} - \sum_{i}^{n_c} x_i(m_i - 1)\ln g_{ii}^{hs}(\sigma_{ii}) \tag{3.21}$$

Where $\bar{m}$ represents the mean segment number in the system, x_i is the mole fraction of component i in the fluid, $\tilde{a}_{hs}$ is the hard sphere contribution, g_{ii}^{hs} is the average radial distribution function of the hard-sphere fluid, m_i is the number of segments per chain for component i. The dispersion term $\tilde{a}_{disp}$

is defined in Eq. 3.22.

$$\widetilde{a}_{disp} = -2\pi\rho_m I_1(\eta,\bar{m})\overline{m^2\epsilon^2\sigma^3} - \pi\rho_m\bar{m}C_1 I_2(\eta,\bar{m})\overline{m^2\epsilon^2\sigma^3} \tag{3.22}$$

Where ρ_m is the molecular density. Details about the terms $I_1(\eta,\bar{m})$, $I_2(\eta,\bar{m})$, and $\overline{m^2\epsilon^2\sigma^3}$ can be found in [Gross and Sadowski, 2001]. The association contribution to the Helmholtz free energy, as stated in [Espinoza et al., 2015][Huang and Radosz, 1990][Huang and Radosz, 1991], can be computed using Eq. 3.23

$$\frac{\widetilde{a}_{ass}}{RT} = \sum_i X_i \left[\sum_{A_i} \left[\ln X^{A_i} - \frac{X^{A_i}}{2} \right] \frac{M_i}{2} \right] \tag{3.23}$$

M_i represents the number of association sites on each molecule of component i, and X^{A_i} is the mole fraction of molecules not bonded at site A for component i, which is given by Eq. 3.24

$$X^{A_i} = \left[1 + \sum_j \sum_{B_j} \rho_j x^{B_j} \Delta^{A_j B_j} \right]^{-1} \tag{3.24}$$

Where $\sum_{B_j}$ represents summation over all sites on the molecules of B_j component j: A_j, B_j, C_j etc. Also $\rho_j = x_j\rho_{mixture}$ is the molar density and $\Delta^{A_j B_j}$ the association strength. The mixture parameters σ_{ij} and ϵ_{ij}, which are defined for every pair of unlike segments, are modeled using a Berthelot-Lorentz combining rule.

$$\sigma_{ij} = \frac{1}{2}(\sigma_i + \sigma_j) \tag{3.25}$$

$$\epsilon_{ij} = \sqrt{\epsilon_i\epsilon_j}(1 - k_{ij}) \tag{3.26}$$

Where k_{ij} is the binary interaction parameter. For more information on the derivation of the PC-SAFT EoS equations, the reader is directed to the original publications of the model [Gross and Sadowski, 2002][Gross and Sadowski, 2001] and Appendix A. The input parameters required for conducting PC-SAFT computations include the number of chain segments (m), the segment diameter (σ), and the depth of the pair potential divided by the Boltzmann

constant (ϵ/k), as shown in Fig. 3.1.

Each component must be individually defined with these parameters. Adjusted values based on empirical density and vapour pressure data can be found in the literature [Gross and Sadowski, 2002][Tumakaka and Sadowski, 2004]. However, to be consistent with our previous work [Geber et al., 2023], this study introduces a more universal and predictive approach. Therefore, we employ a Group Contribution (GC) method to estimate these input parameters. In this study, we have implemented the GC method as proposed in [Tihic et al., 2008]. This method, which has demonstrated satisfactory results in previous applications, dissects the molecular structure into simpler first-order groups and more complex second-order groups. The PC-SAFT parameters (m, σ, and ϵ/k) are then calculated by accounting for the individual contributions from each group (m_i, σ_i, and ϵ/k_i), as demonstrated in Eqs. 3.27, 3.28, and 3.29.

$$m = \sum_{i}^{ngroups} (n_i m_i)_{FOG} + \sum_{i}^{ngroups} (n_i m_i)_{SOG} \tag{3.27}$$

$$m\sigma = \sum_{i}^{ngroups} (n_i m_i \sigma_i^3)_{FOG} + \sum_{i}^{ngroups} (n_i m_i \sigma_i^3)_{SOG} \tag{3.28}$$

$$m\frac{\epsilon}{k} = \sum_{i}^{ngroups} (n_i m_i \frac{\epsilon}{k_i})_{FOG} + \sum_{i}^{ngroups} (n_i m_i \frac{\epsilon}{k_i})_{SOG} \tag{3.29}$$

When dealing with associating components, identifying the type of bonding is necessary. In their study focusing on alkanols, [Huang and Radosz, 1990] recommend the use of both 3B and 2B bonding models. However, due to the absence of a persuasive case for using the more intricate 3B model, this study opts for the simpler 2B approach. Additionally, the 2B model has been successfully utilised by [Gross and Sadowski, 2002] to characterise compounds such as ethanol, methanol, and pentanol, among others. Two further parameters pertaining to pure components, namely the effective association volume (k^{AB}) and the association energy (ϵ^{AB}/k), are employed for associating components. These parameters can also be calculated using the GC method proposed in

[Tihic et al., 2008]. Finally, the Quantitative Structure–Property Relationship (QSPR) method introduced in [Stavrou et al., 2016] was applied to estimate the binary interaction parameter (k_{ij}).

$$k_{ij}^{QSPR} = \sum_{L=1}^{N_d} c_L D_L(\bar{p_i}, \bar{p_j}) \tag{3.30}$$

Where N_d represents the number of descriptors, and $D_L(\bar{p_i}, \bar{p_j})$ are the descriptors with corresponding regression coefficients c_L. As pointed out in [Gross and Sadowski, 2002], the PC-SAFT EoS is applicable to mixtures of small spherical molecules, such as gases, non-spherical solvents, and chain-like polymers. Moreover, when applied to vapour–liquid equilibria of mixtures, the equation of state demonstrates substantial predictive capability and good accuracy for correlating mixtures. Finally, it is noted that the applicability of the proposed model to polymer systems was demonstrated for high-pressure liquid–liquid equilibria of a polyethylene mixture. The pure-component parameters of polyethylene were obtained by extrapolating the pure-component parameters of the n-alkane series to high molecular weights.

3.5 Vapour Liquid equilibrium (VLE) calculations

The methodology detailed and validated in Geber et al. [Geber et al., 2023] and Vidal et al. [Vidal et al., 2020] that is used to create a 3D thermodynamic table (see Section 3.8 for more details), has been made more efficient via parallelisation in the current project. In particular, parallelisation is required to construct the thermodynamic table that will then be used by the numerical solver. With the use of OpenMP, the table formulation requires 2 days instead of weeks for serial calculations.

The algorithm featured in the work of Vidal et al. [Vidal et al., 2020] and used by Geber et al. [Geber et al., 2023] leverages the PC-SAFT EoS to evaluate the stability of a homogeneous mixture, given a particular composition, density, and temperature. In situations where instability is detected, the algo-

rithm determines the vapourised portion of the substance, the compositions of both phases, as well as the resultant equilibrium pressure through a TV-flash calculation.

The TV-flash can be seen as an algorithm in which volume and temperature are used as independent variables to minimise the Helmholtz free energy rather than the Gibbs free energy (as in the PT-flash algorithm) for the multiphase problem [Vidal et al., 2020]. A homogeneous mixture at a given temperature T is considered stable if the tangent plane, drawn at the composition z and density ρ on the Helmholtz free energy surface, does not intersect this energy surface at any other location. To verify stability, the homogeneous mixture is intentionally partitioned into two phases, with one phase existing in a nominal or minute amount, referred to as the trial phase. If there is no reduction in the Helmholtz free energy for any potential two-phase combination, then the mixture is recognised as stable. The tangent plane distance (TPD) function employed is defined in Eq. 3.31.

$$TPD = \frac{P' - P^*}{RT} + \sum_{t=1}^{nc} \rho' x_i' (\ln f_i' - f_i^*) \tag{3.31}$$

The variables represented with primes correspond to values calculated under trial conditions, while those with an asterisk indicate values calculated under feed conditions. R stands for the universal gas constant, and f_i refers to the fugacity of component i. The initialisation of the iterative minimisation process incorporates Raoult's law and Wilson's correlation [Wilson, 1969], along with the work of Michelsen [Michelsen, 1982b] and Mikyska and Firoozabadi [Michelsen, 1982a]. This combination allows the derivation of an expression for the initial composition of the liquid phase (represented as l_i) and the vapour phase (represented as ν_i). Here, z_i denotes the total initial composition, as shown in Eqs. 3.32 and 3.33.

$$\nu_i = \frac{z_i P_{ini}}{P_i^{sat}} = \frac{z_i}{P_i^{sat}(\sum_{i=1}^{n_c} \frac{z_i}{P_i^{sat}})} \tag{3.32}$$

$$l_i = \frac{z_i P_i^{sat}}{P_{ini}} = \frac{z_i P_i^{sat}}{\sum_{i=1}^{n_c} z_i P_i^{sat}} \tag{3.33}$$

If a two-phase regime is identified during the stability analysis, the algorithm continues by performing TV-flash calculations, where the objective is to minimise the Helmholtz energy for a given density, temperature, and composition. In both the stability analysis and flash calculations, Newton's method is employed to solve the optimisation problem. To determine the step length in the Newton method, an inexact line search is conducted. This search aims to find a step length that satisfies the Wolfe conditions [Nocedal and Wright, 2006]. Equation (3.34) needs to be solved to calculate the direction (p_k) followed in the search for the optimal solution.

$$\nabla^2 f_k p_k = -\nabla f_k \tag{3.34}$$

The equation involves the Hessian ($\nabla^2 f_k$) and the gradient (∇f_k) of the objective function. To guarantee the positive definiteness of the Hessian matrix, we employ a modified Cholesky factorisation algorithm [Schnabel and Eskow, 2006]. For a more detailed explanation of the methodology, please refer to [Harvey and Lemmon, 2004]. The thermodynamic closure has been validated thoroughly for various types of multi-component fuel mixtures, as demonstrated in a previous study by the authors' group [Vidal et al., 2020]. The present investigation implements it successfully within the framework of a density-based flow solver in OpenFOAM V7.

3.6 Calculation of Thermal Conductivity

Following up on the work from our group at City, University of London focusing on hydrocarbon mixtures [Koukouvinis et al., 2020], we are employing the same residual entropy scaling method [Hopp and Gross, 2017] for the calculation of thermal conductivity in the present investigation. Within this approach, the thermal conductivity is normalised using a benchmark value, represented as λ_{ref}, which is uniquely tailored for each component, as detailed in Eq. 3.35.

$$\lambda_i^{ref} = \lambda_{CE,i}^{ref} + a(s^*)\lambda_i^{correct} \tag{3.35}$$

In the above equation, $\lambda_{CE,i}^{ref}$ represents the Chapman-Enskog formula for thermal conductivity, which is mainly applicable to monoatomic gases. The element $\lambda_i^{correct}$ serves as an adjustment parameter for polyatomic fluids. Additionally, $a(s^*)$ is defined as a transitional function, detailed as follows:

$$a(s^*) = \exp\left(\sum_{i=1}^{n_c} \frac{-s^{res}}{\sum_i^{n_c} x_i s_{c,i}^{res}}\right) \tag{3.36}$$

In this context, x_i denotes the mole fraction of the i-th component in a mixture comprising n_c components. The term s_{res} represents the residual entropy, and $s_{c,i}^{res}$ signifies the residual entropy value of component i at its critical point.

$$s^{res} = -T\frac{\partial a_{\text{res}}}{\partial T} - \widetilde{a}^{res} \tag{3.37}$$

Following this, the dimensionless thermal conductivity, represented by λ^*, is computed as a function of the normalised residual entropy, denoted as s^*, following Eq. 3.38

$$\ln(\lambda^*) = \ln\frac{\lambda}{\lambda^*} + A_{\text{mix}}^{\lambda} + B_{\text{mix}}^{\lambda} s^* + C_{\text{mix}}^{\lambda}(1 - \exp(s^*)) + D_{\text{mix}}^{\lambda}(s^*)^2 \tag{3.38}$$

In Eq. 3.38, the reduced residual entropy is calculated by using the mean segment number, represented by $\bar{m}$, which is the sum of the products of the mole fraction x_i and segment number m_i for each of the n_c components:

$$s^* = \frac{s^{\text{res}}}{\bar{m}} \tag{3.39}$$

Initially, the entropy scaling method was employed exclusively for individual components. Hence, in this research, mirroring the approach in [Koukouvinis et al., 2020], an empirical mixing rule has been applied to both the coefficients and the reference thermal conductivity. The empirical mixing rule refers to a method where, instead of calculating the thermal conductivity for each species separately and then averaging them, a mixing rule is applied directly to the mathematical coefficients that define the thermal conductivity correlations, following Eq. 3.40

$$X_{\text{mix}} = \frac{\sum_{i=1}^{n_c} x_i m_i \sigma_i^2 X_i}{\sum_{i=1}^{n_c} x_i m_i \sigma_i^2} \tag{3.40}$$

In this equation, X can represent any one of the coefficients $A^\lambda, B^\lambda, C^\lambda, D^\lambda$, or λ_{ref}. If the mixture conditions lie within the VLE regime, the mixing rule becomes a weighted average operation, using the vapour volume fraction, denoted by α_g, along with the thermal conductivities for the liquid and gas phases, expressed as λ_l and λ_g, respectively, in Eq. 3.41.

$$\lambda_{\text{VLE}} = \alpha_g \lambda_g + (1 - \alpha_g)\lambda_l \tag{3.41}$$

3.7 Calculation of Viscosity

Lotgering-Lin and Gross [Lotgering-Lin and Gross, 2015] applied the entropy scaling model for computing dynamic viscosity as well [Rosenfeld, 1977]. For a singular component, the reduced dynamic viscosity, symbolised by μ_i^*, can be calculated using Eq. 3.42.

$$\ln \mu_i^* = A_i^\lambda + B_i^\lambda s^* + C_i^\lambda (s^*)^2 + D_{mix}^\lambda (s^*)^3 \tag{3.42}$$

The methodology for determining the value of the mixture is specified in [Vidal et al., 2018]. If the mixture is in a VLE state, the mixing rule provided by Beattie and Whalley [Beattie and Whalley, 1982] is used, and it is shown in Eq. 3.43

$$\mu_{\text{VLE}} = \alpha_g \mu_g + (1 - \alpha_g) \left(1 + \frac{5}{2\alpha_g}\right) \mu_l \tag{3.43}$$

3.8 Structure of the Thermodynamic-Closure Table

In the context of highly turbulent multi-component simulations, when using explicit density-based diffuse interface solvers, the impact of species diffusion terms in the energy and continuity equations is often considered negligible.

This assumption arises primarily due to the robust convective mixing that characterises turbulent simulations, which significantly overshadows any diffusion effects. This model simplification enables the utilisation of just two continuity equations: one to monitor the multi-component fuel mixture and the other to track the mixture of fuel and ambient gas. By using these two equations, it is possible to consolidate all essential information regarding the properties of the working fluids into a three-dimensional table, organised by fuel mass fraction, density, and internal energy.

Indeed, the procedure described in the Thermodynamic Closure Section (Section 3.4) can be performed on the fly during code execution. However, it requires root-finding of non-linear equations, since the Helmholtz energy is naturally expressed as a function of density ρ and temperature T, whereas the newly developed solver calculates density ρ and internal energy e, as shown in Eqs. 3.1, 3.3, 3.5. Moreover, one would also need to determine whether the flow is at saturation conditions or not. In other words, at each time step, the conservative variables (ρ, ρE) must be transformed to (ρ, T) and then used to derive pressure and speed of sound for the next calculation step. This can be done using, for example, the Newton–Raphson method, but it is very time-consuming. As a consequence, a similar technique to that employed by [Dumbser et al., 2013] has been adopted, instead of solving the PC-SAFT EoS at each time step.

In the present work, a structured 3D thermodynamic table has been used, which was constructed prior to the simulations and contains all the thermodynamic properties derived from the PC-SAFT EoS, including temperature, pressure, specific heat, viscosity, speed of sound, and vapour fraction. In this way, the mismatch between the variables required as input in the PC-SAFT EoS (p, T) and those calculated from the Navier-Stokes equations (ρ, E) is handled through numerical inversion.

The thermodynamic table for each material is built by selecting an appropriate range for density and internal energy: $\rho_{min} \leq \rho \leq \rho_{max}$, $e_{min} \leq e \leq e_{max}$, $0 \leq Y \leq 1$, which defines a 3D table enclosing the expected conditions for each simulation. An example of a 3D table is given in Fig. 3.2, where water

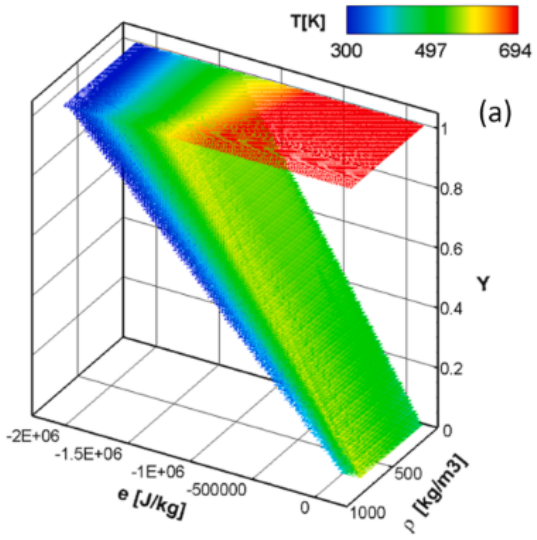

Figure 3.2: Example of a structured 3D Thermodynamic table for water, showing liquid and vapour areas depending on density, vapour fraction, and internal energy.

is considered. Table points are evenly distributed on a linear scale, with 1000 points for density and internal energy, and 100 points for fuel mass fraction.

During algorithm execution, after calculating the conservative vector in the time loop, the density, mass fraction, and internal energy are known. The element of the thermodynamic grid corresponding to each cell of the computational domain can then be determined by employing a static linked-list algorithm. Trilinear interpolation is used within each cell of the domain. Using finite-element trilinear interpolation, any thermodynamic property in the table can be extracted. The extracted property can be either pressure, temperature, or speed of sound, which are needed for flux calculations, or any other property, such as enthalpy or entropy, required during post-processing.

Developing this 3D table presents the challenge of including only physically meaningful and relevant thermodynamic states of the mixture. To address this, realistic minimum and maximum values of density and internal energy for each fuel mass fraction are determined and used to construct the table, taking into account the specific scenarios where it will be applied. These limits are set to ensure the table is suitable for all conditions expected in the relevant simulation and to provide a safety margin beyond the CFD-predicted density and internal energy values. If the table bounds are exceeded during the simulation, instability may occur. More details on the table construction can

be found in [Geber et al., 2023] and Appendix A. Finally, as noted in [Kyriazis et al., 2017], [Bellini et al., 2024], and [Bellini et al., 2025], constructing the thermodynamic table prior to the simulations is almost an order of magnitude more efficient than calculating the PC-SAFT EoS on the fly.

Chapter 4

Solver Validation and Cluster of Bubbles

In this Chapter, the numerical model is first validated against the exact solution of the Riemann problem and the Rayleigh collapse test case (based on the Rayleigh–Plesset Eq. 2.1). Subsequently, a numerical experiment of bubble collapse is performed, and finally, a validation against published data [Ghahramani et al., 2019] for a cluster of bubbles is presented. The Riemann problem was chosen to validate the spatial accuracy of the algorithm and to demonstrate its capability to capture the correct wave pattern. The Rayleigh collapse test case was selected to assess the time advancement of the Runge–Kutta implementation, as well as the thermodynamic validity of the model.

Once the algorithm has been validated with these simple cases, three single-bubble collapse simulations in the vicinity of a wall were conducted. As discussed in Chapter 2.2, many bubble collapse simulations exist in the literature; however, there has been no investigation into the effect of accurate thermodynamics of the fluid involved [Kyriazis et al., 2017]. Finally, following validation of the cluster-of-bubbles case against published data, simulations with different fuels were performed to illustrate how cavitation, and more specifically the peak pressures, is influenced by fuels with distinct properties, such as dodecane and short-chain alcohols.

4.1 Shock Tube Case - Validation against Riemann Problem

In this section, a comparison between the results obtained with the solver presented herein and the Riemann problem [Toro, 2009] [LeVeque, 2004] is presented.[1] More details on the analytical solution of the Riemann problem are available in Appendix D. The goal of this section is to validate the new multiCompTabFoam solver against analytical results.

The geometry employed in this problem consists of a simple 1D shock-tube domain, $x \in [0, 4]$, which has been meshed with 1000 equally spaced cells in the x direction. The fluid considered is dodecane, and the initial conditions are listed in Tab. 4.1. Additionally, wave-transmissive boundary conditions have been applied to both ends of the shock-tube to prevent pressure wave reflections that could affect the results.

Variable	Left Section	Right Section
x	[0,2]	[2,4]
ρ	751.737 kg/m^3	717.5 kg/m^3
e	$-510\,935.125$ J/kg	$-378\,498.706$ J/kg
p	76 668.0 Pa	10 912 000 Pa
T	290 K	350 K

Table 4.1: Initial conditions for the 1D shock tube problem.

The results obtained with `multiCompTabFoam` are then compared with the exact solution of the Riemann problem.

As can be seen in Fig. 4.1, the exact solution of the Riemann problem and the computed results are in satisfactory agreement, and the wave pattern has been correctly captured. The numerical results were taken as soon as the solution reached its steady state conditions.

To give a more quantitative result view, the average errors in all Fig. 4.1 are less than 1%. In particular, far from the shocks, which is the vast majority of

[1] A significant portion of this chapter is published as: R. Bellini, C. Rodriguez, I. K. Karathanassis, M. Gavaises, "Cavitation Dynamics and Surface Erosion in Fuel Injectors, Considering the Composition of Fuel Mixtures", Computers & Fluids, 2025, under the terms of the Creative Commons Attribution 4.0 license (CC BY 4.0). The author of this dissertation has contributed to the methodology, validation, data curation, formal analysis, investigation, writing, and visualisation of the article.

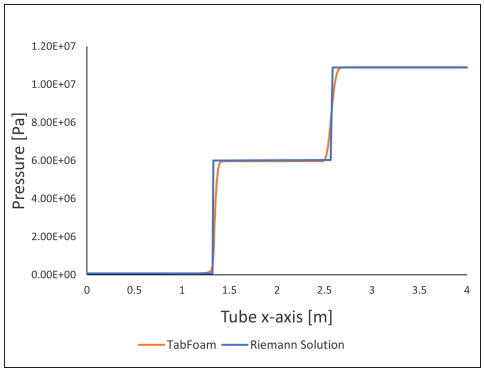

(a) Pressure comparison

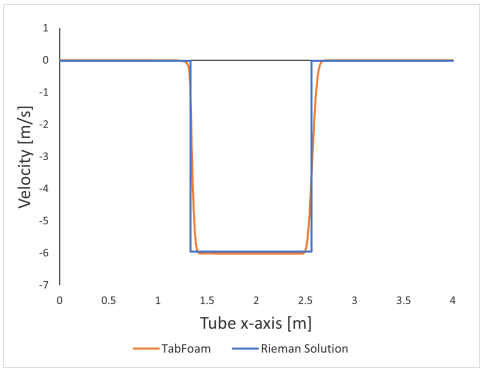

(b) Velocity comparison

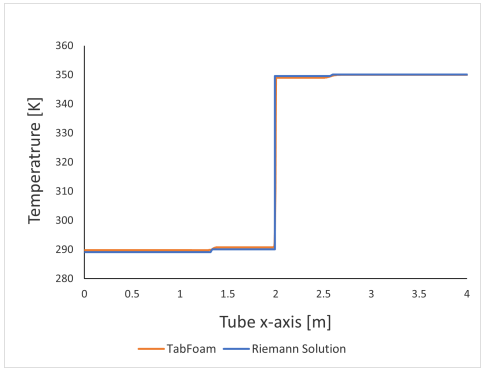

(c) Temperature comparison

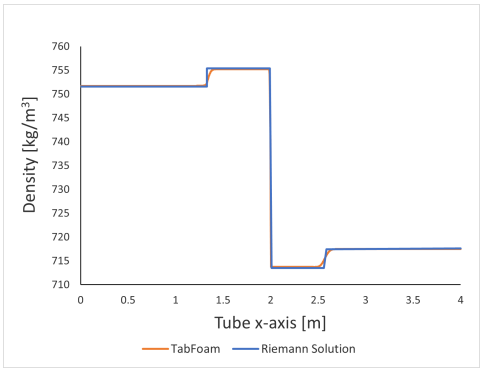

(d) Density comparison

Figure 4.1: Comparison among results obtained with `multiCompTabFoam` and the exact solution of the Riemann problem for: (a) Pressure, (b) Velocity, (c) Temperature, (d) Density.

the tube geometry, the error is near zero. At the shocks, Pressure and Velocity present the higher errors, which are approximately 2.4% for Pressure and 3.1% for the Velocity. Overall we can conclude that the simulation performed with the new solver is accurate on the steady values and introduces some numerical diffusion at the shock waves.

4.2 Rayleigh Bubble Collapse

The second test case examined in this work is the Rayleigh bubble collapse, compared with the Rayleigh-Plesset equation (Eq. 2.1). Indeed, the goal of this section is to simulate an isolated bubble located far from any boundary and compare the collapse dynamics with an analytical solution.

In this case, an isolated vapour sphere of radius $R = 400\mu m$, located far from any solid surface, is subjected to compression due to the higher pressure of the surrounding liquid. As stated previously (and shown in the first case of Fig. 2.2), when an isolated bubble collapses, a shock wave is generated and propagates symmetrically in the surrounding liquid. Therefore, the problem can be considered symmetric. Taking advantage of this spherical symmetry, a two-dimensional geometry was employed for the simulation using a wedge boundary condition. A wedge boundary condition is used to define an axisymmetric simulation, allowing a 3D problem to be solved using a computationally efficient 2D slice. Instead of a full cylinder being meshed, a thin "slice of cake" is utilised (for this simulation, a 5° angle was used), and the wedge condition is applied to the front and back faces. The solver is thereby informed that the flow is rotationally symmetric around the central axis. A sketch of the domain is provided in Fig. 4.2 (X-Z plane) and Fig. 4.3 (X-Y plane).

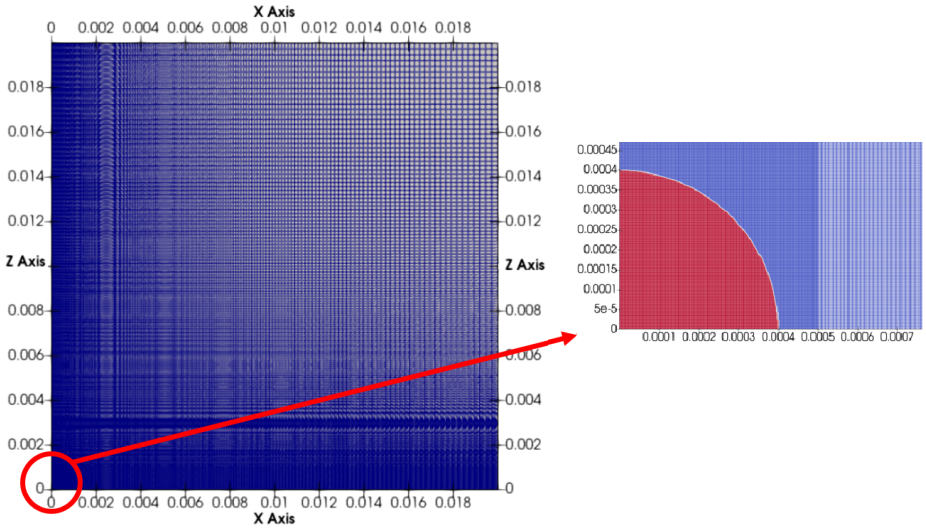

Figure 4.2: X-Z plane view of the geometry for the Rayleigh bubble collapse case.

The bubble's centre is located at the origin of the domain, i.e., at $x = 0$,

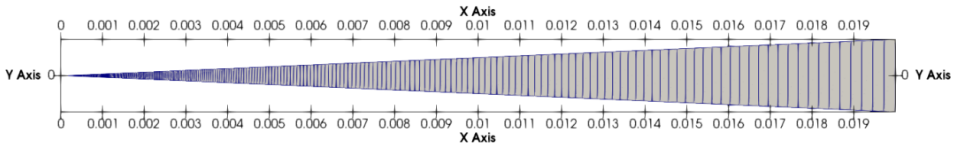

Figure 4.3: X-Y plane view of the geometry for the Rayleigh bubble collapse case.

$y = 0$, and $z = 0$. The total computational domain is *50* times the size of the initial vapour radius (i.e., 8 mm from the centre of the bubble) to minimise interference from the boundaries. Additionally, the mesh is refined in the bubble region (defined as $2.5\,R$), where *1000* equally spaced cells have been used, while a stretching ratio of *1.05* with *1000* cells has been applied outside the bubble region. A wave-transmissive boundary condition is applied at the far-field right and top sides, and symmetry conditions are used for the left and bottom sides to simulate the axis of the wedge. In particular, in OpenFOAM, a wave-transmissive boundary condition (specifically waveTransmissive) is a boundary condition designed to allow pressure waves to exit the computational domain without reflecting back. Specifically, the waveTransmissive condition calculates the wave speed at the boundary and adjusts the pressure values to ensure that outgoing disturbances simply "pass through".

The fluid is pure Dodecane, and the specific initial conditions for this case are specified in Tab. 4.2. In particular, Dodecane has been selected since it is the most common fuel utilised for simulating cavitation inside fuel injectors.

Variable	Vapour Condition	Liquid Condition
ρ	$0.0015\,\mathrm{kg/m^3}$	$744.36\,\mathrm{kg/m^3}$
e	$-142\,760\,\mathrm{J/kg}$	$-488\,540\,\mathrm{J/kg}$
p	$19.64\,\mathrm{Pa}$	$101\,325\,\mathrm{Pa}$

Table 4.2: Initial conditions for the Rayleigh Bubble Collapse.

In this specific case, the characteristic Rayleigh time $\tau = 31.5\mu s$.

The result for this section is shown in Fig. 4.4, where the comparison with the semi-analytical solution (Eq. 2.1) gives satisfactory results. This highlights that the current methodology is able to predict the correct trend of the bubble radius evolution with respect to time and dynamics. To obtain this "dimensionless" graph, the radius has been normalised by the initial radius

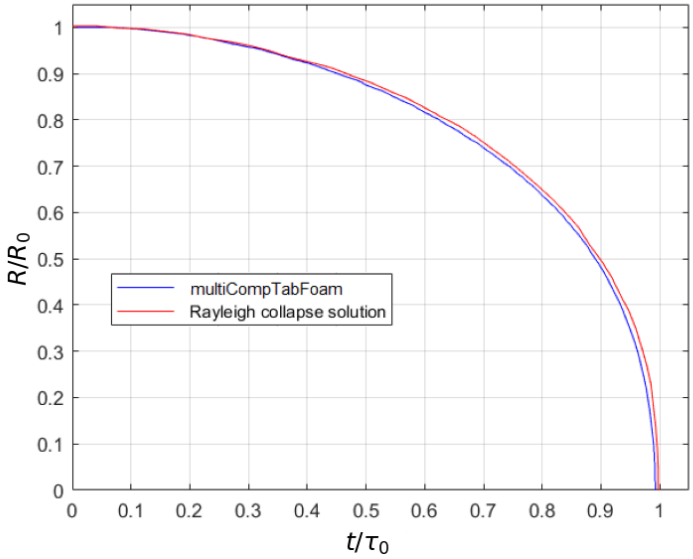

Figure 4.4: Comparison between the Rayleigh collapse solution and multiCompTabFoam

$R_0 = 400\,\mu$m, and the time has been made dimensionless by dividing it by the Rayleigh time (τ_0).

4.3 Single Bubble Collapse near a Solid Surface

Following the work of [Trummler et al., 2021], the collapse of a water vapour bubble in the vicinity of a wall is investigated in this section.[2]

In all configurations, the bubble radius is $R = 400\,\mu$m. The difference among the four cases is the distance of the bubble centre from the wall (defined as the Stand-Off Distance, SOD), as shown in Fig. 4.5. In particular, the SOD is expressed relative to the initial radius of the bubble and the wall, as explained in Chapter 2.1.1.

The four cases presented in this section are:

- **Case 1**: $SOD = 0$

[2]A significant portion of this chapter is published as: R. Bellini, C. Rodriguez, I. K. Karathanassis, M. Gavaises, "Cavitation Dynamics and Surface Erosion in Fuel Injectors, Considering the Composition of Fuel Mixtures", Computer & Fluids, 2025, under the terms of the Creative Commons Attribution 4.0 license (CC BY 4.0). The author of this dissertation contributed to the methodology, validation, data curation, formal analysis, investigation, writing, and visualisation of the article.

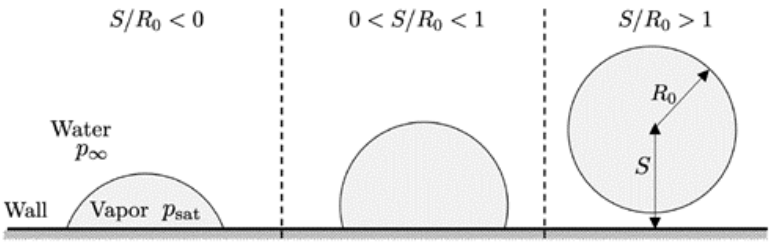

Figure 4.5: Initial SOD cases for a simple bubble collapse close to a solid surface[Trummler et al., 2021]

- **Case 2**: $SOD = 0.35R_0$
- **Case 3**: $SOD = -0.35R_0$
- **Case 4**: $SOD > 1R_0$

The exact same mesh as in the previous case has been employed (see Fig. 4.2). Symmetry can still be used, as the most important wave features are well captured in the observed plane. However, in this study, the bottom side is set as a rigid wall. The bubble centre moves along the y coordinate, while its position with respect to x and z is kept constant for all four SOD cases.

The initial conditions for the four cases are identical and are specified in Tab. 4.3.

Variable	Vapour Condition	Liquid Condition
ρ	$1.60\,\mathrm{kg/m^3}$	$1002.7\,\mathrm{kg/m^3}$
e	$108\,949.94\,\mathrm{J/kg}$	$83\,307.60\,\mathrm{J/kg}$
p	$2340\,\mathrm{Pa}$	$100\,\mathrm{MPa}$

Table 4.3: Initial conditions for a single bubble collapse close to a solid surface[Kyriazis et al., 2017].

In addition to that, the pressure field for the liquid component has been initialised using a Laplacian distribution which follows Eq. 4.1.

$$P(r, t = 0) = p_{sat,l} + \Delta p \frac{r - R_0}{r} \qquad \text{for } r > R_0 \tag{4.1}$$

This Laplacian distribution for pressure, as extensively reported in the literature [Kyriazis et al., 2017], is reasonable for stationary conditions, since the smooth transition from vapour pressure to a high-pressure liquid condition

is more realistic than a step-change distribution. Δp is essentially the linear interpolation coefficient required to transition from $p_{sat,l}$ to the pressure at the wall (i.e. 100×10^6 in this case) across the space between the bubble surface and the wall. This initialisation matches the pressure distribution predicted by the Rayleigh–Plesset equation for the Besant problem [Brennen, 2005] [Besant, 1859]. For the configurations considered, it provides a valid approximation of the realistically evolving pressure field and suppresses the formation of spurious pressure waves caused by pressure jumps at the bubble interface.

The dimensionless bubble volume and pressure evolution, shown in the following 4 subsections, have been compared against published data by Trummler et al. [Trummler et al., 2021], where a fully compressible two-phase flow solver including phase change was used. In particular, the cavitation model of the referenced study is based on the assumption that the liquid and gas phase of a cavitating liquid are in thermal and mechanical equilibrium. Then, the thermodynamic model is embedded into a density-based fully compressible flow solver with a low-Mach-number-consistent flux function. Specifically, two different equations of state were used for the pure liquid and the liquid-vapour mixture: the pure liquid was modelled using a modified Tait equation, while the EoS for the two-phase region ($p < p_{sat}$) was derived from the definition of the isentropic speed of sound, where equilibrium phase change is assumed. It should be noted that viscous effects were also considered in the referenced study. An upwind biased scheme is used for the reconstruction at the cell faces, where the velocity components are reconstructed with the up to third-order-accurate limiter of Koren and the thermodynamic quantities ρ, p with the second-order Minmod slope limiter of Roe. Finally, Time integration is performed with an explicit second-order, 4-step low-storage Runge–Kutta method. The domain was discretised with a resolution of $240c/R_0$, comparable to the one used in this thesis.

In all plots presented in the next section, time is expressed in its dimensionless form (i.e. divided by the Rayleigh time $\tau = 4.006 \times 10^{-6}\,\mathrm{s}$). Similarly, pressure is presented in dimensionless form by dividing its value by p^*, as defined in Eq. 4.2.

$$p^* = c_L \sqrt{rho_L * (p_L - p_V)} \tag{4.2}$$

Lastly, to capture the pressure peaks at the wall, a simulation probe is located at the coordinates $(0, 0, 0)$ and samples data at every time step of the simulation, in accordance with Trummler et al. [Trummler et al., 2021].

4.3.1 Case 1: $SOD = 0$

Fig. 4.7 shows the time sequence of a wall-attached bubble collapsing. It is evident that the bubble uniformly shrinks and collapses at its centre, and this is evident if we look at the velocity vectors and which are all pointing to the centre of the bubble as shown in Fig. 4.7. Similarly, the collapse generates a symmetrical shock wave. Indeed, this is what one would expect given that the surrounding pressure and velocity fields are perfectly symmetric. The results obtained with `multiCompTabFoam` are in agreement with [Trummler et al., 2021], as shown in Fig. 4.6.

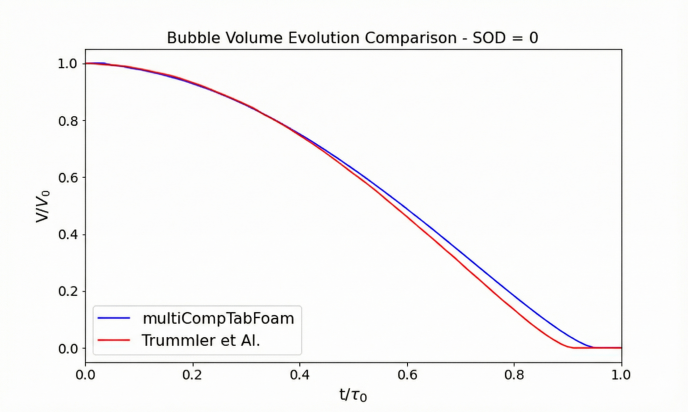

(a)

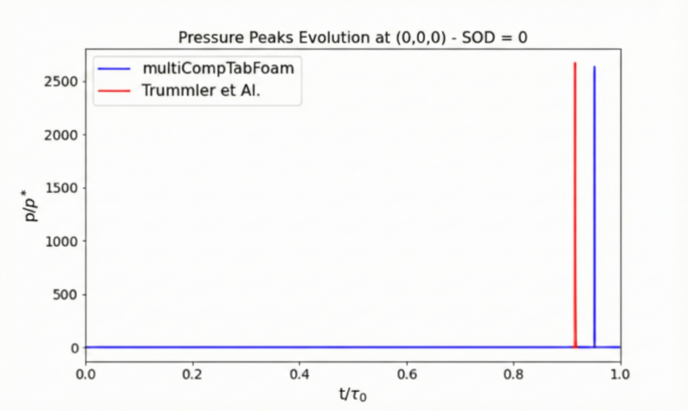

(b)

Figure 4.6: (a) Bubble volume evolution and (b) pressure evolution for $SOD = 0$

4.3.2 Case 2: $SOD < 0$

Fig. 4.9 shows the time sequence of a bubble whose centre is below the wall, i.e. $SOD < 0$. As explained in the introduction, due to the surface tension of the bubble and the velocity field during the collapse, the bubble develops a mushroom shape (as shown in Fig. 4.9b), which leads to a strong initial collapse caused by the encounter of the lateral jets piercing the bubble. Fig. 4.9b also highlights the higher velocity and pressure at the sides of the bubble, which are responsible for the mushroom shape. Finally, the re-entrant jet is also visible in Fig. 4.9c. Looking at the time-to-collapse and pressure peak results (Fig. 4.8), the results obtained with `multiCompTabFoam` are in acceptable agreement with Trummler et al results. [Trummler et al., 2021].

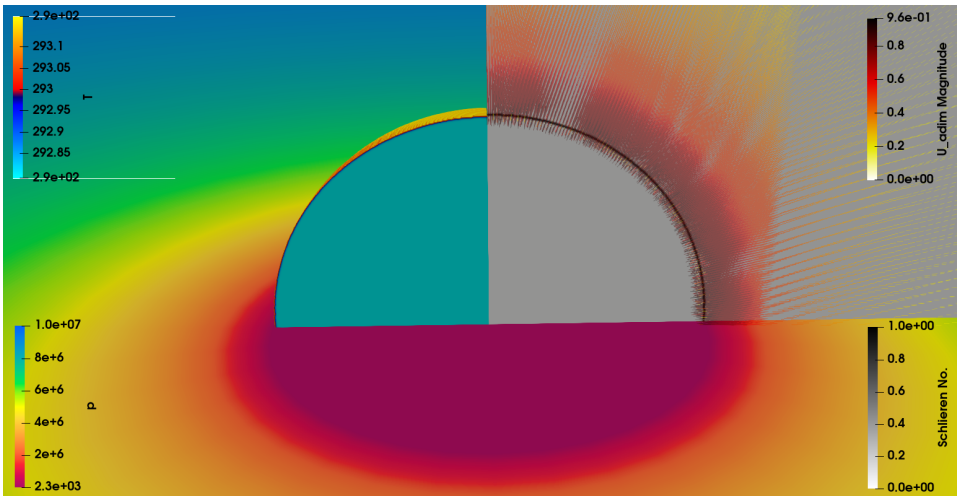

(a) t/τ_0 =0

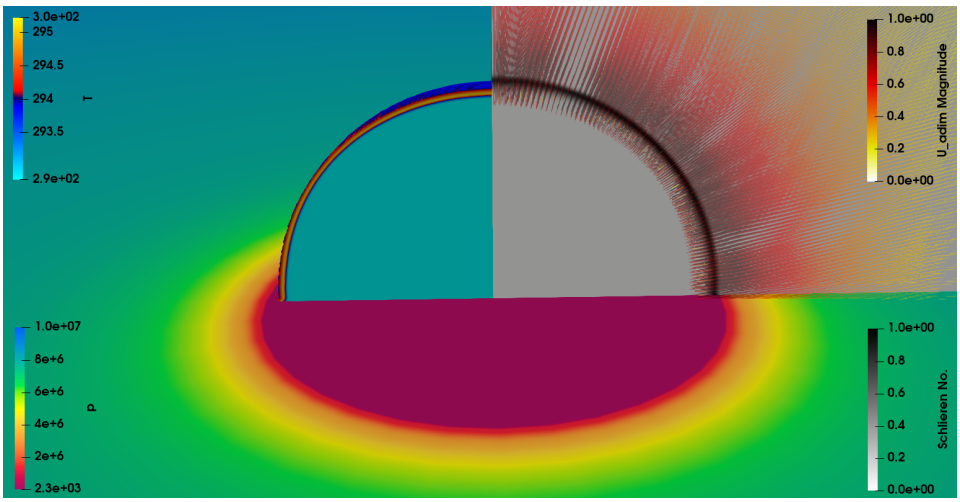

(b) t/τ_0 =0.75

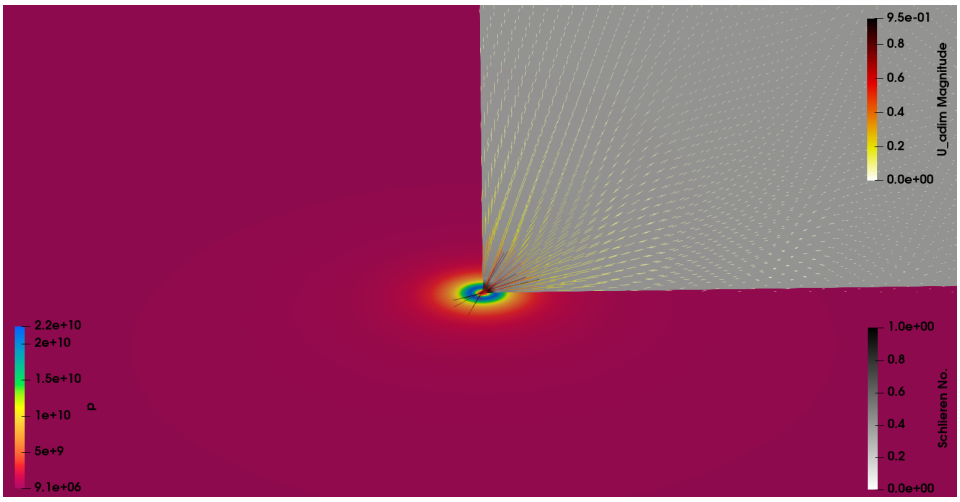

(c) t/τ_0 =0.95

Figure 4.7: pressure, temperature, velocity vectors, and schlieren images for bubble at $SOD/R_0 = 0$ at three different time steps: (a) t/τ_0 =0, (b)) t/τ_0 =0.75, and (c)) t/τ_0 =0.95

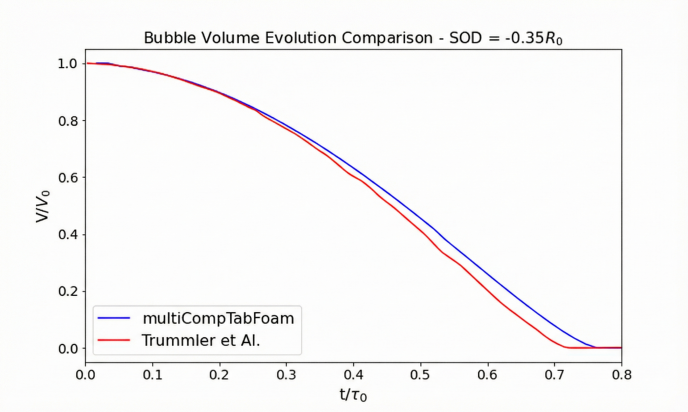

(a)

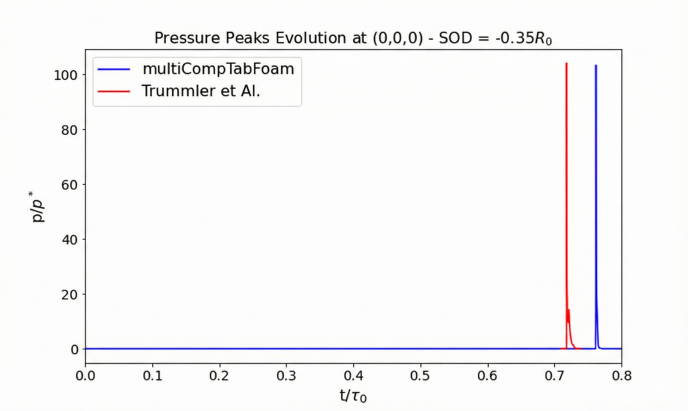

(b)

Figure 4.8: (a) Bubble volume evolution and (b) pressure evolution for $SOD = -0.35R_0$

4.3.3 Case 3: $0 < SOD < R$

Fig. 4.11 shows the time sequence of a bubble with $0 < SOD < 1$, i.e. where the bubble is not completely detached from the wall. As expected in this case, due to the pressure asymmetry in the flow field, as the bubble starts to shrink, a jet develops and tries to pierce the bubble from the top (Fig. 4.11b). This causes an initial collapse driven solely by the re-entrant jet, resulting in the toroidal shape shown in Fig. 4.11c. As time progresses, the entire bubble collapses, generating higher pressure peaks (Fig. 4.10b). Once again, the results obtained with `multiCompTabFoam` are in agreement with Trummler et al results.[Trummler et al., 2021], as shown in Fig. 4.10.

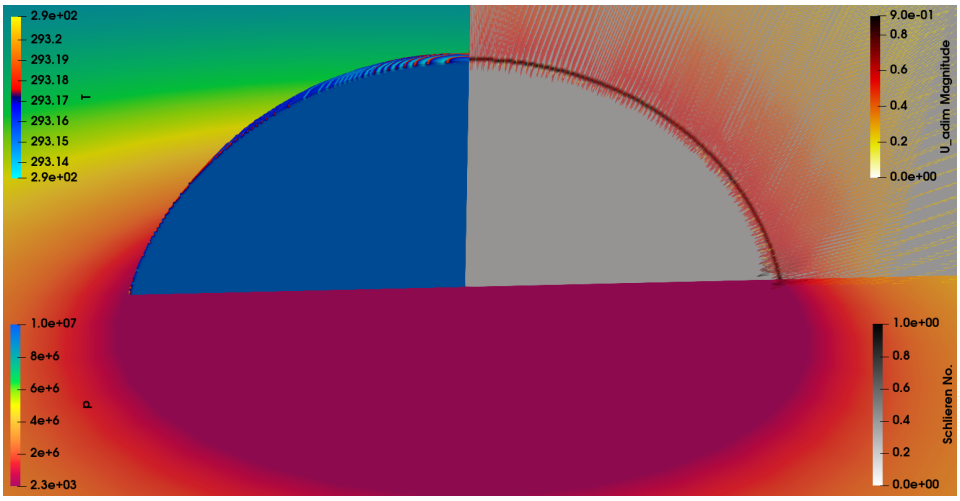

(a) t/τ_0 =0

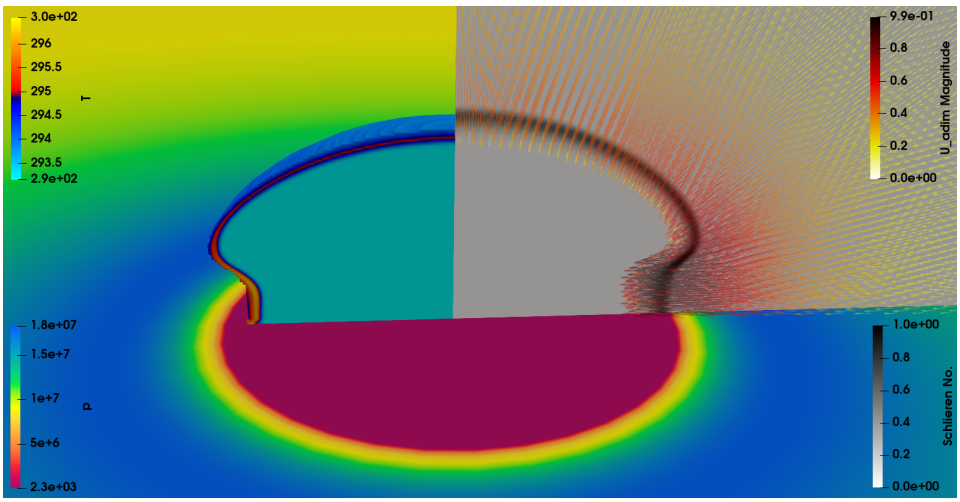

(b) t/τ_0 =0.7

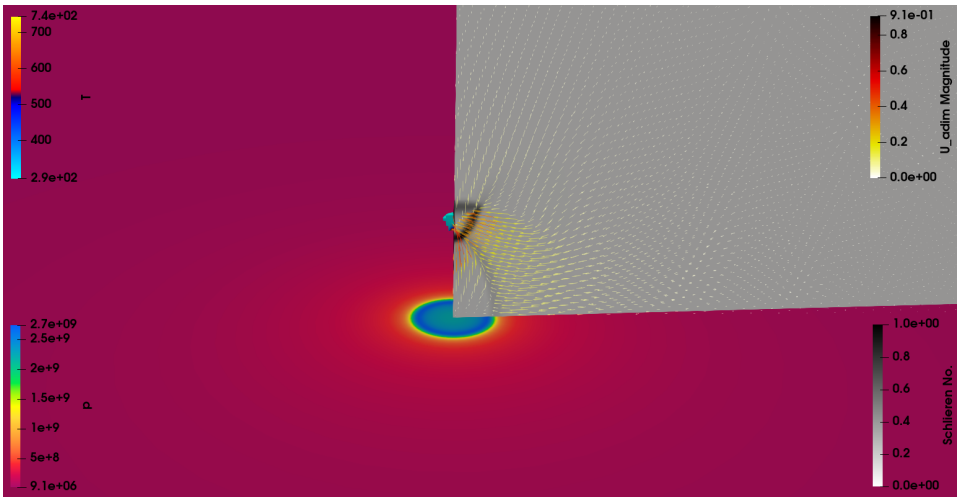

(c) t/τ_0 =0.76

Figure 4.9: Pressure, temperature, velocity vectors, and schlieren images for bubble at $SOD/R_0 = -0.35$ at three different time steps: (a) t/τ_0 =0, (b)) t/τ_0 =0.7, and (c)) t/τ_0 =0.76

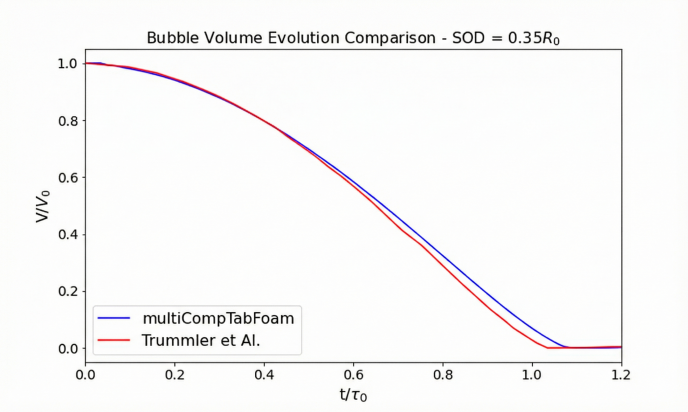

(a)

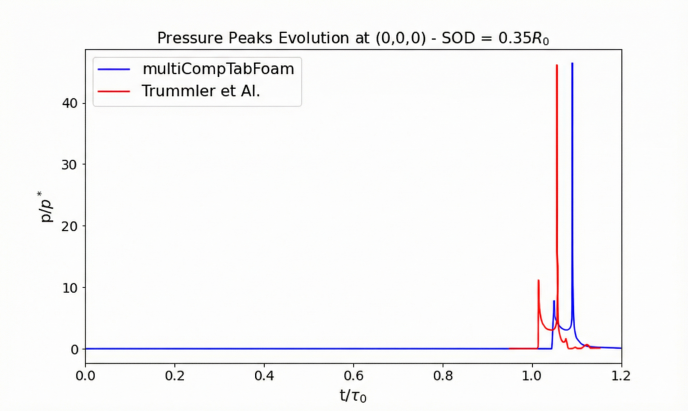

(b)

Figure 4.10: (a) Bubble volume evolution and (b) pressure evolution for $SOD = 0.35R_0$.

4.3.4 Case 4: $SOD > 1$

Lastly, Fig. 4.13 shows the time sequence of a bubble completely detached from the wall collapsing. In this case, due to a higher pressure field in the top part of the bubble relative to its bottom part, a velocity gradient is created, which eventually pierces the bubble from above (Fig. 4.13b). This re-entrant jet causes an initial weak detached collapse, allowing for a vapour rebound, as shown in Fig. 4.12a. This rebounded vapour bubble eventually collapses again. Such behaviour could be particularly hazardous in an injector, as, alongside the strength of a collapse, the repetition (and frequency) of weaker collapses also contributes to erosion.

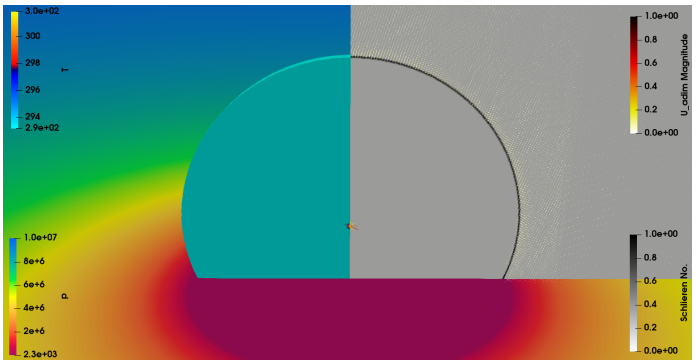

(a) t/τ_0 =0

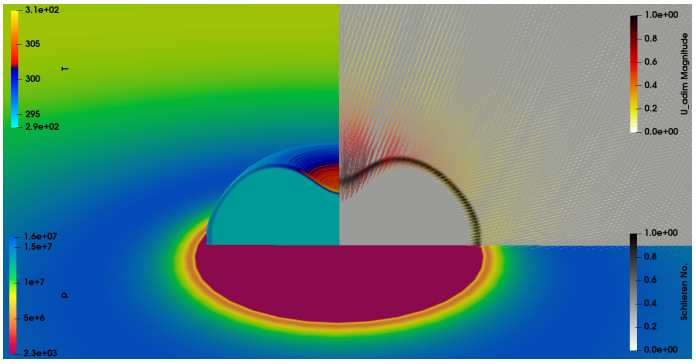

(b) t/τ_0 =1.02

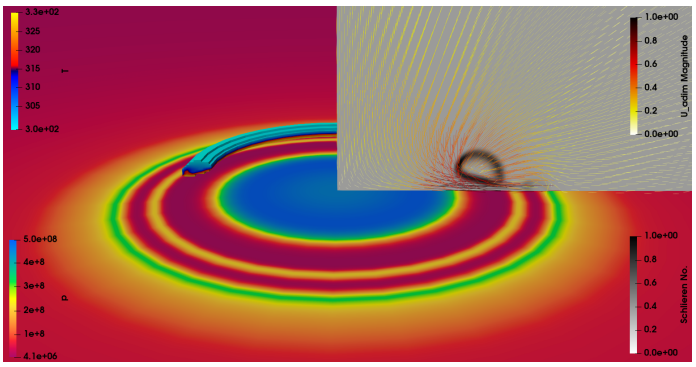

(c) t/τ_0 =1.08

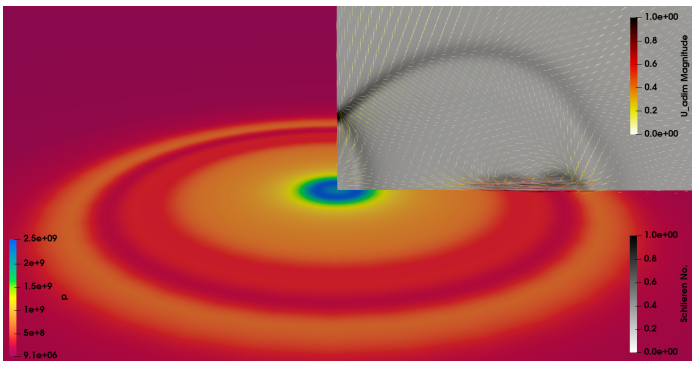

(d) t/τ_0 =1.09

Figure 4.11: Pressure, Temperature, and Schlieren images for bubble at $SOD/R_0 =$ 0.35 at three different time steps: (a) t/τ_0 =0, (b)) t/τ_0 =1.02, (c)) t/τ_0 =1.08, and (d)) t/τ_0 =1.09.

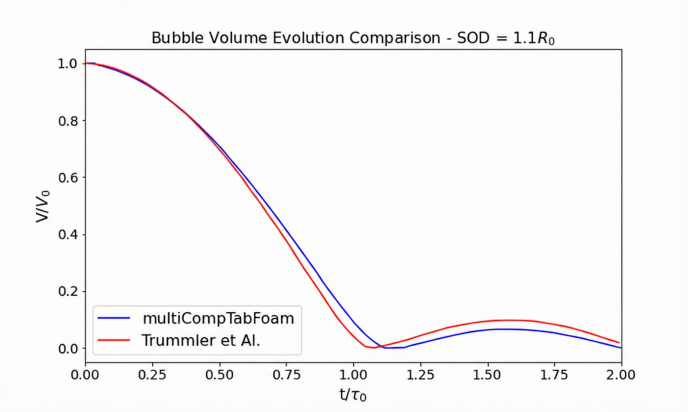

(a)

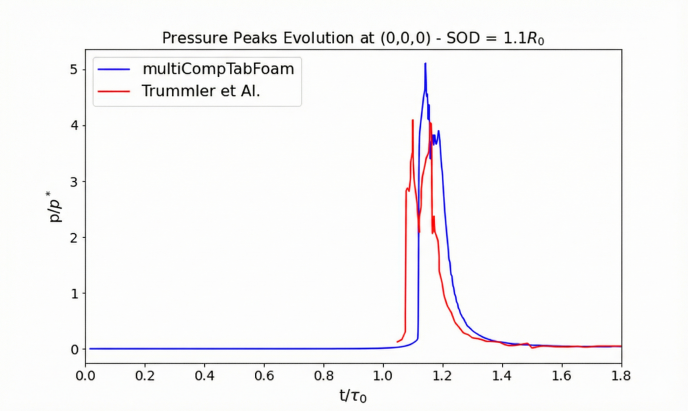

(b)

Figure 4.12: (a) Bubble volume evolution and (b) pressure evolution for $SOD = 1.1R_0$.

Overall, once again, the results obtained with `multiCompTabFoam` are in agreement with Trummler et al. results [Trummler et al., 2021], as shown in Fig. 4.12.

The small differences between `multiCompTabFoam` and the results from Trummler can be attributed mainly to the thermodynamic closure. Indeed, cubic equations of state are well known for overpredicting the density when dealing with mixtures at critical or transcritical conditions compared to Real-Fluid Thermodynamics, such as PC-SAFT employed in this Thesis.

A final important remark concerns the time to collapse in these different configurations. To explain why, if $SOD \leq 0$, the collapse occurs before the expected time for an isolated bubble (i.e., $t_{collapse} < \tau$), it can be noted that most of the bubble (if not all) is subjected to the flow pressure. Consequently, the force acting on the bubble is higher. Indeed, observing Fig. 4.6b and Fig.

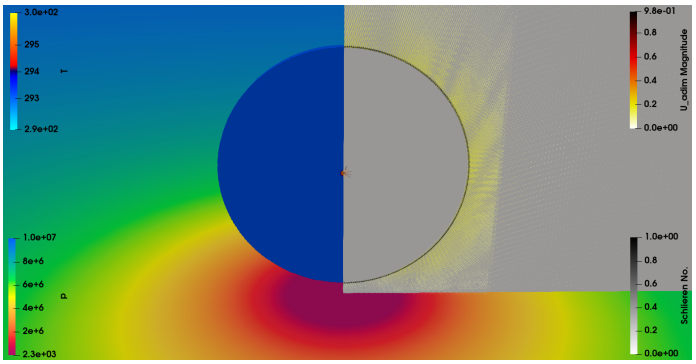

(a) t/τ_0 =0

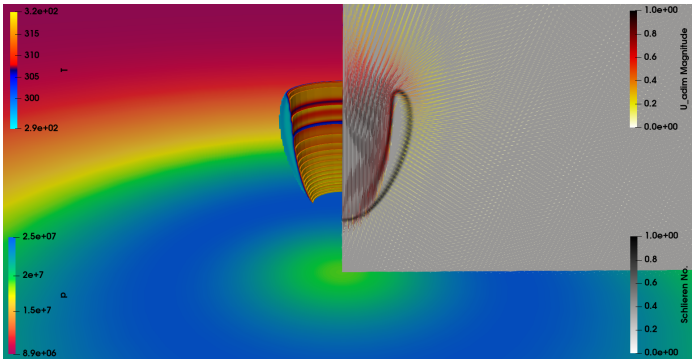

(b) t/τ_0 =1.11

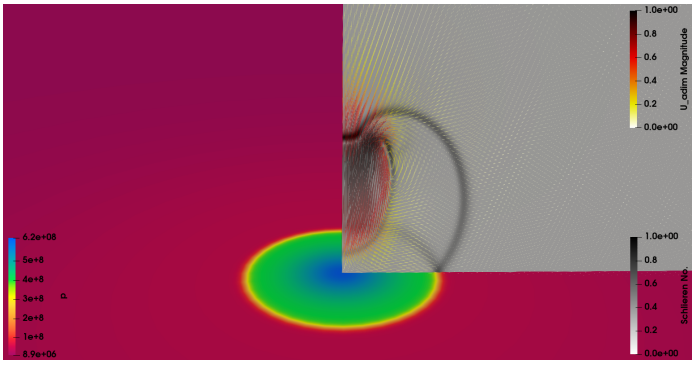

(c) t/τ_0 =1.13

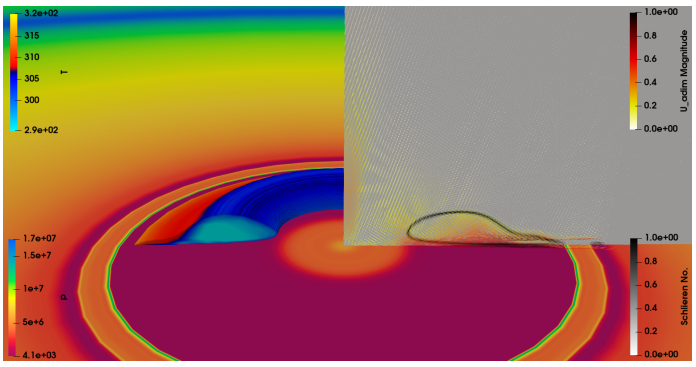

(d) t/τ_0 =1.67

Figure 4.13: Pressure, Temperature, and Schlieren images for bubble at SOD/R_0 = 1.1 at three different time steps: (a) t/τ_0 =0, (b)) t/τ_0 =1.11, (c)) t/τ_0 =1.13, and (d)) t/τ_0 =1.67.

4.8b, the pressure peaks are higher compared to the other cases. As a result, a higher cavitation-induced risk might be expected in these configurations.

4.3.5 Mesh Independence Study for a Single Bubble Collapsing Near a Solid Surface

To conclude this section, a mesh resolution study on a bubble collapsing near a solid surface was also performed, following, again, the work of Trummler et al. [Trummler et al., 2021]. We have performed simulations of collapsing bubbles at different stand-off distances with grid resolutions from 20 to 240 cells/R_0. As one would expect, the peak pressures in the domain and at the wall are affected by the grid resolution. Indeed, Fig. 4.14 shows the maximum wall pressure $p_{max,wall}$ for different grid resolutions and stand-off distances S/R_0. At all configurations, the maximum pressure was recorded in the center. With an increasing absolute stand-off distance $|S/R_0|$, $p_{max,wall}$ decreases. This matches experimental and numerical investigations from the literature [Lauterborn and Ohl, 1998] [Brennen, 2013] [Plesset and Chapman, 1970].

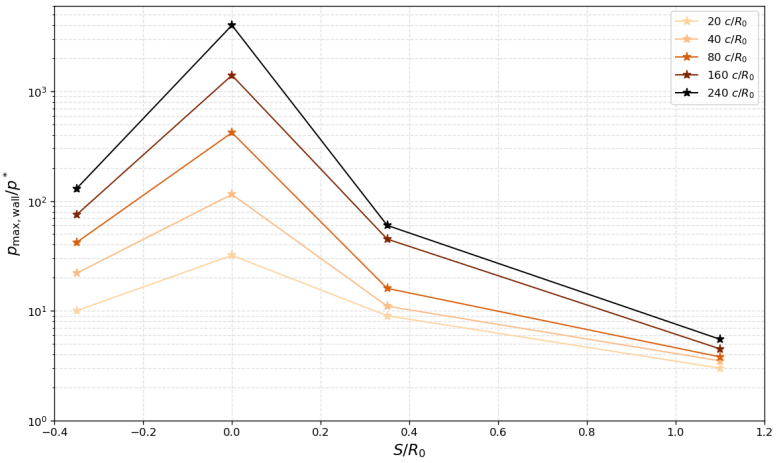

Figure 4.14: Maximum pressure recorded at the wall $p_{max,wall}/p^*$ for varying stand-off distances $|S/R_0|$ and different grid resolutions.

For wall- attached bubbles, the increase in $p_{max,wall}$ is approximately inversely proportional to the cell length, whereas for wall-detached bubbles $p_{max,wall}$ is less grid dependent. Overall, the relative ratio of pressure peaks is comparable at identical grid resolutions and, consequently, the data obtained

at a certain grid resolution allows for a comparative and qualitative assessment of the cavitation erosion potential.

In summary, the most important collapse features are already captured at the coarsest grid resolution of 20 $cells/R_0$. The main features of the maximum pressure distribution, such as pronounced pressure peaks at toroidal collapses, are mostly resolved for $N * cells/R_0 \geq 160$ and at higher resolutions, mainly the intensity of the peaks changes. For the peak values, we observe that the values induced by a collision of accelerated liquid fronts or a collapse are approximately inversely proportional to the cell length, as also found by Mihatsch et al. [Mihatsch, 2016]. For the rebound and the second collapse we find a strong grid dependence, but a convergence of the rebound vol- ume for high grid resolutions.

Finally, in agreement with the literature [Mihatsch, 2016] [Schmidt et al., 1999], we found that peak values induced by a collision of accelerated liquid fronts scale approximately inversely proportional to the cell length. However, since we are using a diffusive methodology, we know that the real maximum pressure will not be captured unless the mesh is infinitely refined, which is not possible [Trummler et al., 2021] [Schmidt et al., 2008]. However, the goal of this thesis, and CFD in general, is not to find the exact value, but to predict certain phenomena most accurately and correctly.

4.4 Cluster of Bubbles

In this section, the collapse of a cluster of bubbles over a flat wall is presented.[3] In particular, the focus will be on bubble dynamics influenced by the collapse of surrounding bubbles as well as the proximity to the wall.

Two different studies are presented:

- A comparative study of a water-based cloud of bubbles near a wall

[3]A significant portion of this chapter is published as: R. Bellini, C. Rodriguez, I. K. Karathanassis, M. Gavaises, "Cavitation Dynamics and Surface Erosion in Fuel Injectors, Considering the Composition of Fuel Mixtures", Computer and Fluids, 2025 under the terms of the Creative Commons Attribution 4.0 license (CC BY 4.0). The author of this dissertation contributed to the methodology, validation, data curation, formal analysis, investigation, writing, and visualisation of the article.

against previous studies by Schmidt [Schmidt et al., 2008] and Ghahramani [Ghahramani et al., 2019].

- Cluster of bubbles simulations for three different fuels assess how the properties of renewable and non-renewable fuels affect the pressure peaks.

4.4.1 Mesh Independence Study for a Cluster of Bubble Collapsing Close to a Solid Surface

Similarly to what has been discussed in Section 4.3.5, this section focuses on how the mesh resolution affects the simulation results of a cluster of bubbles collapsing close to a solid surface. In this study, we considered different ways to discretise the smaller cube domain (i.e. the domain in which the bubbles are contained, see Fig. 4.19). The coarser mesh used 7 cells per side, then doubling the cells per side up to 440 cells per side.

The first parameter that was taken into account for this study was the time evolution of the dimensionless equivalent radius for the different spatial resolutions. From the start of the simulation until the first collapse all grids show a similar behaviour, In particular, we can observe in Fig. 4.15 that the mesh resolution affects the time to collapse, showing that coarser meshes tend to overestimate the time to collapse. At the same time, there is almost a convergence above 220 cells.

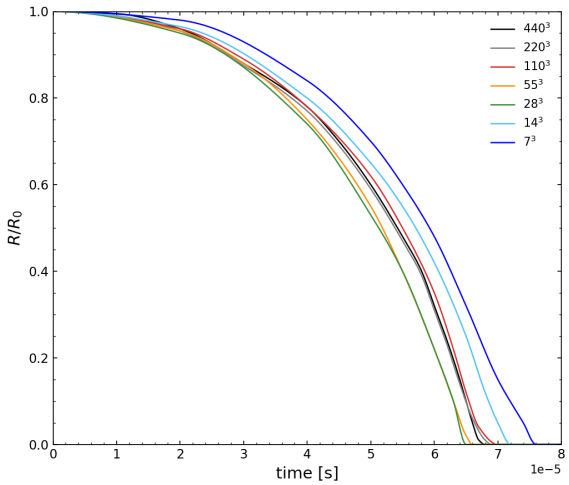

Figure 4.15: Time evolution of dimensionless equivalent radius with different mesh resolutions.

The next parameter under consideration was the maximum pressure in the flow field and at the wall sensor. The maximum values of the pressure in the flow field are shown in Fig. 4.16, which shows that the maximum pressure varies by about two orders of magnitude depending on the mesh resolution. In particular, it scales with the inverse of the characteristic cell size. On the other hand, the maximum pressures on the sensor only show a comparatively weak variation by a factor of ≈ 2.5.

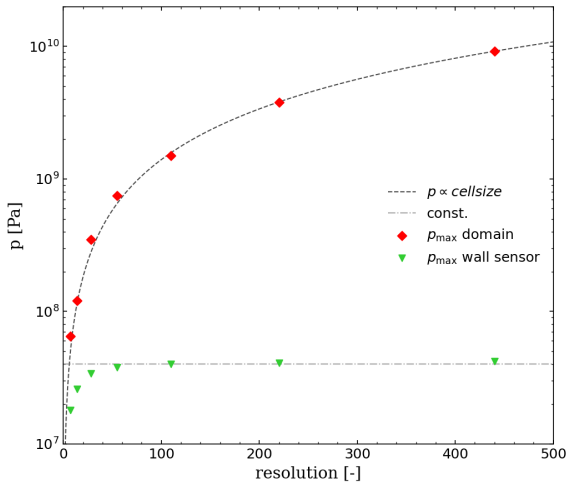

Figure 4.16: Grid-dependence of the maximum pressure in the field and at the wall sensor.

As already mentioned in Section 4.3.5, we found that peak values induced by a collision of accelerated liquid fronts scale approximately inversely proportional to the cell length. However, since we are using a diffusive methodology, the real maximum pressure will not be captured unless the mesh is infinitely refined [Mihatsch, 2016].

Finally, we analyse the influence of grid resolution on the impact of the pressure wave on the wall. Fig. 4.17 shows time signals as obtained by the wall sensor. In the reference configuration, the impact is represented as a sharp peak with a duration of approximately $5 * 10^{-6} s$. Comparison with the sensor output acquired on the grid using 220 cells per side and 440 cells per side shows that this solution is grid converged. With the lowest resolution, grid using 7 cells per side, the peak has a lower amplitude and is smeared.

Therefore, a grid of 220 cells per side within the small domain was used for

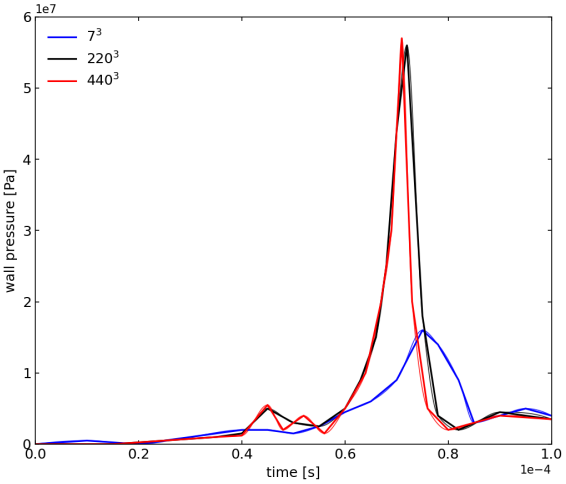

Figure 4.17: Time evolution of the pressure on the wall sensor for 3 selected grid resolutions.

results production.

4.4.2 Collapse Dynamics of a Cloud of Water Vapour Bubbles

In the first study, a vapour bubble cloud, previously defined by Schmidt [Schmidt et al., 2008] and later by Ghahramani [Ghahramani et al., 2019], is considered. This cloud consists of 125 spherical vapour bubbles with radii ranging from 0.70 mm to 1.64 mm, distributed non-uniformly. The average bubble radius is 0.95 mm, and a minimum centre-to-centre distance of 0.2 mm is imposed to prevent intersection. Moreover, the bubbles are more concentrated and larger in the centre of the cloud. The entire cloud is placed inside a small, liquid-filled cubic domain of $20 \times 20 \times 20\,\mathrm{mm}^3$, with a total vapour volume fraction of 5.8%. This cubic domain is embedded within a larger rectangular domain of $4 \times 4 \times 2\,\mathrm{m}^3$, with the bottom faces of the two domains being co-planar, as illustrated in Fig. 4.18.

The structured grid employed for domain discretisation (Fig. 4.18) contains approximately 22 million cells, of which around 11 million are located within the small cubic domain of $20 \times 20 \times 20\,\mathrm{mm}^3$ (i.e. each side of the small cubic domain was discretized with 220 cells). Depending on bubble size, between 128 and more than 600 cells were used to discretise the bubble volume, corre-

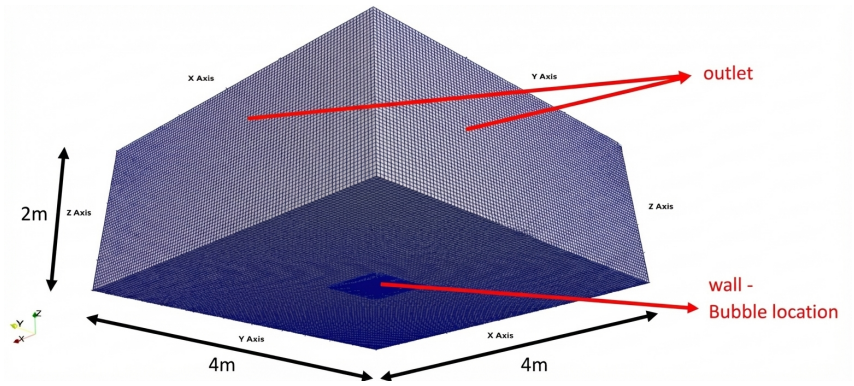

Figure 4.18: 3D mesh employed for the cases referring to a cluster of bubbles. Dimensions are $4 \times 4 \times 2\,\mathrm{m}^3$

sponding approximately to a resolution of $0.051 < \Delta/r < 0.021$, where Δ is the cell size and r is the bubble diameter.

The bubble distribution inside the inner domain is depicted in Fig. 4.19.

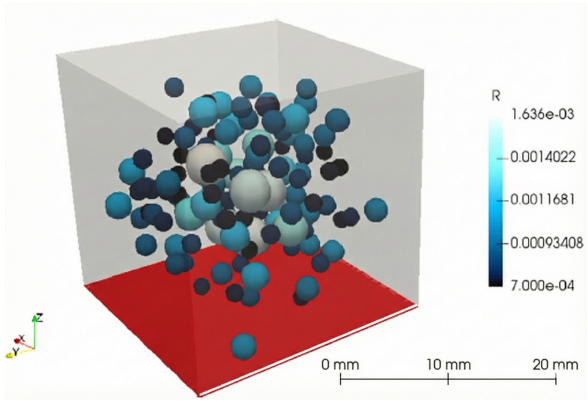

Figure 4.19: Representation and distribution of 125 spherical non-intersecting bubbles within the small cubic domain over a flat wall (red surface)[Ghahramani et al., 2019]. Cube dimensions are $20 \times 20 \times 20\,\mathrm{mm}^3$.

The fluid domain (water) is assumed to have stationary initial conditions with a uniform temperature of 293 K. The initial pressure inside the bubbles is set equal to the vapour pressure of 2340 Pa, while the surrounding liquid is assumed to follow a Laplacian distribution (as in Eq. 4.1 for the single-bubble cases), which is reasonable for a stationary condition. The co-planar bottom faces of the domain are defined as impermeable walls, while the other outer faces are treated as far-field boundaries with a constant pressure of 40 bar and zero gradient for the remaining flow parameters. Finally, to measure the pressure imposed by the collapsing bubbles on the bottom wall, a pressure transducer is located at the centre of the bottom face. This transducer covers

an area of 1 cm^2 and samples the average pressure over this area at every time step. As no experimental data or analytical solution exists for this specific bubble cloud with the given boundary conditions, validation of the case has been carried out against the results published by Schmidt [Schmidt et al., 2008] and subsequently by Ghahramani [Ghahramani et al., 2019].

In particular, Gharamani et al. [Ghahramani et al., 2019] implemented an Eulerian–Lagrangian cavitation model, which couples an Eulerian finite mass transfer formulation with a bubble-tracking Lagrangian framework. The thermophysical properties of the vapour–liquid mixture were evaluated using a volume fraction methodology. Thermodynamic closure was established by applying the ideal gas law for the pure vapour phase and the modified Tait EoS for the liquid phase.

Conversely, Schmidt et al. [Schmidt et al., 2008] employed their in-house code CATUM, whose numerical formulation bears strong resemblance to the approach adopted in the present work, albeit with thermodynamic closure provided through a barotropic EoS.

As shown in Fig. 4.20, the collapse time of the numerical cloud is 7.3×10^{-5} s in the simulation of Ghahramani et al., 6.3×10^{-5} s in the work of Schmidt et al., and 6.9×10^{-5} s in the present study. Overall, the estimated collapse times show good agreement across the different modelling approaches. Discrepancies may arise from differences in the thermodynamic closure methods or from minor variations in the pressure field used for simulation initialisation. Nonetheless, the profiles of both volume variation and wall pressure appear very similar. Differences are also noticeable in the pressure peaks recorded by the wall probe, as shown in Fig. 4.20b. These discrepancies can likely be attributed to the different flux schemes employed, since in compressible flows, flux schemes handle shocks, rarefactions, and contact discontinuities differently. For instance, HLLC schemes, used in this work, better resolve contact discontinuities and reduce dissipation at shocks, leading to more accurate pressure and temperature predictions in regions of high gradients. In any case, reasonable agreement can be claimed, as all pressure peaks remain of the same order of magnitude [Schmidt et al., 2008].

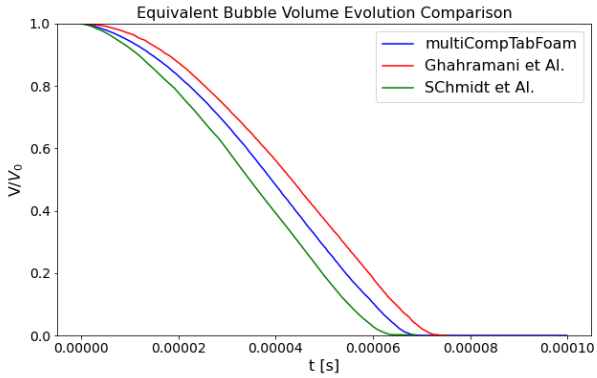

(a)

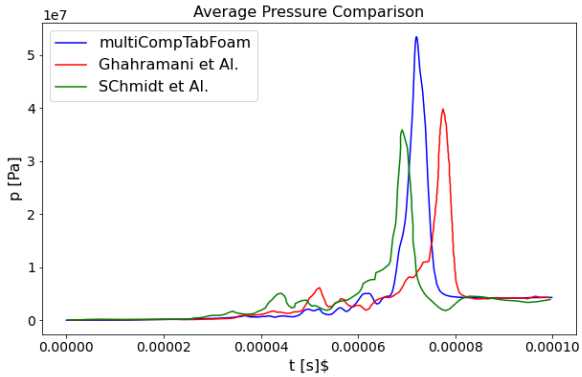

(b)

Figure 4.20: Validation of `multiCompTabFoam`'s simulation of bubble cluster against published data; (a) time history of the vapour volume; (b) average pressure on the wall transducer.

Finally, Fig. 4.21 shows the bubble cloud topology, illustrated through iso-surfaces of volume fraction equal to 0.5, and the wall pressure through contour plots at different time instances; these visualisations provide an overview of the time evolution of the bubble cluster collapse. Fig. 4.21a shows the initial conditions for the pressure field and the initial position and configuration of the bubbles. Fig. 4.21b illustrates the cloud collapse at $t = 3.491 \times 10^{-5}$ s; it can be observed that the bubbles located at the periphery of the cloud start collapsing first. Fig. 4.21b also shows the re-entrant jets that start forming in the peripheral bubbles. Moreover, vapour formation among bubbles is clearly visible. Fig. 4.21c corresponds to a time step where the peripheral bubbles have collapsed while the collapse sequence of those located at the centre of the cloud has commenced. Re-entrant jets are impinging on the wall below the cluster, as indicated by the high-pressure values in the wall contour plots.

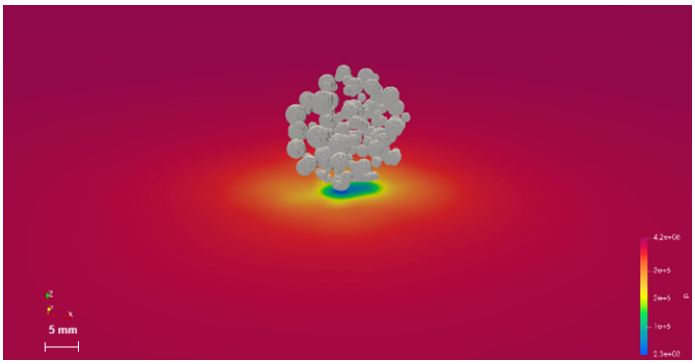

(a) t = 0s

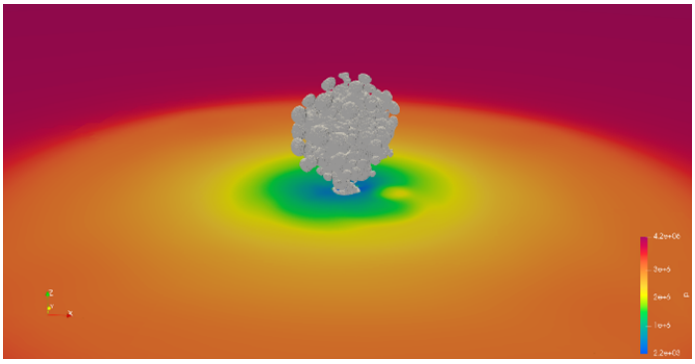

(b) t = 3.491e-5 s

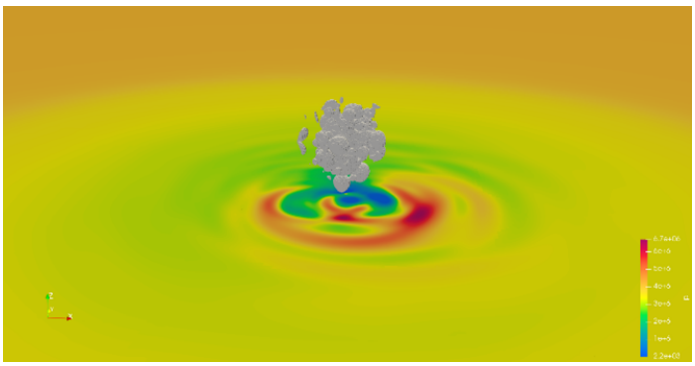

(c) t = 5.258e-5 s

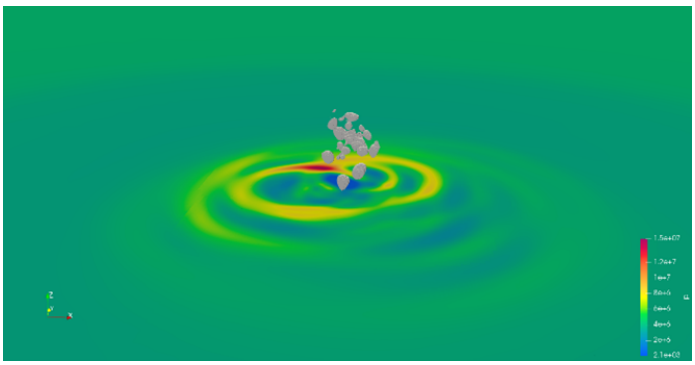

(d) t = 6.3914e-5 s

Figure 4.21: Bubble cloud topology (i.e., iso-surfaces of volume fraction equal 0.5) and wall pressure contours at different time instances of the simulation: (a) t = 0s, (b) t = 3.491e-5 s, (c) t = 5.258e-5 s, and (d) t = 6.3914e-5 s.

Finally, Fig. 4.21d corresponds to a time instance at the latest stage of the collapse, where all remaining vapour structures are close to collapse and already pierced by the re-entrant jets. Figs. 4.21c and 4.21d are important as they show how pressure propagates and highlight the pressure peak zones caused by cavitating bubbles, demonstrating how the pressure immediately propagates in the surrounding regions. It should be noted that rarefaction waves are not prevalent in geometrical layouts such as the one considered in the present study, as the flow field is not symmetrically wall-bounded.

4.4.3 Comparison of diesel and short-Chain alcohols bubble collapse under the same DFICE Conditions

The test case presented in the following section goes beyond code validation and is relevant to the incorporation of different fuels in DFICE. Simulations of bubble clusters for three different fuels have been performed, revealing the effect of fuel properties on the pressure peaks occurring during the collapse of the cloud.[4]

The short-chain alcohols considered in this report are methanol and ethanol, based on the work of Aleiferis et al. [Aleiferis et al., 2010]. Following the test case performed by Obloblina et al. [Ogloblina et al., 2018], the cloud consists of 150 spherical vapour bubbles with a constant radius of 1.5×10^{-3} m, and the minimum distance between bubbles is 0.2×10^{-3} m to avoid intersection. The bubbles are also more concentrated around the centre of the cloud. The overall cloud is located in a small liquid-filled spherical domain of radius 15×10^{-3} m, with a stand-off distance from the wall of 3.2×10^{-3} m, and has a total volume fraction of 8%.

The geometry and mesh discretisation remain the same as for the previous case studied and are shown in Fig. 4.18. Similar to the previous case, a virtual

[4]A significant portion of this chapter is published as: R. Bellini, C. Rodriguez, I. K. Karathanassis, M. Gavaises, "Cavitation Dynamics and Surface Erosion in Fuel Injectors, Considering the Composition of Fuel Mixtures", *Computers & Fluids*, 2025, under the terms of the Creative Commons Attribution 4.0 license (CC BY 4.0). The author of this dissertation has contributed to the methodology, validation, data curation, formal analysis, investigation, writing, and visualisation of the article.

probe has been placed on the wall below the bubble cluster to record maximum pressure and temperature values at each time step. The numerical set-up is common to all fuels examined. Tab. 4.4 summarises the conditions referring to the far-field flow, whilst Tab. 4.5 outlines those relevant to the cluster of bubbles. The far field has been initialised with a pressure and temperature of 10 MPa and 350 K, respectively, while the bubbles have been initialised at 350K under their vapour-saturation conditions.

From Tab. 4.4, it is evident that, under the same conditions, dodecane has a lower density, while the values in Tab. 4.5 demonstrate that dodecane (at saturation conditions) has a significantly lower vapour pressure compared to methanol and ethanol, suggesting a lower tendency to cavitate.

Fuel	ρ $[kg/m^3]$	e $[J/kg]$
Dodecane	714	-378040.1
Ethanol	749.5	403889.3
Methanol	748.2	29389.2

Table 4.4: Far-field initial conditions for Dodecane, Methanol and Ethanol at 350 K and 10 MPa.

Fuel	ρ $[kg/m^3]$	e $[J/kg]$	p [Pa]
Dodecane	2.6	-369052.8	614.27
Ethanol	2.9	831458	95220.64
Methanol	1.45	1042157.2	125889.8

Table 4.5: Cluster-of-bubbles' initial conditions for dodecane, Methanol and Ethanol at 350 K.

As there is no experimental data or analytical solution for this specific cloud under the specified boundary conditions and for these particular fuels, the results are compared only among themselves, and some comments on the influence of fuel properties on cavitation are provided.

Initially, the evolution of the equivalent bubble-cluster radius for the examined fuels is compared in Fig. 4.22. The equivalent radius has been calculated by summing the volumes of all 150 bubbles and defining a single bubble with the same total volume, thereby obtaining an equivalent bubble radius. It is evident that fuel properties do not significantly influence the collapse time of

the bubble cluster. The dodecane bubble collapses approximately 10^{-6} s earlier compared to the bubble clusters of alcohols, as shown in Fig. 4.22. This is attributed to the lower initial pressure of the dodecane bubble cluster, i.e., the vapour pressure as given in Tab. 4.5. However, this is not the most representative difference among the three fuels, as the discrepancy is minimal and can be explained by the small variation in density for both their liquid and vapour phases.

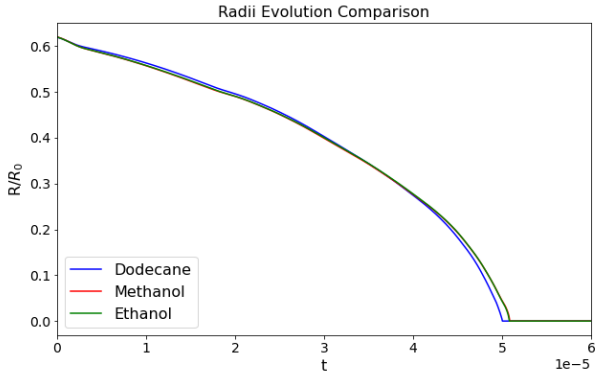

Figure 4.22: Radii evolution comparison among dodecane, methanol, and ethanol.

At the same time, the average pressure (Fig. 4.23a) and temperature (Fig. 4.23b) for dodecane are higher compared to those for methanol and ethanol. These behaviours may be attributed to different mechanisms of the heating effects in the three fuels.

Indeed, focusing on Tab. 4.6, 4.7, 4.8, and 4.9, methanol has the largest latent heat (Tab. 4.6). Therefore, during condensation, the temperature of methanol liquid will increase more. In addition, methanol exhibits the strongest compression heating compared to the other fuels, as shown in Tabs. 4.7, 4.8, and 4.9.

Fuel	T	p	ρ_L	ρ_V	h_L	h_V	ΔH_V
Dodecane	350	6.167e-4	707.26	3.615e-2	-373.23	-40.466	332.76
Ethanol	350	9.591e-2	737.85	1.563	409.94	1262.2	852.29
Methanol	350	1.617e-1	735.84	1.9053	35.664	1111.6	1076.0

Table 4.6: Main thermodynamic properties at saturation conditions of the three fuels taken from NIST Refprop Database[*NIST Refprop Database*, 2022]

From Figs. 4.24a and 4.25a, it can be observed that dodecane exhibits a

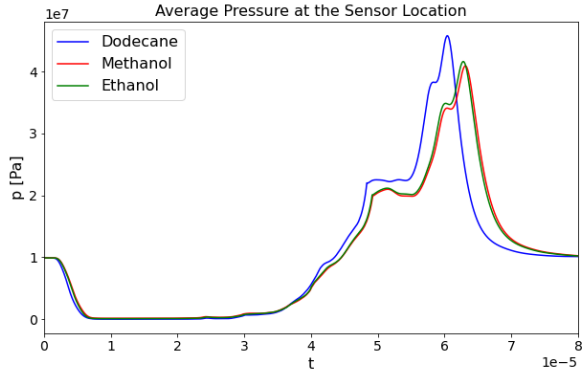

(a)

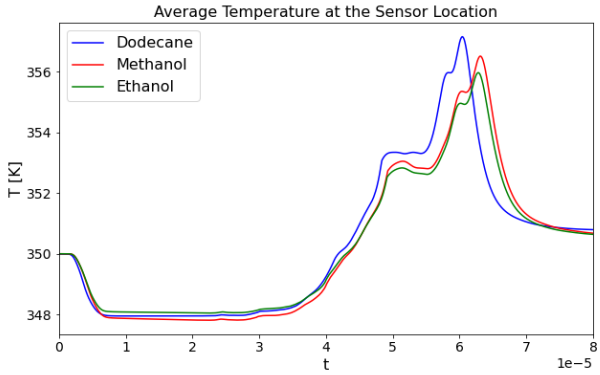

(b)

Figure 4.23: Average (a) pressure and (b) Temperature over the sensor below the cluster of bubbles for dodecane, methanol, and ethanol.

T	p	ρ	h	s	c_p	c_v
350	0.1	707.36	-373.14	-0.89202	2.0129	2.3970
352.06	10.0	715.28	-359.22	-0.89202	2.0256	2.3935
365.78	100.0	764.47	-273.93	-0.89202	2.1240	2.4185

Table 4.7: Main Thermodynamics properties at specific state points for dodecane, taken from NIST Refprop Database[*NIST Refprop Database*, 2022].

T	p	ρ	h	s	c_p	c_v
350	0.1	737.85	409.95	1.6722	2.6542	3.1707
352.06	10.0	747.83	423.27	1.6722	2.6553	3.1282
365.78	100.0	807.73	538.57	1.6722	2.6676	3.0665

Table 4.8: Main Thermodynamics properties at specific state points for Ethanol, taken from NIST Refprop Database[*NIST Refprop Database*, 2022].

stronger collapse, i.e., higher pressure peaks, owing to a greater level of condensation compared to the other fuels. A higher level of condensation indicates that the surrounding vapour is rapidly transitioning back to the liquid phase

T	p	ρ	h	s	c_p	c_v
350	0.1	1.1359	1139.4	3.3761	1.8216	2.2525
352.06	10.0	68.5	1700	3.3761	2.5511	2.9976
365.78	100.0	412.98	2097.8	3.3761	3.3316	3.9594

Table 4.9: Main Thermodynamics properties at specific state points for Methanol, taken from NIST Refprop Database[*NIST Refprop Database*, 2022].

as the bubble implodes, leading to a more forceful implosion and the generation of higher pressure peaks. Moreover, the dodecane bubble cluster collapses slightly faster than the methanol and ethanol clusters, as it has a lower density under the same conditions; this results in higher pressures (Figs. 4.24a and 4.25a) due to the more violent and rapid collapse. Therefore, short-chain alcohols exhibit a more favourable behaviour compared to dodecane in terms of cavitation collapse and cavitation-induced erosion, making them sustainable fuels suitable for incorporation in DFICE.

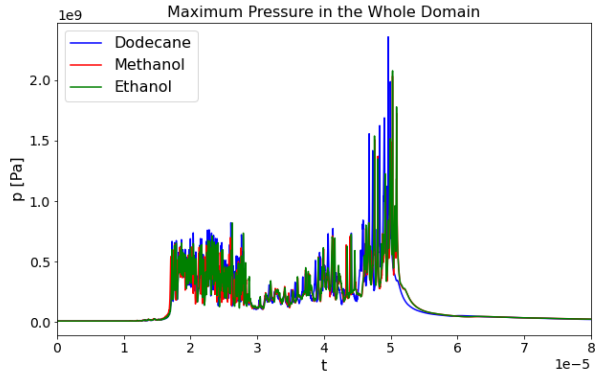

(a)

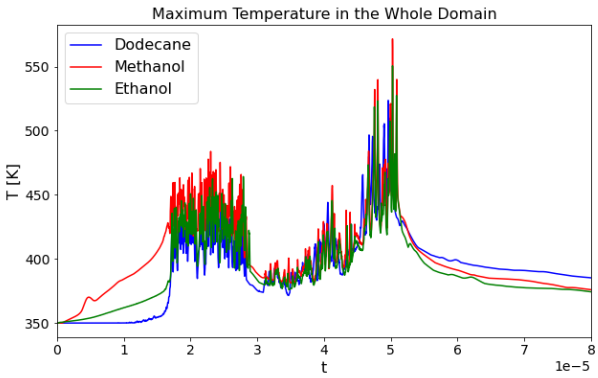

(b)

Figure 4.24: Maximum (a) pressure and (b) Temperature in the whole domain for Dodecane, Methanol, and Ethanol.

Moreover, it can be noted that, at the initial conditions (350 K and 10 MPa), methanol has the largest latent heat (1,070 J/kg) compared to ethanol (852.3 J/kg) and dodecane (332.8 J/kg). During collapse, methanol exhibits the strongest compression heating among the three fluids, as demonstrated in Figs. 4.24b and 4.25a, and therefore reaches higher temperatures both throughout the domain (Fig. 4.24b) and at the probe wall (Fig. 4.25b). This could lead to performance and reliability issues when cavitation occurs inside the orifices of a DFICE injector, potentially affecting combustion quality.

The temperature increase of methanol as pressure rises under constant entropy is greater compared to the other fuels, as also confirmed by the simulations (Fig. 4.24). As expected, ethanol shows maximum pressures and temperatures that lie between those of dodecane and methanol, which can be explained by its latent heat and internal energy relative to the other fuels under examination. Following the same rationale, it is evident from Tabs. 4.4 and 4.5 that dodecane has the lowest heat of vapourisation and density at saturation conditions; accordingly, the simulation trends show that, even when achieving higher pressure peaks, dodecane exhibits less heating and lower peak temperatures.

4.4.4 Limitations and Critical Review

In this chapter, the main goal was to demonstrate the capability of the new solver to simulate a single bubble collapsing both far from a wall and close to a wall with different stand-off distances, as well as to capture the behaviour of a collapsing cluster of bubbles. All results have been compared and validated against analytical, experimental, or numerical data, showing satisfactory agreement.

The main limitation of this section is the lack of consistent data for comparison, particularly well-established experimental databases. This is due to the limited replicability of experiments assessing the cavitation of a single bubble or a cluster of bubbles. In other words, collecting meaningful statistical data is challenging because of the highly explosive behaviour of the phenomenon

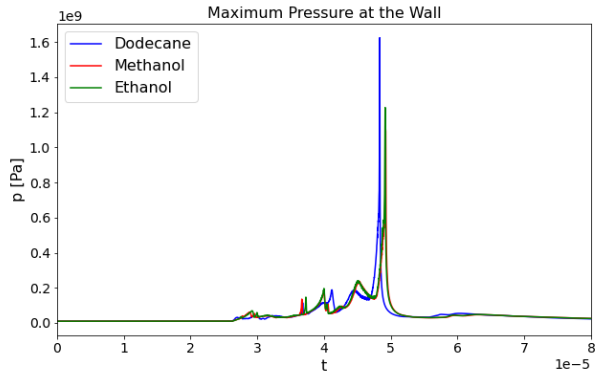

(a)

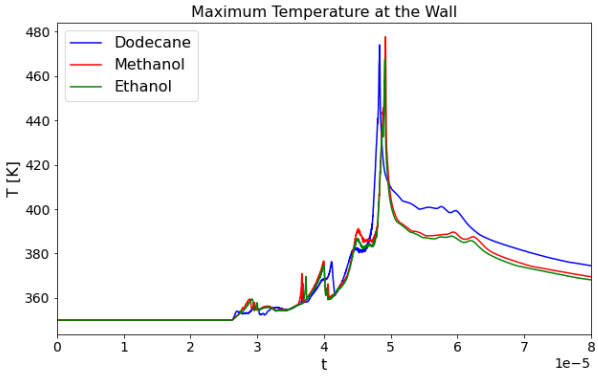

(b)

Figure 4.25: Maximum (a) pressure and (b) Temperature at the wall for dodecane, methanol, and ethanol.

and its sensitivity to small perturbations.

Recent publications, such as [Deng et al., 2024], employing direct numerical simulations, studied single gas/vapour bubbles and spherical bubble clusters containing 13–352 vapour bubbles in compressible flow fields. The numerical results indicate that the single cavitation bubble retains its spherical shape during collapse, and the far-field acoustic pressure calculated using the Ffowcs-Williams–Hawkings (FWH) formulation is consistent with the analytical solution obtained from the volume acceleration calculation, which aligns with the results presented in this chapter. However, the spherical bubble cluster collapses layer by layer (i.e., starting from the outermost bubbles and moving radially towards the centre) due to strong coupling between the bubbles. The closer to the centre of the bubble cluster, the shorter the collapse time and the greater the non-spherical deformation.

The collapse of a bubble cluster generates multiple acoustic pressure peaks, which cannot be accurately predicted by the volume fluctuation sound source theory. The size and volume fraction of the bubble cluster significantly influence the collapse time and the distribution of sound pressure. When the volume fraction of a bubble cluster is large, the total collapse time is almost the same as that of a single bubble with the same total volume, and the frequency distribution of sound pressure of a dense cluster is also similar to that of the corresponding single bubble. Furthermore, a bubble cluster with randomly distributed bubble diameters collapses asymmetrically and rebounds in the later stages of the collapse process.

As an improvement to the present work, it would be valuable to develop a post-processing system capable of capturing multiple acoustic pressure peaks, to better understand cavitation phenomena and the rebounding collapses occurring in clusters close to a wall. Finally, this could lead to the development of a probabilistic distribution or law able to define, in a generalised way, the pressure peaks based on different initial conditions.

Chapter 5

Spray and Atomisation Test Cases

In this chapter, we illustrate the performance of multiCompTabFoam in analysing in-nozzle simulations and examine how cavitation affects spray evolution in four different cases.[1]

Benchmark case	Numerical prediction or experimental data
Case A - Spray C in-nozzle Flow	X-ray phase-contrast radiographies [Tekawade et al., 2020]
Case B - Spray C in-nozzle Flow	x-ray radiography measurements [Guo, 2020]
Case C - Spray C near-nozzle spray region	CONVERGE simulations [Sforzo, 2019]
Case D - Spray C Cone angle	ECN Data [Sandia, 2023]

Table 5.1: Benchmark cases relevant to injector flows were employed to validate the numerical methodology implemented in the present study.

Case *A* is designed to assess the accuracy of the developed CFD code by comparing it with experimental findings for the in-nozzle flow of the ECN Spray C injector [Tekawade et al., 2020]. Case *B* aims to benchmark the accuracy of

[1]A significant portion of this chapter is published as: R. Bellini, C. Rodriguez, I. K. Karathanassis, M. Gavaises, "Modelling of wall-bounded cavitating flow and spray mixing in multi-component environments using the PC-SAFT equation of state", *Applications in Energy and Combustion Science*, 2025, under the terms of the Creative Commons Attribution 4.0 license (CC BY 4.0). The author of this dissertation has contributed to the methodology, validation, data curation, formal analysis, investigation, writing, and visualisation of the article.

the algorithm against widely used commercial software, emphasising in-nozzle cavitating flows [Guo, 2020]. Case *C* is set up to examine the accuracy of the proposed numerical framework, illustrating the effect of nozzle geometry on the near-nozzle spray cone angle for the ECN Spray C injector [Tekawade et al., 2020][*Sandia National Laboratories - Spray A*, 2024]. Finally, Case *D* is devised as a comparative study focusing on the cone angle of the ECN Spray C.

Tab. 5.1 summarises the test cases performed against experimental results to validate the numerical approach proposed in the present study, along with the numerical and thermodynamic approaches against which our methodology has been compared in each case, as well as the sources of the available experimental data.

5.1 Geometry and Numerical Grids

The developed numerical framework was validated using the Spray C037 injector nozzle, a well-studied component within the Engine Combustion Network (ECN). Spray C037 injector nozzle was specifically designed to be the benchmark for studying internal nozzle cavitation. The Spray C nozzle has a sharp-edged inlet inside the injector, and, as fuel flows around this sharp corner at high velocity, the pressure drops drastically. If it drops below the fuel's vapor pressure, vapor bubbles form (cavitation) [Sandia, 2023]. It is worth noting that the precise geometry of this nozzle has been accurately measured as part of the ECN's extensive research initiatives. For a comprehensive understanding of the Spray C037 injector nozzle geometry, readers are referred to the resources available on the official ECN website [Sandia, 2023]. The computational domain, as depicted in Fig. 5.1a, comprises a rectangular region connected to the fuel injector, with overall dimensions of $32 \times 105\,\text{mm}$.

To streamline the process of mesh generation, an adaptive mesh refinement technique was employed. A Cartesian blocking strategy was followed, combined with a static local coarsening/refinement approach, and the grid resolution was adjusted along the spray break-up trajectory to enhance com-

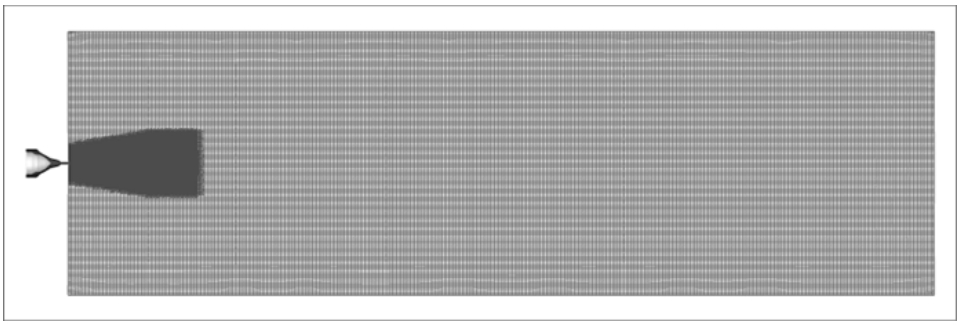

(a) Overall domain.

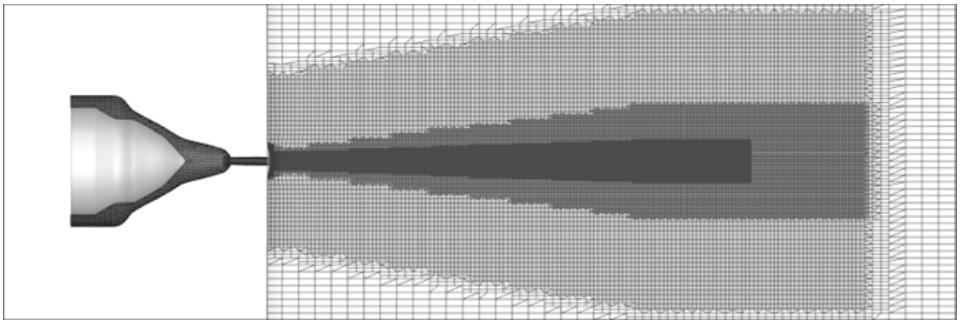

(b) Detailed view of the near-nozzle region mesh.

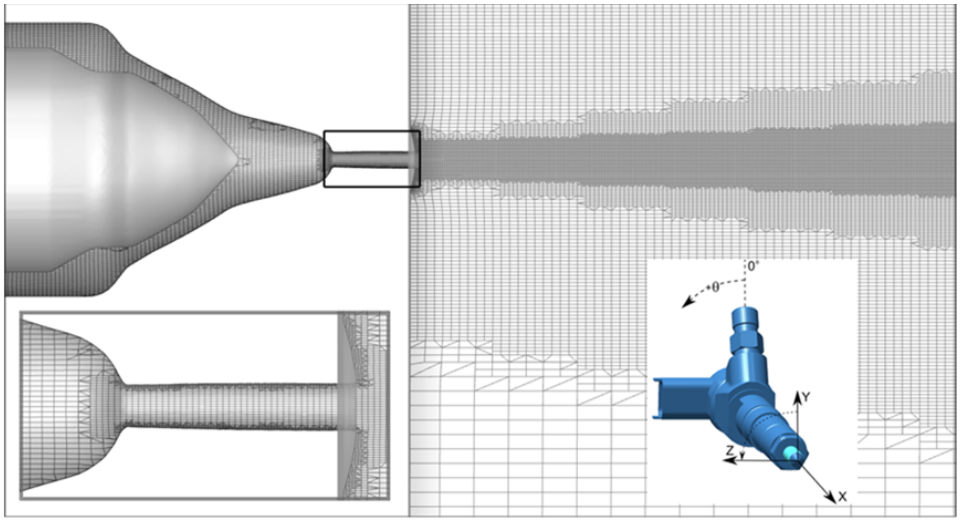

(c) Close-up of the in-nozzle region mesh

Figure 5.1: Numerical grid for the Spray C037 injector nozzle: (a) overall domain, (b) detailed view of the near-nozzle region, (c) close-up of the in-nozzle region, and the ECN coordinate system for the Spray C injector. [Sforzo, 2019].

putational efficiency. In the core of the orifice, the resolution is approximately 10 µm, with refinement closer to the walls reaching a minimum cell size of around 2 µm. This resolution is consistent with the viscous length scales, represented by the equation $\lambda_g = \sqrt{10} Re^{0.5} D$, where D is an indicative length of the geometry; in this case, the nozzle hole exit diameter [Rodriguez et al., 2021].

The flow near the wall is addressed using two specific wall functions: (i) the `kqRWallFunction` [Liu, 2016] for managing the turbulent kinetic energy, and (ii) the `nutkWallFunction` [Liu, 2016] for handling the turbulent viscosity, as implemented in the OpenFOAM V7 framework. Finally, the walls were considered adiabatic, and `zeroGradient` boundary conditions were imposed for temperature at each boundary. This follows the methodology used by Rodriguez et al. [Rodriguez et al., 2021].

5.2 Case 1: Validation of ECN spray C in-nozzle flow simulation against experimental data

This section explores ECN Spray C in-nozzle flow simulations, juxtaposing them with the findings documented by Tekawade et Al [Tekawade et al., 2020]. In this referenced work, an X-ray-based 3D visualisation of the ECN Spray C internal flow was achieved with an impressive 2 µm pixel resolution. The simulation, conducted at a constant maximum lift [Santos et al., 2020], replicates the injection conditions with a fuel pressure of 150 MPa, an ambient pressure of 0.1 MPa, and a constant temperature of 25 ℃ for both the fuel and the ambient environment. The accuracy of the simulations is assessed by examining the vapour phase distribution within the orifice.

Fig. 5.2 provides a qualitative comparison between our simulation and the experimental results drawn from [Tekawade et al., 2020], as quantitative information cannot be extracted from X-ray phase contrast imaging. These results are presented as slices from the fully reconstructed computed-tomography volume, capturing the flow separation and cavitation cloud throughout the orifice length up to its exit. According to the coordinate system in use, the nozzle tip is defined at $x = 0\,\mu\text{m}$. Areas of high and low intensity correspond to the liquid and gas phases, respectively. The comparison of the two images reveals a high degree of similarity between the simulated and experimental vapour structures.

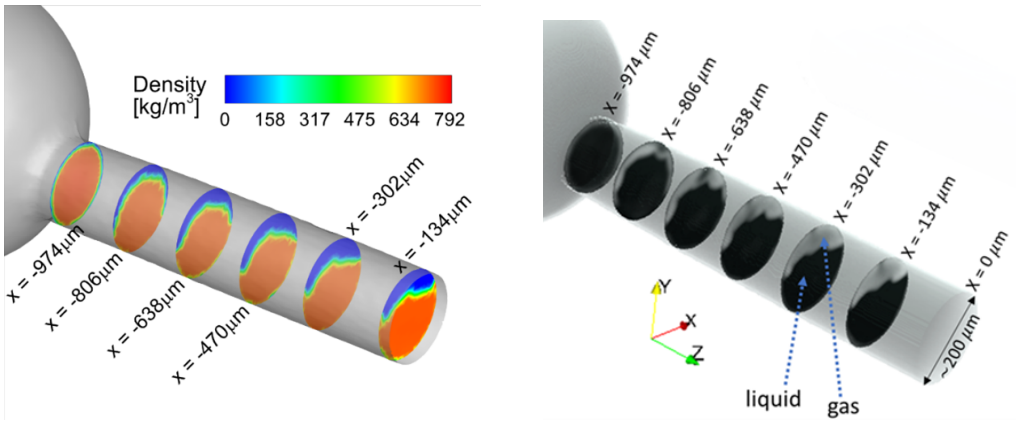

(a) Simulation results. **(b)** Experimental Results.

Figure 5.2: This figure contrasts ECN Spray C in-nozzle flow simulation results (a) with experimental results from [Kyriazis et al., 2017] (b). The experimental image, a slice of the fully reconstructed CT volume, reveals flow separation and cavitation approaching the nozzle exit (nozzle length ~ 1 mm). The coordinate system is defined with $x = 0\,\mu$m at the nozzle tip. Areas of high and low intensity correspond to the liquid and gas phases, respectively.

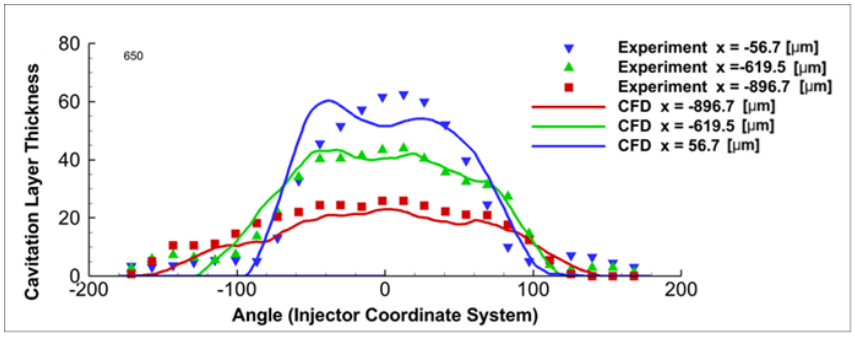

Figure 5.3: Instantaneous gas layer thickness distributions at three cross-sections, plotted as a function of angular position for injection Case A. The experimental results reported in [Tekawade et al., 2020] are compared with the current numerical simulations.

Fig. 5.3 builds upon this analysis by providing a quantitative comparison of the gas layer thickness at three specific cross-sections, defined in terms of angular position. Within this reference framework, the origin is centrally positioned at the orifice exit, and all positions within the orifice are described by negative x coordinates. Following the method described in [Guo, 2020], a gas volume fraction threshold of 0.15 was selected to ensure precise agreement between the simulation and experimental results at the $-896.7\,\mu$m location. This threshold also provided an accurate representation of the gas layer extent and orientation at the other two cross-sections, namely $-619.5\,\mu$m and $-56.70\,\mu$m, albeit with a minor reduction in thickness, which is considered to fall within the experimental uncertainty of X-ray-based visualisation [Karathanassis et al.,

2018]. Even with these slight variations, the overall trend remains consistent with the experimental findings.

Fig. 5.4c illustrates the complex temperature distribution within the injector, providing insights into the contrasting effects of viscous heating and depressurisation-induced liquid cooling. Notably, the figure highlights the substantial shear along the orifice walls, resulting in heating due to viscous forces, with localised near-wall temperatures reaching approximately 313 K. Conversely, it is important to note that in regions of the nozzle orifice adjacent to the walls, where intense cavitation occurs, the temperature drops to around 295 K.

Moreover, Figs. 5.4a and 5.4b illustrate the isentropic expansion of the liquid, leading to cooling as the fluid expands from the inlet pressure and sac temperature to the orifice exit pressure. This cooling process results in a temperature decline to approximately 304 K, consistent with the minimum value observed at the orifice exit. These observations demonstrate that both viscous heating and depressurisation-induced cooling play significant roles in shaping the temperature distribution within the injector. Unlike the barotropic models typically employed for in-nozzle simulations, which do not provide temperature distributions, the methodology presented here can capture these intricate temperature dynamics. This capability is a significant advantage, highlighting the combined effects of viscous heating and depressurisation-induced cooling on the injector's temperature field.

5.3 Case 2: Comparative study of the ECN spray C in Nozzle flow simulation results with existing software

In this section, we replicate the analysis carried out in the previous section (i.e., the Spray C nozzle), albeit under different operating conditions. Here, the focus is on the gas layer thickness at three specific cross-sections, as shown in Fig. 5.5. The results of the present investigation were obtained using purely

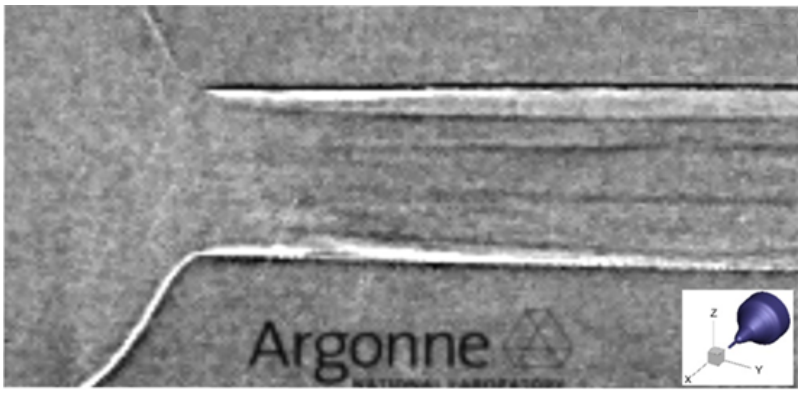

(a) Experimental result.

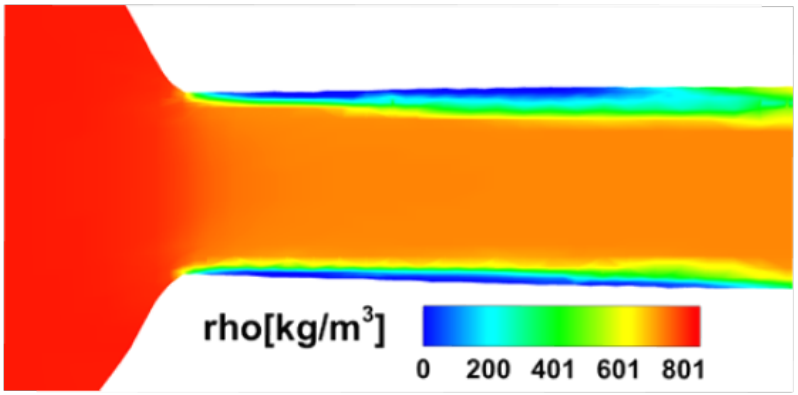

(b) Density distribution inside the injector obtained with `multiCompTabFoam`.

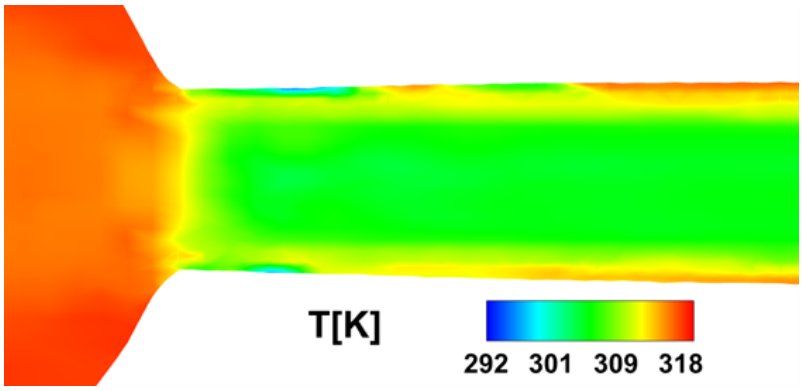

(c) Temperature distribution inside the injector obtained with `multiCompTabFoam`.

Figure 5.4: The three images show: (a) experimental results [Guo, 2020], depicting the phase contrast corresponding to cavitation inside the Spray C injector; (b) simulation results of the density distribution inside the injector, highlighting vapour formation along the walls (obtained with `multiCompTabFoam`); and (c) simulation results of the temperature distribution inside the injector, illustrating the effects of viscous heating, depressurisation-induced liquid cooling, and cavitation (obtained with `multiCompTabFoam`).

physics-informed thermodynamic and phase-change modelling approaches.

The baseline study [Guo, 2020] was performed using the commercial CFD software CONVERGE v2.4. In that study, a large eddy simulation (LES)

framework with the one-equation dynamic structure model was used to model the effect of turbulence on the flow field. Phase change due to cavitation was modelled via the homogeneous relaxation model (HRM), which assumes a first-order relaxation of vapour quality towards the equilibrium value. The gas phases were described by the Redlich–Kwong equation of state (EOS), while the liquid was modelled as compressible using an exponential barotropic fluid assumption. Spatial and temporal discretisation were achieved using second-order and first-order schemes, respectively. A variable timestep algorithm was employed with a maximum CFL number of 0.4.

The parameters for our simulation include n-dodecane as the fuel, an injection pressure of 150 MPa, an ambient pressure of 2.0 MPa, and a fuel temperature of 323 K. Based on the needle profile described in Guo et al. [Guo, 2020], we maintained a constant needle lift corresponding to its position 0.2 ms after the Start of Injection (SOI). The mass fraction of non-condensable N_2 gas was set to 2×10^{-5}.

Findings in Fig. 5.5 show good agreement with those reported in the literature [Guo, 2020]. This comparison is particularly relevant because, unlike established commercial software, where calibration parameters such as liquid saturation density, viscosity, surface tension, or vapour pressure are commonly adjusted, our study adopts a different, tuning-free approach. In the methodology described in this thesis, all thermophysical parameters are considered as functions of internal energy, density, and mass fraction, allowing them to vary throughout the simulations, as explained in Chapter 3.8. This approach provides more detailed insight into the fluid dynamics within the injector, capturing localised temperature variations and enabling the incorporation of novel synthetic fuels or complex fuel mixtures, as demonstrated by the work conducted at City in collaboration with another Ph.D. student [Geber et al., 2023].

This methodology is particularly beneficial in cases where experimental data are limited or unavailable. Indeed, a key limitation of cubic EOSs is that the specified density of the vapour–liquid mixture used by the flow solver may fall between the liquid and vapour saturated densities in the P–T diagram of

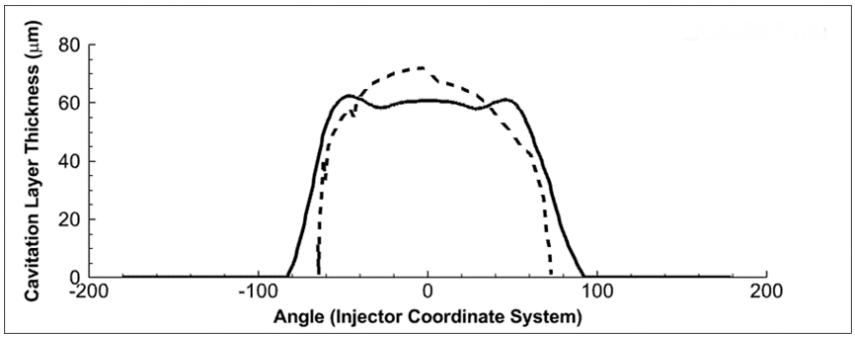

(a) $x = -56.7\mu m$

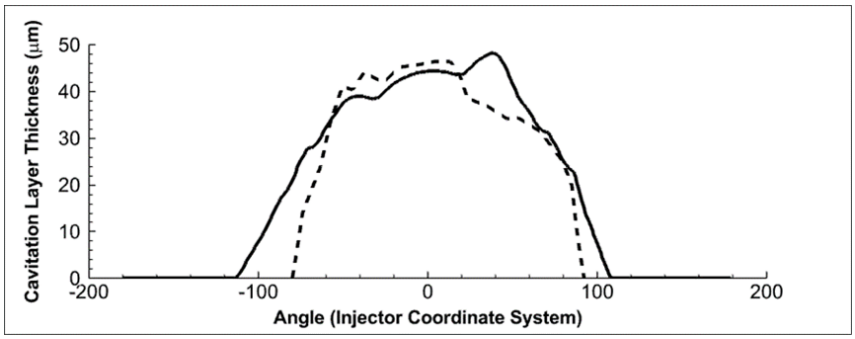

(b) $x = -619.5\mu m$

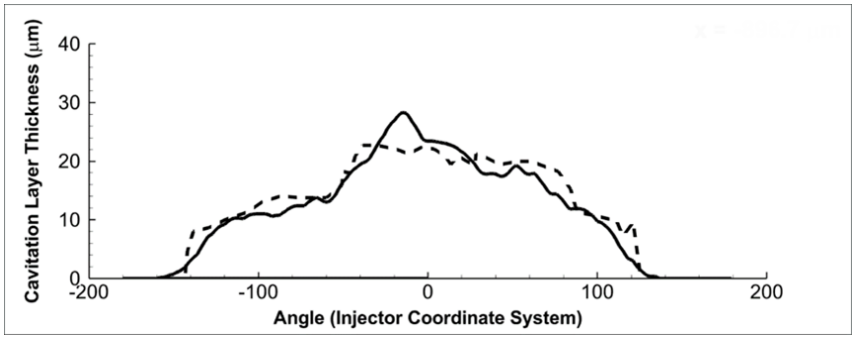

(c) $x = -896.7\mu m$

Figure 5.5: Gas layer thickness plotted as a function of angular position for injection Case B at (a) $x = -56.7\,\mu$m, (b) $x = -619.5\,\mu$m, and (c) $x = -896.7\,\mu$m. Current CFD predictions (solid line) are compared with those reported in [Guo, 2020].

the fuel, rendering the target density unattainable. In contrast, the approach proposed here allows for the calculation of the target density, as it implements the VT Flash algorithm described in the manuscript.

5.4 Case 3: Validation in the spray C near-nozzle spray region

The case discussed in this section was conducted to investigate whether the spray characteristics in the near-nozzle region are influenced by the in-nozzle two-phase flow topology. The same operating conditions used for X-ray radiography measurements of ECN Spray C were replicated, as described in Sforzo et al. [Sforzo, 2019]. Operating conditions included n-dodecane fuel, an injection pressure of 150 MPa, an ambient pressure of 2 MPa, and a uniform temperature of 25 ℃ for both the fuel and the surrounding environment. Previously obtained quantitative measurements using the monochromatic beam of the Advanced Photon Source at Argonne National Laboratory were used to validate the simulation.

Fig. 5.6 shows the sampling location of projected density profiles of the fuel jet at $x = 1$ and $x = 2$ mm with respect to the injector and the geometry.

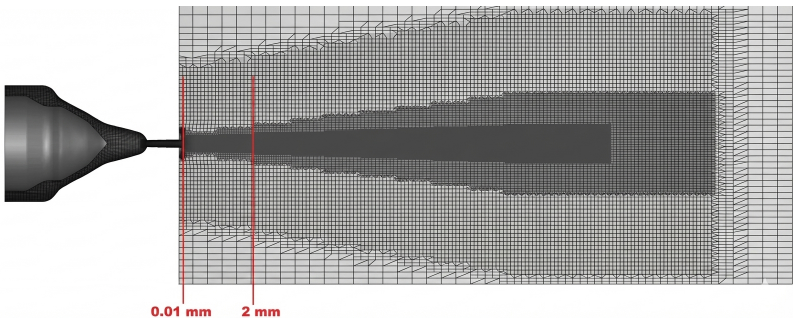

Figure 5.6: Sampling location of projected density profiles of the fuel jet at $x = 1$ and $x = 2$ mm with respect to the injector and the geometry.

The projected density profile represents the total amount of material encountered along a straight line of sight through the object. Mathematically, the projected density (Σ) is the integral of the volume density (ρ) along the z-axis (the direction you are looking), and it is shown in Eq. 5.1.

$$\Sigma(x, y) \ = \int_{-\infty}^{\infty} \rho(x, y, z) \ dz \tag{5.1}$$

The focus on this near-nozzle region was intentional, as it allows a detailed examination of how the complex processes occurring within the nozzle, such as

cavitation evolution, are reflected in the spray pattern just outside the nozzle. The decision to exclude additional density profiles beyond 2 mm is influenced by the divergence between the simulation's classical vapourisation initial conditions and the diffuse-interface VLE assumption, which is more relevant in high-pressure and high-temperature environments [Crua et al., 2017].

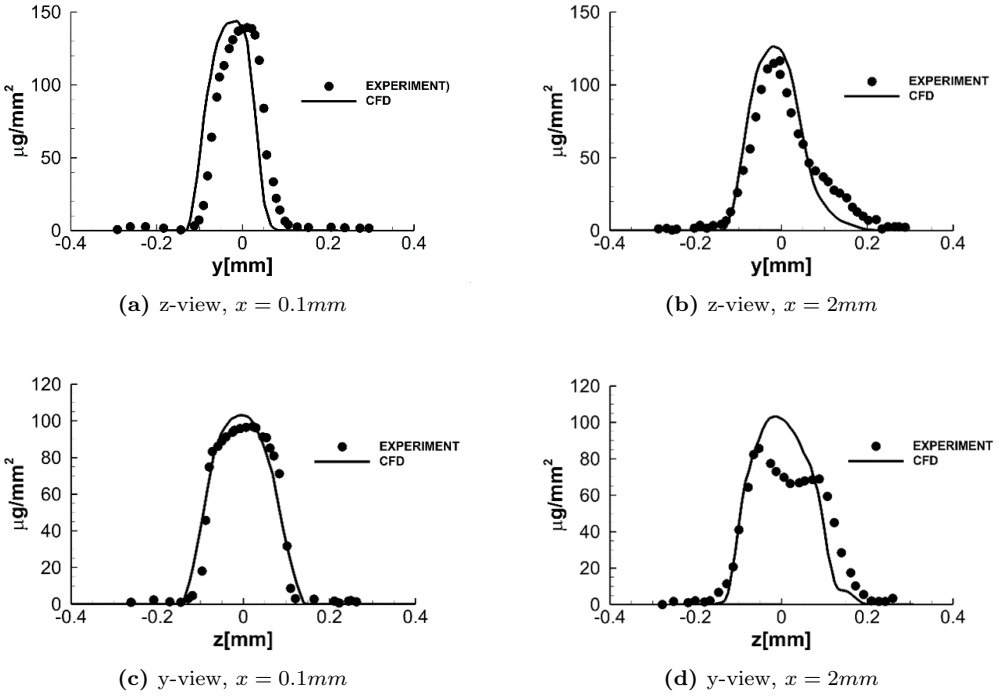

(a) z-view, $x = 0.1mm$ **(b)** z-view, $x = 2mm$

(c) y-view, $x = 0.1mm$ **(d)** y-view, $x = 2mm$

Figure 5.7: Comparison between steady-state projected density profiles of fuel spray obtained from experimental measurements and numerical simulations for Spray C: (a) z-view, x = 0.1 mm, (b) z-view x = 2 mm, (c) y-view, x = 0.1 mm, (d) y-view x = 2 mm.

Fig. 5.7 also reveals the asymmetric nature of the fuel distribution, a direct consequence of cavitation within the Spray C nozzle. The vapour cloud obstructing a portion of the hole exit area leads to a unimodal spray profile skewed in the Y direction, demonstrating the significant impact of the internal nozzle conditions on the emerging spray pattern. The discrepancies observed in Fig. 5.7 can be attributed to the inherent delicacy of X-ray radiography. For instance, uncertainty in the calculation of the absorption coefficient (usually determined in a precursor calibration study) or variation in the beam energy, leading to beam hardening effects, can increase experimental uncertainty [Karathanassis, 2021]. Additional sources of discrepancy include unavoidable

uncertainties in the injector geometry and needle motion, such as wobble. It should be noted that the experimental data were not reported with uncertainty in the original publication.

5.5 Case 4: Simulation of experimental cone angle in ECN spray C

In this final case, the focus is on the experimental cone angle for the ECN Spray C, as documented by the ECN [Sandia, 2023]. In particular, the complete coupling between the cavitation inside the injector and the spray evolution is being taken into account. Moreover, the needle is also moving for a complete coupling between cavitation and spray evolution. This was the most computationally expensive simulation performed in this study. The selected time-step was on the order of 10^{-9} s, owing to the spatial and temporal length scales present in the in-nozzle flow. Finally, being an explicit solver, it has excellent scalability properties.

The cone angle is a critical parameter for understanding how liquid fuel distributes as it is ejected from the injector nozzle, and it is influenced by various factors, including the internal flow dynamics and cavitation within the injector. The simulation initial conditions were set with an ambient temperature of 440 K, a fuel temperature of 363 K, and an injection pressure of 150 MPa. The total simulation time selected for this study was 0.5 ms.

Fig. 5.8a demonstrates that the simulation accurately captures the cone angle for the ECN Spray C. The cone angle was measured by detecting the pixel brightness gradients in high-speed visualisation images, which highlight the local spray periphery [Battistoni and Grimaldi, 2012]. Furthermore, to better visualise the cone angle in Fig. 5.8a, cells in a single-phase state—whether entirely liquid or gas—were assigned a vapour volume fraction of 0.

Fig. 5.9a illustrates the mass fraction within the jet. The image effectively captures the multiphase mixing process, revealing a structure that closely resembles what is typically observed in experimental studies. Furthermore,

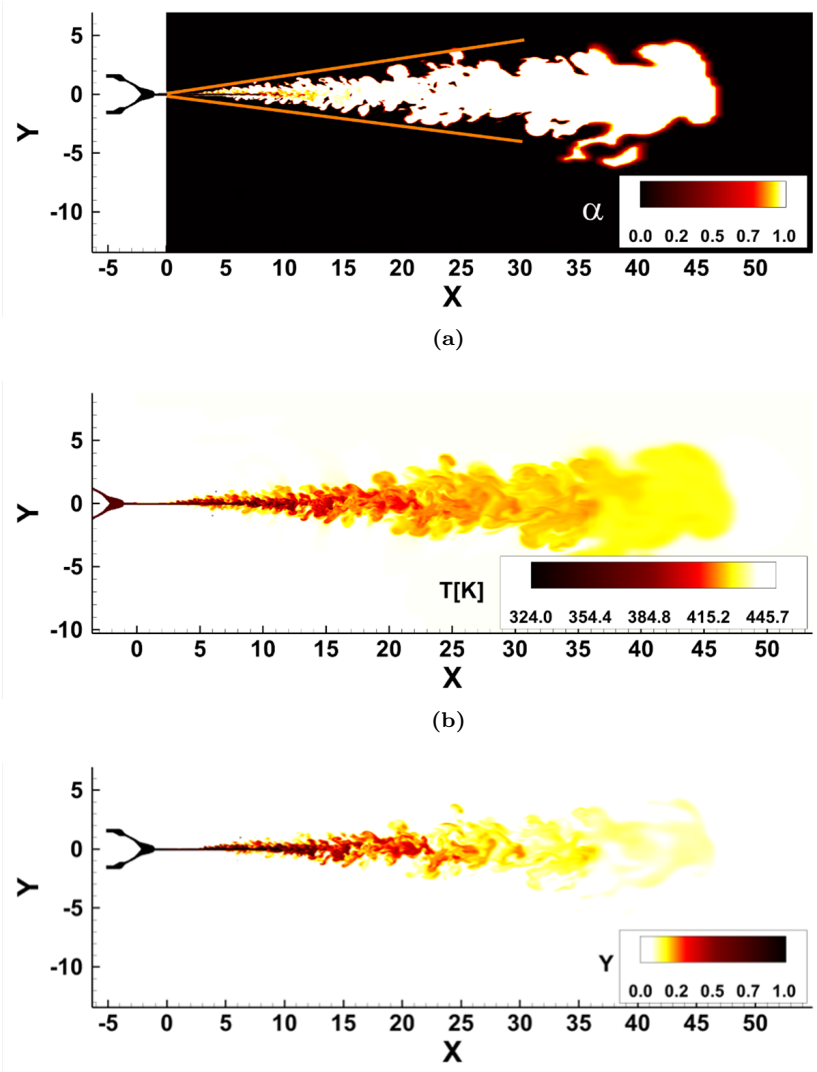

Figure 5.8: Visualisation of spray evolution during the steady injection phase (fixed needle) for Case D, showing the z-view (X–Y plane) as defined in the ECN coordinate system for Spray C injector (Fig. 5.1). ECN measurements of plume growth, experimentally obtained up to 8 mm and subsequently linearly extrapolated, are shown with orange lines in image (a), corresponding to the z-view. Image (a) presents the vapour volume fraction distribution and the experimental cone angle, annotated in orange, measured by detecting pixel brightness gradients in high-speed visualisation images highlighting the spray periphery. Image (b) shows the temperature distribution in the spray region, while image (c) details the fuel mass fraction.

Fig. 5.8b presents the temperature contours for both the in-nozzle and spray regions, clearly showing the rise in fuel temperature as it mixes with the warmer ambient gas within the combustion chamber. Notably, the areas of elevated temperature correspond closely to zones of pronounced shear-flow instabilities, predominantly of the Kelvin–Helmholtz type, which mark the initial stages of jet disintegration, as shown in Figs. 5.8c and 5.9c.

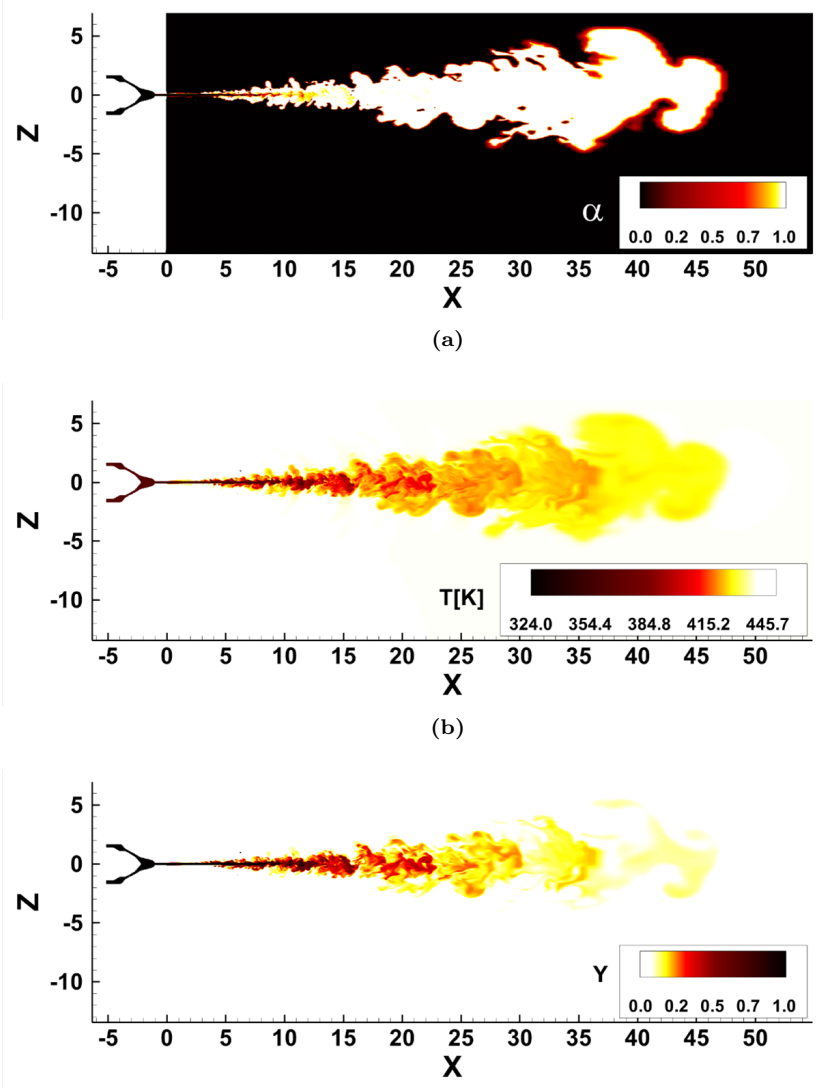

Figure 5.9: Visualisation of spray evolution during the steady injection phase (fixed needle) for Case D, showing the y-view (X–Z plane) as defined in the ECN coordinate system for Spray C injector (Fig. 5.1). Image (a) presents the vapour volume fraction distribution and the experimental cone angle, annotated in orange, measured by detecting pixel brightness gradients in high-speed visualisation images highlighting the spray periphery. Image (b) shows the temperature distribution in the spray region, while image (c) details the fuel mass fraction.

5.6 Limitations and Critical Review

In this section, the main goal was to demonstrate the capability of the new solver to simulate cavitation in different nozzles and to show how it affects both in-nozzle flow and spray behaviour under realistic thermodynamic conditions. All results have been compared and validated against experimental or numerical data, showing good agreement. This is particularly noteworthy,

as the model and the Equation of State (EoS) do not involve any empirical tuning, and realistic operating conditions were employed throughout.

The primary limitation of this section is the scarcity of comparative data, particularly experimental results, due to the low replicability of experiments for assessing cavitation within the nozzle and the quantitative evolution of the spray. Nevertheless, the new solver can be employed to study different nozzle designs and investigate their in-nozzle and spray behaviour.

Another critical aspect for future improvement would be the incorporation of predictive models to better simulate and understand both in-nozzle flows and spray atomisation. A recent study by Liu [Liu et al., 2024] addressed this by developing reliable correlations for Lagrangian engineering simulations to predict the onset of cavitation. Using extensive data generated from high-fidelity Eulerian volume-of-fluid (VOF) simulations of a single-hole injector across a wide range of operating conditions, appropriate discharge (C_d, how much mass is actually coming out compared to what theory says should come out) and contraction (C_a, how much the nozzle area is reduced following the vena contracta formation due to cavitation or recirculation areas) coefficients were determined. Four significant factors characterising nozzle geometry were considered: the K factor (standard industry metric used to quantify the taper (conicity) of the nozzle hole. It describes whether the hole gets narrower or wider as the fluid flows through it. The K-factor is calculated based on the difference between the inlet and outlet diameters), inlet curvature radius, nozzle exit radius, and channel length, as well as ambient and injection pressures. The results indicated that a larger K factor and inlet curvature radius yielded higher C_d and C_a values, whereas the exit radius and channel length had a less significant effect on cavitation dynamics. A smaller pressure difference between the nozzle inlet and exit mitigated cavitation formation. In their study, Liu showed that, using these correlations, it was possible to describe cavitation effects on in-nozzle flow and spray atomisation via a mathematical regression model. Furthermore, two additional correlation models based on regression learners and artificial neural networks were developed. Of the three models, the mathematical regression model showed the best agreement with

an external validation dataset. This approach illustrates the potential of CFD combined with machine learning to optimise injector design and operation, and represents a promising direction for future research.

Chapter 6

Conclusions and Future Work

The CFD solver `multiCompTabFoam` has been implemented and employed to simulate various test cases, validated against analytical solutions, simplified numerical solutions, and published numerical and experimental data from multiple sources. In particular, it was initially validated against the Shock tube problem, demonstrating that wave patterns are accurately captured. Subsequently, it was tested against the solution of the Rayleigh–Plesset equation, showing that the methodology can accurately predict the dynamic evolution of the bubble radius over time.

The algorithm was then validated against a series of published results, including two specific sets of numerical data: a single bubble collapsing close to a wall at different SOD, and a cluster of bubbles collapsing near a rigid wall. The solver exhibited excellent performance compared to the literature, while also enabling the study of heat transfer between phases and its effects. Additionally, an analysis comparing different fuels for a DFICE was performed, specifically comparing dodecane and two short-chain alcohols, showing that short-chain alcohols could help mitigate erosion during DFICE operation.

The solver has also been tested and validated for cases of multicomponent mixtures. The main novelty of this work lies in the implementation of a robust and computationally efficient flow solver based on the highly accurate PC-SAFT Equation of State for thermodynamic closure. The capability to concurrently predict in-nozzle flow and spray atomisation under sub- and

supercritical pressure and temperature conditions advances the current state of the art in numerical tools for highly compressible flows. Its effectiveness was confirmed through detailed comparisons with experimental data, demonstrating its accuracy in predicting flow characteristics such as the gas layer thickness, projected density profiles near the nozzle, and the spray cone angle.

By leveraging PC-SAFT, VLE computations, entropy scaling methodologies, and group contribution methods, the model accounts for thermal effects and local variations of thermophysical properties, while also incorporating real-fluid behaviour in capturing phenomena such as cavitation, atomisation, and vaporisation under high-pressure and high-temperature conditions. The model's adaptability, lack of reliance on adjustable parameters, and consistency with precise experimental results further affirm its reliability.

This has also resulted in the successful completion of all objectives defined at the beginning of the project.

6.1 Future Work

The present research and developed methodology can be further expanded to address Fluid-Structure Interaction problems. The input to the solid mechanics solver would be the velocity and pressure fields calculated from the Navier-Stokes equations, and the output would predict deformation of injector walls (or any surface in contact with cavitation) and possible rupture, providing a more accurate estimate of whether the liquid jet velocity could cause material loss or, more generally, mechanical fatigue.

Another path would be to enhance the integration of turbulence, cavitation, and combustion coupling, enabling a more comprehensive description of injection-driven combustion dynamics under engine-relevant conditions. This could also reveal how cavitation affects combustion efficiency. According to theory, cavitation is expected to increase the spray cone angle and spray penetration length, thereby enhancing combustion performance.

Another natural extension of this work would be to continue studying cavitation inside injectors and spray evolution using `multiCompTabFoam` under

different fuels and operating conditions. Since the code has been extensively validated for multicomponent mixtures, the next step would be to study cavitation evolution for various geometries relevant to DFICE-powered powertrains and fuels and optimise them, in order to facilitate a phased transition to a green automotive sector.

Ultimately, as the project's final goal, a comprehensive database of simulations with various initial conditions, fuels, and geometries could be created and incorporated in the ECN database. A machine learning algorithm could be developed to predict when and how cavitation would occur based on a few simple input parameters, thereby dramatically reducing computational costs.

Appendix A

Technical parameters of the PC-SAFT closure

This appendix provides more detailed technical information on the PC-SAFT thermodynamic closure. The details and results presented here are taken from the technical paper of Geber et al. [Geber et al., 2023], with whom a close collaboration was maintained during the PhD period.

PC-SAFT is a theoretically derived model based on perturbation theory, which divides the intermolecular potential energy of the fluid into repulsive and attractive contributions.

In PC-SAFT, a reference fluid is defined to calculate the repulsive contribution. This reference fluid consists of spherical segments forming a hard-sphere fluid, which then assembles into molecular chains to create the hard-chain fluid. The attractive interactions, treated as perturbations to the reference system, are accounted for through the dispersion term [Gross and Sadowski, 2001]. In addition to these two basic contributions, the association term can also be included to account for intermolecular bonds forming between hard-sphere segments with association sites (proton donor and acceptor) [Gross and Sadowski, 2002]. The hydrogen bonds formed by the $-OH$ group of alcohols are an example of self-association [Chapman et al., 1990], which will be modelled and discussed in this appendix.

The PC-SAFT equation of state (EoS) is based on the Helmholtz free

energy, expressed as the sum of the hard-chain, dispersion, and association contributions, as shown in Eq. (A.1) (and illustrated in Fig. 3.1).

$$\tilde{a}^{\text{res}} = \tilde{a}^{\text{hc}} + \tilde{a}^{\text{disp}} + \tilde{a}^{\text{assoc}} \tag{A.1}$$

The hard-chain term $\tilde{a}^{\text{hc}}$ for a mixture of n_c components is given by:

$$\tilde{a}^{\text{hc}} = \bar{m}\tilde{a}^{\text{hs}} - \sum_{i=1}^{n_c} x_i(m_i - 1) \ln g_{ii}^{\text{hs}}(\sigma_{d,ii}) \tag{A.2}$$

Where $\bar{m}$ is the number of segments for a multicomponent mixture, x_i is the mole fraction of component i, $\tilde{a}^{\text{hs}}$ is the hard-sphere fluid contribution, g_{ii}^{hs} is the radial distribution function of the hard-sphere fluid, and m_i is the number of segments per chain for component i.

The dispersion term is defined in Eq. A.3.

$$\tilde{a}^{\text{disp}} = -2\pi\rho\bar{m}^2\varepsilon\sigma_d^3 I_1(\eta, \bar{m}) - \pi\rho\bar{m}^2 C_1 \varepsilon^2 \sigma_d^3 I_2(\eta, \bar{m}) \tag{A.3}$$

The association contribution to the Helmholtz free energy is linear for mole fractions and is given by Eq. A.4.

$$\tilde{a}^{\text{assoc}} = \frac{1}{RT} \sum_i x_i \left(\sum_{A_i} \left(\ln X_{A_i} - \frac{X_{A_i}}{2} \right) + \frac{M_i}{2} \right) \tag{A.4}$$

where M_i is the number of association sites on each molecule of component i, and X_{A_i} is the mole fraction of molecules not bonded at site A for component i, given by Eq. A.5.

$$X_{A_i} = \left(1 + \sum_j \rho_j \sum_{B_j} X_{B_j} \Delta_{A_i B_j} \right)^{-1} \tag{A.5}$$

The summation over B_j represents summation over all sites on molecules of component j (e.g., A_j, B_j, C_j). Also, $\rho_j = x_j \rho_{\text{mixture}}$ is the molar density, and $\Delta_{A_i B_j}$ is the association strength.

The mixture parameters σ_{ij} and ε_{ij} for every pair of unlike segments are modelled using the Berthelot-Lorentz combining rules, Eq. A.7.

$$\sigma_{ij} = \frac{1}{2}(\sigma_i + \sigma_j) \tag{A.6}$$

$$\varepsilon_{ij} = \sqrt{\varepsilon_i \varepsilon_j (1 - k_{ij})} \tag{A.7}$$

where k_{ij} is the binary interaction parameter. These mixture parameters are used in the computation of $\bar{m}^2\varepsilon^2\sigma_d^3$ in Eq. (3.22).

The main input parameters needed for the PC-SAFT calculations are the number of segments per chain (m), the segment diameter (σ) and the depth of pair potential divided by the Boltzmann constant (ϵ/k), and they must be defined for each component individually. Values that have been adjusted using experimental density and vapour pressure data can be found in the literature [Gross and Sadowski, 2002, 2001, Tumakaka and Sadowski, 2004]. To provide a generic and predictive methodology for fuel-property calculations, a Group Contribution (GC) method is employed for estimating the input parameters. The GC method of Tihic et al. [Tihic et al., 2008] is implemented.

The chemical structure of the molecule is divided into simple, first-order groups (FOG) and more complex, second-order groups (SOG). The PC-SAFT parameters m, σ, and ε/k are computed as a function of all the individual group contributions m_i, σ_i, and ε/k_i according to Eqs. A.8, A.9, and A.10.

$$m = \sum_{\text{groups}} (n_i m_i)^{\text{FOG}} + \sum_{\text{groups}} (n_i m_i)^{\text{SOG}} \tag{A.8}$$

$$m\sigma^3 = \sum_{\text{groups}} (n_i m_i \sigma_i^3)^{\text{FOG}} + \sum_{\text{groups}} (n_i m_i \sigma_i^3)^{\text{SOG}} \tag{A.9}$$

$$m\frac{\varepsilon}{k} = \sum_{\text{groups}} \left(n_i m_i \frac{\varepsilon_i}{k_i} \right)^{\text{FOG}} + \sum_{\text{groups}} \left(n_i m_i \frac{\varepsilon_i}{k_i} \right)^{\text{SOG}} \tag{A.10}$$

The computation of the individual group contributions relies on the fitting of vapor pressure and liquid density data at a reduced temperature range of $0.5 \leq T_r \leq 0.9$.

The work of Burgess et al.[Burgess et al., 2014] is also used in cases where a

weak performance of the thermodynamic model is observed. While the above equations remain valid, the values of m_i, $m_i\sigma_i^3$, and $m_i\varepsilon_i/k_i$ for each first-order and second-order group are different.

The method of Burgess et al. [Burgess et al., 2014] aims to improve performance under high- and low-pressure conditions by creating two different sets of GC parameters: one derived from experimental data at low pressure (below 7 MPa), and another at high pressure (7 MPa up to 276 MPa).

For the OME_n fuel family, a model developed by Schappals et al. [Schappals et al., 2017] is also investigated as a possible solution. In this approach, the number of segments m in OME_n is assumed to be linearly dependent on the OME chain length n, while the parameters σ and ϵ/k are considered constant. This is a rather simple approach, developed through fitting of experimental vapour pressure and liquid density data in the temperature range of 300–500 K and pressures of 1 bar and below. Therefore, it serves as a good reference for comparison with the more generic GC method. All the input parameters of the individual components for the PC-SAFT formulations are listed in Tabs. A.1, A.2, and A.3.

For associating components, the bonding type must be defined. In the case of alkanols, the 3B and 2B bonding models were proposed by Huang et al. [Huang and Radosz, 1990]. However, since the use of the more complex 3B model could not be sufficiently justified, the simpler 2B model was adopted in this work. The study of Gross et al. [Gross and Sadowski, 2001] also successfully applied the 2B model to describe substances such as ethanol, methanol, and pentanol. Therefore, the 2B bonding approach was selected as the most suitable option for this study.

Two additional pure component parameters, the effective association volume (k_{AB}) and the association energy (ε_{AB}/k), are used for associating components. These parameters can also be estimated using the GC method proposed by Tihic et al. [Tihic et al., 2008].

Finally, for the estimation of the binary interaction parameter k_{ij}, the method of Stavrou et al. [Stavrou et al., 2016] was used. In the proposed Quantitative Structure–Property Relationship (QSPR) method, k_{ij} is calcu-

Table A.1: Individual component PC-SAFT input parameters estimated with the method of Tihic et al. [Tihic et al., 2008].

Compound	m	σ	ε/k	k^{AB}	ϵ^{AB}/k
n-pentane	2.69	3.77	231.20		
isooctane	3.14	4.09	249.77		
n-undecane	4.91	3.89	248.82		
Isopentane	2.56	3.83	230.75		
Cyclopentane	2.36	3.71	265.83		
Hexene	2.98	3.77	236.81		
Toluene	2.81	3.72	285.69		
heptane	3.48	3.80	238.40		
octadecane	7.44	3.95	254.90		
pentamethyl heptane	3.88	4.25	273.72		
heptamethyl nonane	5.60	4.16	266.46		
1-methylnaphthalene	3.42	3.90	338.79		
Tetralin	3.09	3.99	337.46		
1,2,4-trimethylbenzene	3.61	3.75	284.25		
OME3	5.85	3.01	220.84		
OME4	7.08	2.98	221.75		
methanol	1.52	3.23	188.90	0.035	2899.50
ethanol	2.38	3.18	198.24	0.032	2653.40
propanol	3.00	3.25	233.40	0.015	2276.80
butanol	2.75	3.61	259.59	0.007	2544.60
pentanol	3.63	3.45	247.28	0.010	2252.10

Table A.2: Individual component PC-SAFT input parameters estimated with the method of Burgess et al. [Burgess et al., 2014].

Compound	m	σ	ϵ/k
pentamethyl heptane	5.25	3.86	224.88
heptamethyl nonane	7.14	3.85	227.96

Table A.3: Individual component PC-SAFT input parameters estimated by the method of Fletcher et al. [Schappals et al., 2017].

Compound	m	σ [Å]	ε/k [K]
OME_3	4.05	3.55	260
OME_4	4.83	3.55	260

lated using the following Eq. A.11.

$$k_{ij}^{\mathrm{QSPR}} = \sum_{L=1}^{N_d} c_L D_L(\bar{p}_i, \bar{p}_j) \tag{A.11}$$

Where N_d is the number of descriptors, $D_L(\bar{p}_i, \bar{p}_j)$ are the descriptors, and c_L are the corresponding regression coefficients. The descriptors are functions of the PC-SAFT molecular parameters.

Since all fuel mixtures considered have non-polar components and only up to a single associating component, one descriptor is used, as expressed in Eq. A.12.

$$D^{LJ} = 1 - \left[\frac{\sigma_i^3}{\sigma_j^3} \left(\frac{\varepsilon_i/k}{\varepsilon_j/k} \right)^2 \right] \tag{A.12}$$

The value of the c^{LJ} coefficient can be found in the tables of the work by Stavrou et al. [Stavrou et al., 2016].

The vapor-liquid equilibrium (VLE) calculations are performed under constant temperature, specific volume, and composition, and are based on the unconstrained minimisation of the Helmholtz free energy. The choice of temperature, specific volume (or density), and composition as independent variables is suitable, as in PC-SAFT, all equations are expressed as functions of these variables. More importantly, the use of density instead of pressure as an independent variable allows for a better description of the phase change.

In the case of a single component or a multi-component mixture with very similar components, phase change occurs at constant or nearly constant pressure. Therefore, a pressure-based code would compute only a single point in the vapour-liquid equilibrium, reducing the entire phase change process to one state.

The algorithm consists of two stages: the stability analysis and the flash calculations. First, the mixture is assumed to be in a single-phase state, and its stability is investigated through the Tangent Plane Distance (TPD), in a manner similar to the work of Michelsen and Mollerup [Michelsen and Mollerup, 2007]. If the TPD, calculated according to Eq. (A.13), is always non-negative,

the mixture is considered stable. Otherwise, the system is unstable, and flash calculations are performed to determine the composition of the two-phase mixture. The existence of a non-negative minimum of the TPD is sufficient to prove the mixture's stability; thus, this is formulated as a minimisation problem in Eq. A.13.

$$\mathrm{TPD} = \frac{P' - P^*}{RT} + \sum_{i=1}^{n_c} \rho' x'_i \log\left(\frac{f'_i}{f^*_i}\right) \tag{A.13}$$

In Eq. (A.13), the primes ($'$) refer to the trial phase and the asterisks (*) to the feed conditions. R is the universal gas constant, f_i is the fugacity of component i, P is the pressure, ρ is the density, and n_c is the number of components.

For the initialisation of the iterative minimisation process, Raoult's law and Wilson's correlation [Wilson, 1969] are combined with the work of [Michelsen, 1982*b*] and Mikyska and Firoozabadi [Mikyska and Firoozabadi, 2012] to obtain the initial estimates for the liquid (y_i) and vapour (x_i) phase compositions, where z_i denotes the initial overall composition, as shown in Eq. 2.14.

$$x_i = \frac{z_i / P_i^{\mathrm{sat}}}{\sum_{i=1}^{n_c} z_i / P_i^{\mathrm{sat}}}, \quad y_i = \frac{z_i P_i^{\mathrm{sat}}}{\sum_{i=1}^{n_c} z_i P_i^{\mathrm{sat}}} \tag{2.14}$$

If a two-phase regime is detected during the stability analysis, the code proceeds with flash calculations, aiming to minimise the Helmholtz free energy at a given density, temperature, and composition.

During these flash calculations, the vapor mole fraction β is computed in Eq. A.14.

$$\beta = \sum_{i=1}^{n_c} n_{v,i} \tag{A.14}$$

From this, the compositions and densities of the vapour and liquid phases can be derived using Equations A.15, where ρ_v and ρ_l are the densities of the liquid phases. The compositions and densities of the vapour and liquid phases are also expressed in Eq. A.15.

$$x_i = x_i^{\text{inv}}, \quad y_i = y_i^{\text{inl}}, \quad \rho_v = \frac{\beta}{V_v}, \quad \rho_l = \frac{1-\beta}{V_l} \tag{A.15}$$

In both the stability analysis and the flash calculations, the optimisation problem is solved using Newton's method [Nocedal and Wright, 2006]. To calculate the step length in Newton's method, an inexact line search is applied, ensuring that the step satisfies the Wolfe conditions [Fletcher, 2013].

The Newton step direction p_k is determined by solving the following linear system shown in Eq. A.16.

$$\nabla^2 f_k \, p_k = -\nabla f_k \tag{A.16}$$

where $\nabla^2 f_k$ is the Hessian matrix and ∇f_k is the gradient of the objective function at iteration k.

For Equation A.16 to have a solution, the Hessian must be positive definite. To ensure this condition, a modified Cholesky factorisation algorithm is used.

Appendix B

Immersed Boundary Methodology

This appendix provides a more rigorous description of the Immersed Boundary (IB) forcing formulation. The concept is based on the work of [Stavropoulos Vasilakis et al., 2019], and its implementation has been adapted to the current methodology and solver in OpenFOAM V7, as described in this thesis.

As noted in Eq. 3.16, the immersed boundary is modelled through the addition of the volumetric source term f_{ib} in the momentum equation (Eq. 3.14). The immersed solid boundary is represented by a surface mesh, and a colour function is used to identify the solid or IB cells and the computational grid cells enclosed by this surface. Figure B.1 shows the triangulated surface of a cylinder and the corresponding projection via the colour function in the computational domain.

The default OpenFOAM octree-search algorithm is initially used to identify grid cells whose centres lie inside the IB shell. The solid stencil is then extended to include grid cells intersected by the IB surface. The colour function (also referred to as the IB mask), representing the solid region, corresponds to the solid volume fraction of the cells. This function takes continuous values between 0 for fluid cells and 1 for solid cells, with intermediate values representing the interface between the solid and fluid regions.

For each computational cell, the mask is calculated as the average of the

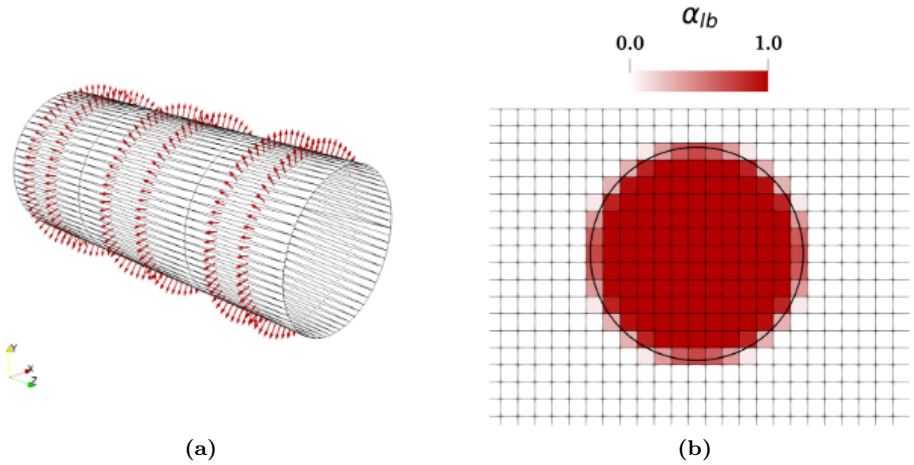

Figure B.1: Representation of the immersed boundary using a triangulated surface, showing the corresponding surface normals (a) and its projection onto the computational grid via the IB mask α_{ib} (b).

normal distances of all its vertices from the IB surface. The signed distance of each vertex from the nearest IB surface point is computed, with negative values indicating a vertex located in the solid region, as illustrated in Fig. B.2. The sum of the distances of vertices inside the solid region is then divided by the sum of the distances of all vertices. This procedure is expressed in Eq. B.1 for each of the N_c cells with N_v vertices.

$$\alpha_j = \frac{\sum_{i=1}^{N_v} |\min(d_{n,ij}, 0)|}{\sum_{i=1}^{N_v} |d_{n,ij}|}, \qquad j \in [1, N_c] \tag{B.1}$$

The forcing source term, introduced in Eq. B.2 (and also used in Eq. 3.16), is calculated as the difference between the fluid velocity and the IB solid velocity, divided by the time step. By multiplying this term by the IB mask, the source is localised across all cells within the IB region, rather than only at the interface.

$$\vec{f}_{ib} = \alpha_{ib} \frac{\vec{u}_{ib} - \vec{u_{fluid}}}{\Delta t}, \qquad \alpha_{ib} \in [0, 1] \tag{B.2}$$

The term is designed to drive the solution of the equation towards the desired velocity in the IB region, thereby imposing a no-slip condition on the IB cells. The target velocity for each computational cell in the IB region is calculated at the centre of gravity of the IB surface, accounting for the body's

rotation, as $\vec{u}_{ib,j} = \vec{u}_G + \vec{r}_j \times \omega_G$. This procedure is illustrated in Fig. B.2b.

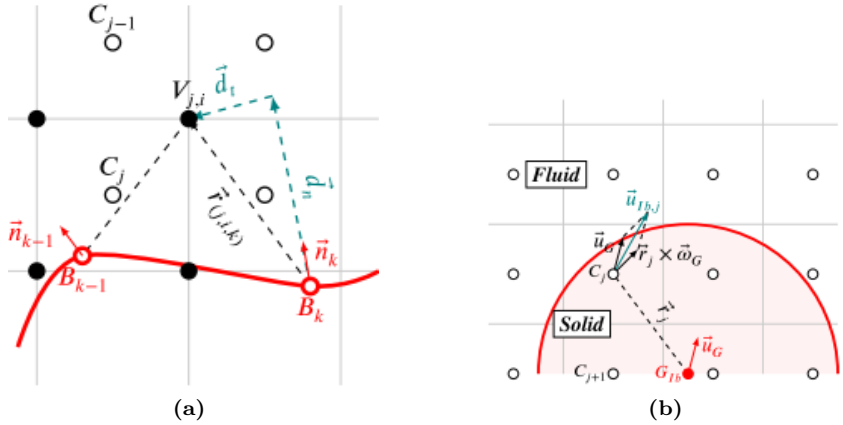

Figure B.2: Calculation of the distance of each grid node from the IB surface (a) and of the target velocity for each cell within the IB region (b).

When the IB methodology is combined with the explicit density-based algorithm (as in the solver introduced in this thesis), the forcing term is updated once at the beginning of the time step and then integrated as part of the momentum equation according to the RK4 scheme.

The IB methodology is particularly relevant for injector cases involving needle movement, as it allows the modelling of the flow field at zero lift, where the needle remains closed. Many numerical studies of these flows accommodate the needle movement through either complete remeshing of the domain [Huang et al., 2013], cell layer addition and inflation [Koukouvinis, Gavaises, Li and Wang, 2016], or interpolation between grids of different resolution but the same cell count [Santos et al., 2020]. Only a few studies employ cut-cell IB methods, which, however, do not permit the needle to fully close and require a minimum lift [Orley et al., 2015, Battistoni and Grimaldi, 2012]. While cut-cell methods could be an alternative, the Cartesian background geometry would require an excessive number of cells to resolve the small needle/needle-seat gaps. Accurate simulation of needle movement, including the fully closed position, is essential for capturing pressure-wave dynamics and the residual fuel in the injector sac volume between successive injection events—a phenomenon that significantly affects nozzle wall wetting and emissions, as demonstrated by recent work from the author's group.

The IB methodology described in this Appendix overcomes the staircase

issue at interface cells and avoids the cumbersome interpolation procedures, the need to define every intersection of the body geometry with the computational grid, or the sophisticated sub-grid reconstruction required in other immersed boundary methods. Consequently, it benefits from a simpler formulation. Compared to alternative approaches, this method offers a computationally efficient solution for complex flows in domains with moving geometries. Its significantly lower computational cost compared with sliding conforming grids, and the simpler algorithm compared with remeshing techniques, are major advantages. The method has been successfully applied to turbulent cavitating flows with moving boundaries, characterised by highly transient phenomena, for which the computational cost of conforming grid techniques would be prohibitive. Its performance has been assessed against experimental data, computational results from the literature, and, where possible, conformal grid simulations, as reported in [Stavropoulos Vasilakis et al., 2019].

Appendix C

Local Time Stepping

This appendix provides a more rigorous and thorough description of the Local Time Stepping (LTS) concept and formulation. The methodology is based on the work of Espinoza [Espinoza et al., 2015], and the implementation has been adapted to the solver and methodology used in OpenFOAM V7, as described in this thesis.

To capture the essential flow features satisfactorily, good practice dictates a specific set of procedures. These include categorising the relevant physics and selecting appropriate solution methodologies. While significant research has focused on these aspects, the spatial and temporal resolution of calculations is also critical to achieving accurate numerical results while minimising computational expense.

Regarding spatial resolution, a computational mesh that adequately follows shock structures is essential. Tetrahedral meshes can be created more quickly than structured ones and provide greater flexibility, particularly for complex geometries. However, poor predictions of heat transfer can result. Therefore, standard practice for unstructured meshes involves using prismatic cells aligned with solid surfaces and shock waves. Alignment with the shock wave is particularly important to avoid significant fluctuations in predicted stagnation-point heat flux. Additionally, sufficient cell refinement is required near the shock wave to properly capture the spatial variation of flow properties. In this work, the BlockMesh and SnappyHexMesh tools within OpenFOAM

have been used to achieve the necessary cell refinement for single-bubble collapse cases, bubble clusters, and in-flow and spray simulations.

The temporal advancement must also preserve numerical stability and accuracy. The LTS methodology presented here (derived from [Espinoza et al., 2015]) enables a time-acceleration technique that can significantly accelerate the computation of initial transients and, therefore, the convergence towards steady-state solutions.

Local Time Stepping (LTS) is a technique used to accelerate the convergence of computations towards steady-state solutions. As *rhoCentralFoam* is an unsteady solver, the solution initially undergoes a transient before reaching steady state. The *rhoCentralFoam* solver was used as the baseline for developing the solver presented in this thesis, *multiCompTabFoam*. In its original form, *rhoCentralFoam* advances all cells in the computational domain using the same time step, which is limited by the smallest allowable step for any cell. In contrast, LTS allows each cell to advance using its own time step.

The original Navier–Stokes equations are expressed in Eq. C.1.

$$\frac{\partial \vec{W}}{\partial t} + \nabla \cdot \vec{F} = \vec{S} \tag{C.1}$$

Where $\vec{W}$ represents the conserved variables, $\vec{F}$ the fluxes, $\vec{S}$ the source terms, and t the time. LTS technique solves the equation as expressed in Eq. C.2.

$$\frac{1}{a}\frac{\partial \vec{W}}{\partial t} + \nabla \cdot \vec{F} = \vec{S} \tag{C.2}$$

where a is the accelerator factor that depends on $\vec{W}$. If the solution is steady, then the time derivative is exactly zero, and so a solution to Eq. C.2 is also a solution of Eq. C.1, independent of the value of a. In the LTS procedure that has been implemented into OpenFOAM V7 during this project, the time derivative is modelled using an Euler scheme. The time-step t for each cell is selected individually as the minimum between the global, user-defined maximum time-step t_{max}, and the time-step that is determined by the maximum allowable Courant number C_{max} within the flow. This is shown in

Eq. C.3.

$$\Delta t = \min(\Delta t_{max}, \Delta t(C_{max})) \tag{C.3}$$

In practice, the field Δt calculated using this approach is first smoothed spatially before being applied to the calculation of the LTS solution in each computational cell.

As explained in Espinoza [Espinoza et al., 2015], the implementation of the LTS technique has resulted in a significant reduction of the computational time for the simulation of the Couette flow, matching the analytical solution to within 1.03% error and being 2.56 times faster than the unmodified solver. In the cases studied within this PhD thesis, the computational time has been reduced to less than 1/3 thanks to this LTS approach.

Appendix D

Exact Riemann Problem solution for an arbitrary equation of state

This appendix illustrates the methodology for finding the exact solution to the shock tube problem for the Euler equations, for an arbitrary equation of state of the form $p = f(\rho, e)$. This analytical solution has been used in Chapter 4.1 to validate the newly developed solver in the case of a simple 1D shock tube case, as shown in Fig. 4.1.

The equation of state may be provided in closed form, where simplifications as in Toro [Toro, 2009] may be done, or in a general tabular form (Additional information might be found in [Menikoff and Plohr, 1989, Le Métayer et al., 2005, Muller and Voss, 2006, Petitpas et al., 2009]).

The form of the Riemann problem solved is shown in Eq. D.1.

$$\frac{\partial \vec{U}}{\partial t} + \frac{\partial \vec{F}(\vec{U})}{\partial x} = 0, \tag{D.1}$$

Where the initial conditions are defined in Eq. D.2.

$$U(x,0) = \begin{cases} U_L, & x < 0, \\ U_R, & x > 0. \end{cases} \tag{D.2}$$

$\vec{U}(x,t)$ is the vector of conservative variables and $\vec{F}(\vec{U})$ is the flux vector, as shown in Eq. D.3

$$U = \begin{bmatrix} u \\ E \end{bmatrix}, \qquad F(U) = \begin{bmatrix} u \\ u^2 + p \\ u(E+p) \end{bmatrix}, \tag{D.3}$$

where $E = \frac{1}{2}u^2 + e$, with e being the internal energy.

The Jacobian matrix $\vec{A}(\vec{U})$ is shown in Eq.

$$\vec{A}(\vec{U}) = \begin{bmatrix} 0 & 1 & 0 \\ \frac{\partial p}{\partial \rho} + \frac{\frac{\partial p}{\partial e} + (u^2 - 2e) - 2\rho u^2}{2\rho} & u\left(2 - \frac{\partial p}{\partial e}\right) & \frac{\partial p}{\rho \partial e} \\ u\left[2p + \frac{\partial p}{\partial e}\left(2e - u^2\right) + \rho\left(u^2 - 2\frac{\partial p}{\partial \rho} + 2e\right)\right] & \left(\rho - 2\frac{\partial p}{\partial e}\right)u^2 + 2p + 2e\rho & \left(\frac{\partial p}{\partial e} + \rho\right)\frac{u}{\rho} \end{bmatrix} \tag{D.4}$$

and the eigenvalues $\lambda_1, \lambda_2, \lambda_3$ are:

$$\lambda_1 = u - \sqrt{\frac{\partial p}{\partial \rho} + \frac{\partial p}{\partial e}\frac{p}{\rho^2}}, \tag{D.5}$$

$$\lambda_2 = u, \tag{D.6}$$

$$\lambda_3 = u + \sqrt{\frac{\partial p}{\partial \rho} + \frac{\partial p}{\partial e}\frac{p}{\rho^2}}. \tag{D.7}$$

The solution of the Euler Equations (Eqs. D.1) is self-similar, with two genuinely nonlinear waves (corresponding to eigenvalues λ_1 and λ_3), which can be either shock waves or rarefaction waves (Fig. D.1).

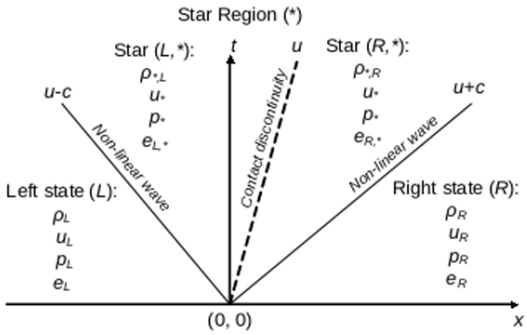

Figure D.1: Wave structure of the Riemann problem for the Euler equations for a general equation of state $p = f(\rho, e)$.

These waves separate the solution of the Riemann problem into the left state (L), the right state (R), and the star region ($*$). In the star region,

pressure and velocity are the same, but density and internal energy are not. In particular, the internal energy also changes along the contact discontinuity (corresponding to λ_2).

To find the solution to the Riemann problem, one needs to solve a nonlinear algebraic equation for the pressure (Eq. D.8).

$$g(p^*) = g_L(p^*) + g_R(p^*) + u_R - u_L = 0. \tag{D.8}$$

Functions g_L and g_R depend on the type of nonlinear wave. For shock waves the Rankine–Hugoniot conditions are employed, eventually leading to:

$$g_{K,\text{shock}} = \frac{(p^* - p_K)(\rho_K^* - \rho_K)}{\rho_K^* \rho_K}, \qquad K = L \text{ or } K = R. \tag{D.9}$$

Apart from Eq. D.9, energy conservation applies across the shock wave, as shown in Eq. D.10

$$e_K^* = \frac{1}{2}(p^* + p_K)\frac{\rho_K^* - \rho_K}{\rho_K^* \rho_K} + e_K. \tag{D.10}$$

To solve Eqs. D.9 and D.10 an iterative procedure is required. Initially, one assumes an internal energy e_K^* (e.g. equal to e_K) which, combined with pressure p^*, corresponds to a density ρ_K^*. This density can be used to obtain the $g_{K,\text{shock}}$ function and the internal energy from the energy balance (Eq. D.10). Since e_K^* from Eq.D.10 and the guessed e_K^* are not necessarily the same, the guessed value got e_K^* is corrected, and the process is repeated until convergence.

For the rarefaction wave, the calculation is more complicated, since it involves the Riemann invariants across an isentropic path. The Riemann invariants are shown below for the left rarefaction wave:

$$du + \frac{c}{\rho} d\rho = 0, \qquad s = s_L \tag{D.11}$$

and the right rarefaction wave:

$$du - \frac{c}{\rho} d\rho = 0, \qquad s = s_R \tag{D.12}$$

Integration of these relations is not convenient to be done analytically for a general EoS (which might be expressed in tabular form). It is rather convenient to perform the integration numerically on an isentropic path across the rarefaction wave, as follows (e.g. for the left rarefaction wave):

$$u^* - u_L + \int_L^* \frac{c}{\rho}\Big|_{s=s_L} d\rho = 0 \tag{D.13}$$

One can split the integral as follows:

$$u^* + \int_{ref}^* \frac{c}{\rho}\Big|_{s=s_L} d\rho = u_L + \int_{ref}^L \frac{c}{\rho}\Big|_{s=s_L} d\rho, \tag{D.14}$$

where ρ_{ref} is a reference state (e.g. at the minimum allowable density of the EoS).

Similarly, one may derive the relation for the right rarefaction wave:

$$u^* - \int_{ref}^* \frac{c}{\rho}\Big|_{s=s_R} d\rho = u_L - \int_{ref}^R \frac{c}{\rho}\Big|_{s=s_R} d\rho, \tag{D.15}$$

and eventually the function

$$g_{K\cdot rarefaction} = \int_{ref}^* \frac{c}{\rho}\Big|_{s=s_K} d\rho - \int_{ref}^K \frac{c}{\rho}\Big|_{s=s_R} d\rho \tag{D.16}$$

From this point onwards, the integral $\int_{ref}^K \frac{c}{\rho}\Big|_{s=s_R} d\rho$ will be referred to as $I_K(p_K)$.

Calculation of the isentropic integral $I_K(p_K)$ may be performed numerically. First, the states that have the same entropy s as the right (R) and left (L) states need to be determined. Assuming that the thermodynamic properties are expressed in the form $f(\rho, e)$, the isentropic path can be calculated as follows:

1. Determine the entropy of the K state (K can be either L or R) as

$s_K = s(\rho_K, e_K)$.

2. Starting from a low reference density ρ_{ref}, and increasing it by intervals $\Delta\rho$, find the point that corresponds to s_K by iteratively correcting the internal energy e for the given path point i. Internal energy correction can be performed with the Newton–Raphson method until a specified tolerance is reached.

3. After convergence, compute the remaining thermodynamic properties (e.g., pressure, speed of sound) for (ρ_i, e_i). The speed of sound c is needed to evaluate the term inside the integral I_K, while the pressure p is required to express the integral as a function of pressure (preferable, since pressure in the whole star region is uniform).

4. Evaluate the integral using the trapezoid rule, or a more accurate Simpson method. Care must be taken in regions with large variations in the speed of sound, such as near saturation lines.

5. Extend the procedure up to a sufficiently high pressure $p_{\max}$, which should be greater than the pressure expected in the subsequent calculations.

Switching between rarefaction and shock waves is done based on pressure, as shown in Eq. D.17.

$$g_K = \begin{cases} g_{K,\text{rarefaction}} & p_K < p^*, \\ g_{K,\text{shock}} & p_K \geq p^*. \end{cases} \tag{D.17}$$

The solution for the star region can be achieved with the Newton–Raphson method, as described in Eq. D.18.

$$p^{(n)} = p^{(n-1)} - \frac{g(p^{(n-1)})}{g'(p^{(n-1)})}\, urf, \tag{D.18}$$

where n is the iteration index, urf is an under-relaxation factor to enhance stability in case of highly nonlinear EoS, and g' is the derivative of Eq.D.8.

For such equations, it is preferable to resort to a numerically approximated value of the derivative, as shown in Eq. D.19.

$$g' = \frac{g(\rho - \varepsilon) - g(p)}{\varepsilon}, \tag{D.19}$$

with ε a small positive number.

To prevent overshoots/undershoots, one may also bound the maximum change of pressure from iteration to iteration, as expressed in Eq. D.20.

$$p^{(n)} = \max\Big(\min(p^{(n)}, p_{\max}),\, p_{\min}\Big), \tag{D.20}$$

where $p_{\max}, p_{\min}$ can be chosen as percenlabeles of $p^{(n-1)}$ (e.g. 120% and 80% respectively).

After convergence of p^*, the velocity u^* is obtained as in Eq. D.21.

$$u^* = \tfrac{1}{2}(u_L + u_R) + \tfrac{1}{2}\big[g_R(p^*) - g_L(p^*)\big]. \tag{D.21}$$

Identification of the type of wave is based on the star-region pressure compared with the left/right states:

- if $p^* > p_K$ then the wave between $*$ and K is a shock wave;
- otherwise, it is a rarefaction wave

The type of wave determines the wave speed and the transition between the two states. For a shock wave the transition is sharp and the wave speed is given by:

$$S_L = u_L - \tfrac{Q_L}{\rho_L}, \tag{D.22}$$

$$S_R = u_R + \tfrac{Q_L}{\rho_L} \tag{D.23}$$

with

$$Q_K = \sqrt{\frac{(p^* - p_K)\rho_K \rho^*}{\rho_K - \rho^*}}. \tag{D.24}$$

Rarefactions, contrary to shock, are gradual changes in density, pressure and velocity. Thus, they are associated with two speeds, one for the head of

the rarefaction and one for the tail:

$$S_{LH} = u_L - c_L, \qquad S_{LT} = u^* - c_L, \tag{D.25}$$

$$S_{RH} = u_R + c_R, \qquad S_{RT} = u^* + c_R. \tag{D.26}$$

In order to find the conditions inside the rarefaction wave, the Riemann invariants shall be used. Inside the rarefaction wave, Riemann invariants apply. For a left rarefaction:

$$\frac{x_i}{t} + c(p_i) + I_L(p_i) = u_L + I_L(p_L), \tag{D.27}$$

and for the right rarefaction:

$$\frac{x_i}{t} - c(p_i) - I_R(p_i) = u_R - I_R(p_R). \tag{D.28}$$

These equations are typically solved numerically for density, using Newton–Raphson with under-relaxation. Experience has shown that it is better to apply a low under-relaxation factor of even 0.02.

Publications

The following scientific publications were produced as a result of the conducted research activities during this PhD project:

Raffaele Bellini, Carlos Rodriguez, Ioannis K. Karathanassis, and Manolis Gavaises. Cavitation dynamics and surface erosion in fuel injectors considering the composition of fuel mixtures. *Computer and Fluids*, 301(106793), 2025.

Raffaele Bellini, Carlos Rodriguez, Ioannis K. Karathanassis, Manolis Gavaises, and Evangelos Geber. Modelling of wall-bounded cavitating flow and spray mixing in multi-component environments using the pc-saft equation of state. *Applications in Energy and Combustion Science*, 20(10), 2024.

Raffaele Bellini, Carlos Rodriguez, Ioannis K. Karathanassis, and Manolis Gavaises. Collapse of cavitation bubble clusters of fuels utilised with modern combustion systems. *ILASS Europe 2023, 31st European Conference on Liquid Atomization & Spray Systems, 4-7 Sept 2023, Napoli, Italy*, 2023.

Bibliography

Aleiferis, P. G., Serras-Pereira, J., Augoye, A., Davies, T. J., Cracknell, R. F. and Richardson, D. [2010], 'Effect of fuel temperature on in-nozzle cavitation and spray formation of liquid hydrocarbons and alcohols from a real-size optical injector for direct-injection spark-ignition engine', *Int. J. Heat Mass Transf* **53**, pp. 4588–4606.

Anitescu, G., Bruno, T. and Tavlarides, L. [2012], 'Dieseline for supercritical injection and combustion in compression-ignition engines: volatility, phase transitions, spray/ jet structure, and thermal stability', *Energy Fuels* **6247-58**.

Anon. [2015], 'Senate regulation 25: Physical format, binding and retention of theses', **url**: www.city.ac.uk/about/city-information/governance/constitution/senate-regulations.

Arai, Y., Sako, T. and Takebayashi, Y. [2002], 'Material processing using supercritical fluids.', *Supercritical Fluids: Molecular Interactions, Physical Properties, and New Applications.* pp. 281–345.

Arcoumanis, C., Gavaises, M. and French, B. [1997], 'Effect of fuel injection processes on the structure of diesel sprays.', *SAE Transactions* pp. 1025–1064.

Arndt, M. C. and Sadowski, G. [1994], *Biochemical and Chemical Engineering.*, 2^{nd} edn, Addison-Wesley, Reading, MA.

Arndt, R. [1981], 'Cavitation in fluid machinery and hydraulic structures', *Annual Review of Fluid Mechanics* **13**, pp. 273–326.

Arndt, R. [2002], 'Cavitation in vortical flows', *Annual Review of Fluid Mechanics* **34**, pp. 143–175.

Balz, R. e. a. [2021], 'Experimental and numerical investigation of cavitation in marine diesel injectors.', *International Journal of Heat and Mass Transfer* .

Bamgbade, B. e. a. [2015], 'High-temperature, high-pressure volumetric properties of propane, squalane, and their mixtures: measurement and pc-saft modeling', *Ind Eng Chem Res* **56(26)**, 6804–6811.

Baran, O. e. A. [2023], 'Assessment of injector-flow characteristics of additised and renewable diesel blends through high-speed imaging', *Fuel* **352:129076**.

Battistoni, M. and Grimaldi, C. [2012], 'Numerical analysis of injector flow and spray characteristics from diesel injectors using fossil and biodiesel fuels', *Applied Energy* **97**, pp. 656–666.

Battistoni, M., Som, S. and Powell, C. [2019], 'Highly resolved eulerian simulations of fuel spray transients in single and multi-hole injectors: nozzle flow and near-exit dynamics', *Fuel* **251**, 709–729.

Beattie, D. and Whalley, P. [1982], 'Simple two-phase frictional pressure drop calculation method. int j multiphase flow', *Phys Rev A* **8(1)**.

Berger, M. J. and Colella, P. [1989], 'Local adaptive mesh refinement for shock hydrodynamics', *Journal of Computational Physics* **82**(1), 64–84.

Bergwerk, W. [1959], 'Flow pattern in diesel nozzle spray holes', *Proceeding, Institute of Mechanical Engineering* **173**, pp. 655–660.

Besant, W. [1859], *Hydrostatics and Hydrodynamics*, Cambridge University Press.

Bohbot, J., Miche, M. and Melgar, C. [2009], 'Modelling of the cavitation phenomenon in the high pressure diesel injection system', *Thermo-and Fluid Dynamic Processes in Diesel Engines* **2**.

Brennen, C. [1994], *Hydrodynamics of Pumps*, Concepts ETI Inc.

Brennen, C. [2005], *Fundamentals of Multiphase Flows*, Cambridge University Press.

Brennen, C. [2013], *Cavitation and bubble dynamics*, Cambridge University Press.

Burgess, W., Tapriyal, D., Gamwo, I., Wu, Y. and McHugh, M. [2014], 'New group-contribution parameters for the calculation of pc-saft parameters for use at pressures to 276 mpa and temperatures to 533 k', *Ind. Eng. Chem. Res.* **53(6)**, 2520–2528.

Butcher, A. [2020], Spray Formation and Cavitation of Fuel Injectors with Various Metal and Optical Nozzles, PhD dissertation, University College London.

Cao, J. e. a. [2020], 'Dynamics of vortex-induced string cavitation in fuel injector nozzles', *International Journal of Multiphase Flow* .

Cervone, A., S., M. and Scardovelli, R. [2010], 'Simulation of axisymmetric jets with a finite element navier–stokes solver and a multilevel vof approach', *Journal of Computational Physics* **229**, 6853–6873.

Chapman, W., Gubbins, K., Jackson, G. and Radosz, M. [1990], 'New reference equation of state for associating liquids', *Ind Eng Chem Res* **29(8)**, 1709–1721.

Chaves, H., Knapp, M., Kubutzek, A., Obermeier, F. and Schneider, T. [1995], 'Experimental study of cavitation in the nozzle hole of diesel injectors using transparent nozzles', *SAE Paper 950290* **24**, pp. 645–657.

Climate Watch - the World Research Institute [2022], https://ourworldindata.org/emissions-by-sector#sector-by-sector-where-do-global-greenhouse-gas-emissions-come-from. Accessed: 01.09.2022.

Cristofaro, M., Edelbauer, W., Koukouvinis, P. and Gavaises, M. [2018], 'Large eddies simulation of the injector internal flow during a pilot injection', *Proceedings of the 10th International Symposium on Cavitation (CAV2018)* pp. 1025–1064.

Crua, C., Manin, J. and Pickett, L. [2017], 'On the transcritical mixing of fuels at diesel engine conditions', *Fuel* **208**, 535–548.

Dahms, R. and Oefelein, J. [2015], 'Liquid jet breakup regimes at supercritical pressures', *Combust Flame* **162(10)**, 3648–3657.

Deng, F., Zhao, D., Zhang, L. and Shao, X. [2024], 'Numerical study of the kinematic and acoustic characteristics of bubble clusters', *Journal of Hydrodynamics* **35**(1), 61–75.

Devassy, B., Edelbauer, W. and Greif, D. [2015], 'Numerical simulation of the effect of 3d needle movement on cavitation and spray formation in a diesel injector.', *Journal of Physics: Conference Series* **12092**.

Dular, M., Bachert, B., Stoffel, B. and Sirok, B. [2004], 'Relationship between cavitation structures and cavitation damage.', *Wear* **257(11)**, 1176–1184.

Dular, M. and Petkovsek, M. [2018], 'Cavitation erosion in liquid nitrogen', *Wear* **400-401**, pp. 111–118.

Dumbser, M., Iben, U. and Munz, C. D. [2013], 'Efficient implementation of high order unstructured weno schemes for cavitating flows', *Energy & Fuels* **86**, 141–168.

EDEM Projet [2019], https://edem-itn.eu/. Accessed: 01.05.2022.

Endo, K., Okada, T. and Baba, Y. [1969], 'Fundamental studies on cavitation erosion', *Bulletin of JSME* **12**, pp. 729–737.

Engine Combustion Network [2022], https://ecn.sandia.gov/. Accessed: 01.04.2022.

Espinoza, D., Scanlon, T. and Brown, R. [2015], 'Validation of tools to accelerate high-speed cfd simulations using openfoam', *20th AIAA International Space Planes and Hypersonic Systems and Technologies Conference* pp. 1–18.

E.W., L. and Hube, M. L. [2004], 'Thermodynamic properties of n-dodecane', *Energy & Fuels* **18**, 960–967.

ExxonMobil [2023], *2023 Outlook for Energy*, Technical Report - ExxonMobil.

Falgout, Z., Rahm, M., Sedarsky, D. and Linne, M. [2016], 'Gas/fuel jet interfaces under high pressures and temperatures', *Int J Multiphase Flow* **168**, 14–21.

Fang, T. e. a. [2023], 'X-ray visualization of internal flow and hydraulic flip in gdi injectors.', *Fuel* .

Fathi, M. and Hickel, S. [2021], 'Rapid multi-component phase-split calculations using volume functions and reduction methods', *AIChE* **67(6)**, 1–30.

Fathi, M., Hickel, S. and Roekaerts, D. [2022], 'Large eddy simulations of reacting and non-reacting transcritical fuel sprays using multiphase thermodynamics', *Fuel* **34(8)**.

Ferrari, A. [2017], 'Fluid dynamics of acoustic and hydrodynamic cavitation in hydraulic power system', *Proceeding A, Royal Society* **473**, 0160345.

Fletcher, R. [2013], 'Practical methods of optimization', *John Wiley & Sons* **320**, 1–9.

Franc, J. [2009], 'Incubation time and cavitation erosion rate of work-hardening materials', *Journal of Fluids Engineering* **131**, pp. 021303–1–14.

Franc, J., Chahine, G., Riondet, M. and Karimi, A. [2011], 'Impact load measurements in an erosive cavitating flow', *Journal of Fluids Engineering* **133**, pp. 121–301.

Franc, J. and Michel, J. [1985], 'Attached cavitation and the boundary layer: experimental investigation and numerical treatment', *Journal of Fluid Mechanics* **154**, pp. 63–90.

Franc, J. and Michel, J. [2005], *Fundamentals of Cavitation*, Kluwer Academi Publishers.

Ganser, M. [2000], 'Common rail injectors for 2000 bar and beyond', *Journal of Computational Physics* **01-0760**, 6853–6873.

Gavaises, M., Murali-Girija, M., Rodriguez, C., Koukouvinis, P., Gold, M. and Pearson, R. [2022], 'Numerical simulation of fuel dribbling and nozzle wall wetting.', *Int J Engine Res* **23(1)**, 132–149.

Geber, E., Rodriguez, C., Vidal, A., Koukouvinis, P. and Gavaises, M. [2023], 'A general predictive methodology for fuel-mixture properties up to supercritical conditions', *Fluid Phase Equilib* **574**.

Ghahramani, E., Arabnejad, M. H. and Bensow, R. E. [2019], 'A comparative study between numerical methods in simulation of cavitating bubbles', *International Journal of Multiphase Flow* **111**, pp. 339–359.

Ghosn, L., Villedieu, N., Menard, T. and Berlemont, A. [2018], 'Assessment of amr strategies for the simulation of liquid jet atomization', *Proceedings of the 14th Triennial International Conference on Liquid Atomization and Spray Systems (ICLASS)* .

Giannadakis, E. [2005], Modelling of Cavitation in Automotive Fuel Injector Nozzles, PhD dissertation, Imperial College, University of London.

Giannadakis, E., Gavaises, M. and Arcoumanis, C. [2008], 'Modelling of cavitation in diesel injector nozzles', *J. Fluid Mech.* **616**, pp. 153–193.

Gilmore, F. [1952], 'The growth and collapse of a spherical bubble in a viscous compressible liquid', *Caltech Institute of Technology, Hydrodynamics Laboratory, Report* **26-4**.

Goncalves, E., Champagnac, M. and Fortes-Patella, R. [2010], 'Comparison of numerical solvers for cavitating flows', *Int. J. Comput. Fluid Dyn.* **24**, pp. 201–216.

Gorokhovski, M. and Herrmann, M. [2008], 'Modeling primary atomization', *Annual Review of Fluid Mechanics* **40**, 343–366.

Greenshields, C., Weller, H., Gasparini, L. and Reese, J. [2009], 'Implementation of semi-discrete, non-staggered central schemes in a colocated, polyhedral, finite volume framework, for high-speed viscous flows', *Int J Numer Methods Fluids* **38(2)**.

Gross, J. and Sadowski, G. [2001], 'Perturbed-chain saft: an equation of state based on a perturbation theory for chain molecules', *Ind Eng Chem Res* **40(4)**, 1244–1260.

Gross, J. and Sadowski, G. [2002], 'Application of the perturbed-chain saft equation of state to associating systems.', *Ind Eng Chem Res* **41(22)**.

Guo, H. e. A. [2020], 'Internal nozzle flow simulations of the ecn spray c injector under realistic operating conditions', *SAE Technical Papers* **4**, 1–12.

Han, Z., Uludogan, A., Hampson, G. and Reitz, R. [1996], 'Mechanism of soot and nox emission reduction using multiple-injection in a diesel engine', *SAE Transaction* pp. 837–852.

Harvey, A. and Lemmon, E. [2004], 'Correlation for the second virial coefficient of water', *J Phys Chem Ref Data* **33(1)**, 369–376.

Hattori, S., Hirose, T. and Sugiyama, K. [2010], 'Prediction method for cavitation erosion based on measurement of bubble collapse impact loads', *Wear* **269**, pp. 507–514.

Hattori, S. and Nakao, E. [2001], 'Cavitation damage measurement by 3d laser profilometry', *Wear* **249**, pp. 839,845.

Hawi, M., Kosaka, H., Sato, S., Nagasawa, T., Elwardany, A. and Ahmed, M. [2019], 'Effect of injection pressure and ambient density on spray characteristics of diesel and biodiesel surrogate fuels.', *Fuel* **254:115674**.

He, Z., Guo, G., Tao, X., Zhong, W., Leng, X. and Wang, Q. [2016], 'Study of the effect of nozzle hole shape on internal flow and spray characteristics', *International Communications Heat Mass Trans* **71**, pp. 1–8.

He, Z., Zhong, W., Wang, Q., Jiang, Z. and Shao, Z. [2013], 'Effect of nozzle geometrical and dynamic factors on cavitating and turbulent flow in a diesel multi-hole injector nozzle', *International Journal of Thermal Sciences* **70**, pp. 132–143.

Hopp, M. and Gross, J. [2017], 'Thermal conductivity of real substances from excess entropy scaling using pc-saft', *Ind Eng Chem Res* **56(15)**, 4527–4538.

Huang, B., Ducoin, A. and Young, Y. [2013], 'Physical and numerical investigation of cavitating flows around a pitching hydrofoil', *Phys. Fluids* **25(10)**.

Huang, S. and Radosz, M. [1990], 'Equation of state for small, large, polydisperse, and associating molecules', *Ind Eng Chem Res* **29(11)**, 2284–2294.

Huang, S. and Radosz, M. [1991], 'Equation of state for small, large, polydisperse, and associating molecules: extension to fluid mixtures', *Ind Eng Chem Res* **30(8)**, 1994–2005.

IPCC [2022], *Climate Change 2022 - Mitigation of Climate Change*, WMO - UNEP.

Jayaprakash, A., Choi, J., Franc, J., Chahine, G., Martin, F., Donelly, M. and Karimi, A. [2012], 'Scaling study of cavitation pitting from cavitating jets and ultrasonic horns', *Wear* **296**, pp. 619–629.

Jiang, G., Zhang, Y., Wen, H. and Xian, G. [2015], 'Study of the generated density of cavitation inside diesel nozzle using different fuels and nozzles', *Energy Conversion and Management* **103**, pp. 208–217.

Karathanassis, I. e. A. [2021], 'X-ray phase contrast and absorption imaging for the quantification of transient cavitation in high-speed nozzle flows', *Phys Fluids* **33(3)**.

Karathanassis, I., Trickett, K., Koukouvinis, P., Wang, J., Barbour, R. and Gavaises, M. [2018], 'Illustrating the effect of viscoelastic additives on cavitation and turbulence with x-ray imaging', *Sci Rep* **8(1)**, 149–168.

Karimi, M., Wang, X., Hamilton, J., Negnevitsky, M. and Lyden, S. [2021], 'Status, challenges and opportunities of dual fuel hybrid approaches-a review', *International Journal of Hydrogen Energy* **70**, 34924–34957.

Keller, J. and Miksis, M. [1980], 'Bubble oscillations of large amplitude', *journal of the Acoustical Society of America* **68**(2), 628–633.

Kim, K., Chahine, G., Franc, J. and Karimi, A. [2014], *Advanced Experimental and Numerical Techniques for Cavitation Erosion Prediction*, Springer.

Kook, S. and Pickett, L. [2012], 'Liquid length and vapor penetration of conventional, fischer–tropsch, coal-derived, and surrogate fuel sprays at high-temperature and high-pressure ambient conditions.', *Fuel* **93**, 539–548.

Koukouvinis, P., Gavaises, M., Georgoulas, A. and Marengo, M. [2016], 'Compressible simulations of bubble dynamics with central-upwind schemes', *International Journal of Computational Fluid Dynamics* **30**, pp. 129–140.

Koukouvinis, P., Gavaises, M., Li, J. and Wang, L. [2016], 'Large eddy simulation of diesel injector including cavitation effects and correlation to erosion damage', *Fuel* **175**, pp. 26–39.

Koukouvinis, P., Gavaises, M., Supponen, O. and Farhat, M. [2016], 'Numerical simulation of a collapsing bubble subject to gravity', *Phys. Fluids* **28**.

Koukouvinis, P., Vidal, A., Rodriguez, C., Gavaises, M. and Pickett, L. [2020], 'High pressure/high temperature multiphase simulations of dodecane injection to nitrogen: application on ecn spray-a', *Fuel* **275:117871**.

Kubota, A., Kato, H. and Yamaguchi, H. [1992], 'A new modelling of cavitating flows: a numerical study of unsteady cavitation on a hydrofoil section', *Journal of Fluid Mechanics* **240**, 59–96.

Kyriazis, N., Koukouvinis, P. and Gavaises, M. [2017], 'Numerical investigation of bubble dynamics using tabulated data', *International Journal of Multiphase Flow* **93**, pp. 158–177.

Kyriazis, N., Koukouvinis, P. and Gavaises, M. [2019], 'Numerical investigations on bubble-induced jetting and shock wave focusing: Application on a needle-free injection', *Proc. R. Soc. A Math. Phys. Eng. Sci* **475**, 2222.

Lacaze, G. and Misdariis A, Ruiz A, O. J. [2015], 'Analysis of high-pressure diesel fuel injection processes using les with real-fluid thermodynamics and transport', *Proc. Combust. Inst.* **35(2)**, 1603–1611.

Lamport, L. [1994], *Latex, A document preparation system*, 2^{nd} edn, Addison-Wesley, Reading, MA.

Lauer, E., Hu, X. Y., Hickel, S. and Adams, N. A. [2012], 'Numerical modeling and investigation of symmetric and asymmetric cavitation bubble dynamics', *Computational Fluids* **69**, pp. 1–19.

Lauterborn, W. and Ohl, C. [1998], 'The peculiar dynamics of cavitation bubbles', *Applied Scientific Research* **58**, pp. 63–76.

Le Métayer, O., Massoni, J. and Saurel, R. [2005], 'Modelling evaporation fronts with reactive riemann solvers', *Journal of Computational Physics* **205**, 567–610.

Leekumjorn, S. and Krejbjerg, K. [2013], 'Phase behavior of reservoir fluids: comparisons of pc- saft and cubic eos simulations', *Fluid Phase Equilib* **359**, 17–23.

Lemaire, R., Faccinetto, A., Therssen, E., Ziskind, M., Focsa, C. and Desgroux, P. [2009], 'Experimental comparison of soot formation in turbulent flames of diesel and surrogate diesel fuels.', *Proc. Combust. Inst.* **32(1)**, 737–44.

Lemmon, E., Huber, M. and McLinden, M. [2013], *NIST Standard Reference Database 23: Reference Fluid Thermodynamic and Transport Properties*, refprop, version 9.1 edn, National Institute of Standards and Technology.

LeVeque, R. [2004], *Finite Volume Methods for Hyperbolic Problems*, Cambridge University Press.

Li, Y., Ries, F., Sun, Y., Lien, H., Nishad, K. and Sadiki, A. [2024], 'Direct numerical simulation of atomization characteristics of ecn spray-g injector: In-nozzle fluid flow and breakup processes', *Flow, Turbulence and Combustion* **112**, 615–642.

Liang, X., Maribo-Mogensen, B., Thomsen, K., Yan, W. and Kontogeorgis, G. [2012], 'Approach to improve speed of sound calculation within pc-saft framework', *Ind Eng Chem Res* **51(45)**, 14903–14914.

Lin, R. [2011], Issues on Clean Diesel Combustion Technology Using Supercritical Fluids: Thermophysical Properties and Thermal Stability of Diesel Fuel., PhD dissertation, Syracuse University.

Lin, R. and Tavlarides, L. [2012], 'Thermophysical properties needed for the development of the supercritical diesel combustion technology: evaluation of diesel fuel surrogate models.', *Journal of Supercritical Fluids* **08-003**.

Lindau, O. and Lauterborn, W. [2003], 'Cinematographic observation of the collapse and rebound of a laser-produced cavitation bubble near a wall', *Journal of Fluid Mechanics* **479**, pp. 327–348.

Liu, F. [2016], 'Fuel nozzle geometry effects on cavitation and spray behavior at diesel engine conditions.', *Proceedings of CFD with OpenSource Software* **34**.

Liu, X., Guo, H. and Im, H. [2024], 'Development of correlation model for cavitating spray using eulerian simulations.', *Internatoinal Journal of Engine Research* **25**.

Lotgering-Lin, O. and Gross, J. [2015], 'Group contribution method for viscosities based on entropy scaling using the perturbed-chain polar statistical associating fluid theory', *Ind Eng Chem Res* **54(32)**, 7942–7952.

Ma, P., Wu, H., Banuti, D. and Ihme, M. [2019], 'On the numerical behavior of diffuse-interface methods for transcritical real-fluids simulations', *Int J Multiphase Flow* **231-249**.

Magnotti, G. and Som, S. [2022], 'Experimental investigation of cavitation-induced erosion using x-ray imaging.', *Frontiers in Mechanical Engineering* .

Mamaikin, D., Knorsch, T., Rogler, P., Wang, J. and Wensing, M. [2021], 'The effect of transient needle lift on the internal flow and near-nozzle spray characteristics for modern gdi systems investigated by high-speed x-ray imaging.', *International Journal of Engine Research* **23(2)**, 226–229.

Manin, J., Pickett, L. and Yasutomi, K. [2020], 'Stereoscopic high-speed microscopy to understand transient internal flow processes in high-pressure nozzles', *Exp Therm Fluid Sci* **114**.

Martynov, S. [2005], Numerical Simulation of the Cavitation Process in Diesel Fuel Injectors, PhD dissertation, University of Brighton.

Matheis, J. and Hickel, S. [2017], 'Multi-component vapor-liquid equilibrium model for les of high-pressure fuel injection and application to ecn spray a', *International Journal of Multiphase Flow* **000**, pp. 1–18.

Menikoff, R. and Plohr, B. J. [1989], 'The riemann problem for fluid flow of real materials', *Rev. Mod. Phys* **61**, 75–130.

Michelsen, L. [1982*a*], 'The isothermal flash problem. part i. stability', *Fluid Phase Equilib* **9(1)**, 1–19.

Michelsen, L. [1982*b*], 'The isothermal flash problem. part ii. phase-split calculation', *Fluid Phase Equilib* .

Michelsen, L. and Mollerup, J. [2007], 'Thermodynamic models : Fundamentals & computational aspects', *Tie-Line Publications* .

Mihatsch, M. [2016], Numerical Prediction of Erosion and Degassing Effects in Cavitating Flows, PhD dissertation, Technische Universitat Munchen.

Mikyska, J. and Firoozabadi, A. [2012], 'Investigation of mixture stability at given volume, temperature, and number of moles', *Fluid Phase Equilib.* **320**, 1–9.

Mithun, M., Koukouvinis, P. and Gavaises, M. [2018], 'Numerical simulation of cavitation and atomization using a fully compressible three-phase model', *Physical Review Fluids* .

Mitroglou, N., Lorenzi, M., Santini, M. and Gavaises, M. [2016], 'Application of x-ray micro- computed tomography on high-speed cavitating diesel fuel flows', *Exp Fluids* **57**, 1–14.

Mohamed, M., Hameed, H., ElShenawy, E., Abdel, H., El-Salmawy, A. and Shaltout, R. [2021], 'Numerical simulation and experimental study for the impact of in-flow nozzle on spray characteristics', *ACS Omega* **6**.

Moon, C., Magnotti, G., Sforzo, B., Tekawade, A., Kastengren, A. and Powell, C. [2022], 'Experimental investigation of cavitation-induced erosion using x-ray imaging and tomography', *Front. Mech. Eng* **8**.

Mueller, C. and et al. [2016], 'Diesel surrogate fuels for engine testing and chemical-kinetic modeling: compositions and properties', *Energy & Fuels* **30(2)**, 1445–1461.

Muller, S. and Voss, A. [2006], 'The riemann problem for the euler equations with nonconvex and nonsmooth equation of state: Construction of wave curves', *SIAM Journal on Scientific Computing* **28(2)**, 651–681.

Nicoud, F. and Ducros, F. [1999], 'Subgrid-scale stress modelling based on the square of the velocity gradient tensor', *Flow Turbul Combust* **62(3)**, 183–200.

Nishida, K., Zhu, J., Leng, X. and He, Z. [2017], 'Effects of micro-hole nozzle and ultra-high injection pressure on air entrainment, liquid penetration, flame lift-off and soot formation of diesel spray flame.', *International Journal of Engine Research* **18(1-2)**, 51–63.

NIST Refprop Database [2022], https://www.nist.gov/srd/refprop. Accessed: 01.05.2021.

Nocedal, J. and Wright, S. [2006], 'Numerical optimization 2nd edition', *Springer* **2nd**.

Ogloblina, D., Schmidt, S. and Adams, N. [2018], 'Simulation and analysis of collapsing vapor-bubble clusters with special emphasis on potentially erosive impact loads at walls', *EPJ Web of Conferences* **18**, pp. 02079.

Okada, T., Iwai, Y., Ishimaru, H. and Maekawa, N. [1994], 'Measurement and evaluation of cavitation bubble collapse pressures', *JSME international journal. Ser. A, Mechanics and material engineering* **37**, pp. 37–42.

Onorati, A. e. a. [2022], 'The role of hydrogen for future internal combustion engines', *SAGE Publications Sage UK: London, England* .

OpenCFD Ltd [2022], https://www.openfoam.com/. Accessed: 01.08.2022.

Orley, F., Pasquariello, V., Hickel, S. and Adams, N. [2015], 'Cut-element-based immersed boundary method for moving geometries in compressible liquid flows with cavitation.', *Journal of Comput Phys: Conference Series* **283**, 1–22.

Patel, N. and Bambhania, M. P. [2023], 'Hydrodynamic cavitation in the fuel injector nozzle and its effect on spray characteristics: A review', *Heat and Mass Transfer Research* **19**, 1–20.

Patella, R., Reboud, J. and Archer, A. [2000], 'Cavitation damage measurement by 3d laser profilometry', *Wear* **246**, pp. 59–67.

Payri, F., Arrègle, J. and López, J.and Hermens, S. [2006], 'Effect of cavitation on the nozzle outlet flow, spray and flame formation in a diesel engine,', *SAE Technical Paper* **01-1391**.

Payri, F., Bermúdez, V., Payri, R. and Salvador, F. [2004], 'The influence of cavitation on the internal flow and the spray characteristics in diesel injection nozzles', *Fuel* **83**, pp. 419–431.

Perera, S. [2025], 'Direct visualization of cavitation erosion near the needle seat area on real-size diesel fuel injectors.', *Journal of Mineral Science and Materials.* .

Petitpas, F., Massoni, J., Saurel, R., Lapebie, E. and Munier, L. [2009], 'Di use interface model for high speed cavitating underwater systems', *International Journal of Multiphase Flow* **35(8)**, 651–681.

Philipp, A. and Lauterborn, W. [1998], 'Cavitation erosion by single laser-produced bubbles', *Journal of Fluid Mechanics* **361**, pp. 75–116.

Philipp, A. and Lauterborn, W. [2000], 'Cavitation erosion by single laser-produced bubbles', *Journal of Fluid Mechanics* **361**, pp. 75–116.

Pickett, L., Manin, J., Genzale, C., Siebers, D., Musculus, M. and Idicheria, C. [2011], 'Relationship between diesel fuel spray vapor penetration/dispersion and local fuel mixture fraction', *SAE Int. J. Engines* **4**, pp. 764–799.

Pickett, L. and Siebers, D. [2004], 'Soot in diesel fuel jets: effects of ambient temperature, ambient density, and injection pressure.', *Combust Flame* **138(1-2)**, 114–135.

Piehl, J. and Bravo, L. [2018], *Assessment of Cavitation Models for Computational Fluid Dynamics Analysis of Erosion Risk in a Hydrocarbon-Fueled Nozzle*, Technical Report - US Army Research Laboratory.

Plesset, M. and Chapman, R. [1970], 'Collapse of an initially spherical vapour cavity in the neighbourhood of a solid boundary', *Journal of Fluid Mechanics* **47**, pp. 283–290.

Pope, S. B. [2000], *Turbulent Flows*, 2^{nd} edn, Cambridge University Press.

Qiu, L. and Reitz, R. [2015], 'An investigation of thermodynamic states during high-pressure fuel injection using equilibrium thermodynamics.', *Int J Multiphase Flow* **72**, 24–38.

Rayleigh, B. [1917], 'On the pressure developed in a liquid during the collapse of a spherical cavity', *Phil. Mag.* **34**, pp. 94–97.

Reitz, R. e. a. [2020], 'Ijer editorial: the future of the internal combustion engine', *SAGE Publications Sage UK: London, England* .

Ripple, W. J. [2020], 'World scientists' warning of a climate emergency', *BioScience* **70**(1), pp. 8–12.

Ripple, W. J. [2021], 'World scientists' warning of a climate emergency 2021', *BioScience* **71**(9), pp. 894–989.

Rodriguez, C., Koukouvinis, P. and Gavaises, M. [2019], 'Simulation of supercritical diesel jets using the pc-saft eos', *Jounral of Supercrit Fluids* **145**, 48–65.

Rodriguez, C., Rokni, H., Koukouvinis, P., Gupta, A. and Gavaises, M. [2019], 'Complex multi-component real-fluid thermodynamic model for high-pressure diesel fuel injection', *Fuel* **257:115888**.

Rodriguez, C., Vidal, A., Koukouvinis, P., Gavaises, M. and McHugh, M. [2021], 'Simulation of transcritical fluid jets using the pc-saft eos', *J Comput Phys* **374**, 444–468.

Rokni, H., Gupta, A., Moore, J., McHugh, M., Bamgbade, B. and Gavaises, M. [2019], 'Purely predictive method for density, compressibility, and expansivity for hydrocarbon mixtures and diesel and jet fuels up to high temperatures and pressures', *Fuel* **236**, 1377–1390.

Rosenfeld, Y. [1977], 'Relation between the transport coefficients and the internal entropy of simple systems', *Phys Rev A (Coll Park)* **15(6)**.

Rowane, A., Gupta, A. and McHugh, Gavaises, M. [2020], 'Experimental and modeling investigations of the phase behavior and densities of diesel + nitrogen mixtures.', *Fuel* **265**.

Salimi, M. and Bahramian, A. [2014], 'The prediction of the speed of sound in hydrocarbon liquids and gases: the peng-robinson equation of state versus saft-back', *Pet Sci Technol* **32(4)**, 409–417.

Salvador, F., Martinez-Lopez, J., Romero, J. and Rosello, M. [2013], 'Computational study of the cavitation phenomenon and its interaction with the turbulence developed in diesel injector nozzles by large eddy simulation (les)', *Math Comput Model* **57(7-8)**, 1656–1662.

Sandia [2023], 'Sandia national laboratories - spray c nozzle geometry', https://ecn.sandia.gov/diesel-spray-combustion/target-condition/spray-c-nozzle-geometry/. Accessed: 01.06.2023.

Sandia National Laboratories - Spray A [2024], https://ecn.sandia.gov/diesel-spray-combustion/target-condition/spray-ab/. Accessed: 01.06.2023.

Santos, E., Shi, J., Gavaises, M., Soteriou, C., Winterbourn, M. and Bauer, W. [2020], 'Investigation of cavitation and air entrainment during pilot injection in real-size multi-hole diesel nozzles.', *Fuel* **263:116746**.

Sato, K. and Saito, Y. [2001], 'Unstable cavitation behavior in circular cylinder orifice flow', *Proceedings of the 4th Int. Symp. on Cavitation, CALTECH* .

Schappals, M., T., B.-N., Langenbach, K., Burger, J. and H., H. [2017], 'Solubility of carbon dioxide in poly(oxymethylene) dimethyl ethers', *J. Chem. Eng. Data* **62(11)**, 4027–4031.

Schmidt, D., Rutland, C., Corradini, M., Roosen, P. and Genge, O. [1999], 'Cavitation in two-dimensional asymmetric nozzles', *SAE paper* **1999-01-0518**.

Schmidt, S. J., Sezal, I. H., Schnerr, G. H. and Talhamer, T. [2008], 'Riemann techniques for the simulation of compressible liquid flows with phase-

transition at all mach numbers - shock and wave dynamics in cavitating 3-d micro and macro systems', *46th AIAA Aerosp. Sci. Meet. Exhib* **January**, pp. 1–24.

Schnabel, R. and Eskow, E. [2006], 'A revised modified cholesky factorization algorithm', *Springer* .

Schnerr, G. and Sauer, J. [2001], 'Physical and numerical modeling of unsteady cavitation dynamics', *4th Int. Conf. Multiph. Flow* **June**, pp. 1–12.

Schnerr, G., Sezal, I. and Schmidt, S. J. [2008], 'Numerical investigation of three-dimensional cloud cavitation with special emphasis on collapse induced shock dynamics', *Phys. Fluids* **20**.

Senecal, P. K., Pomraning, E., Richards, K. J. and Som, S. [2013], 'Grid-convergent spray models for internal combustion engine cfd simulations', *Journal of Energy Resources Technology* **135**(1), 012204.

Sezal, I. H. [2009], Compressible Dynamics of Cavitating 3-D Multi-Phase Flows, PhD dissertation, Technische Universitat Munchen.

Sforzo, B. e. A. [2019], 'Fuel nozzle geometry effects on cavitation and spray behavior at diesel engine conditions.', *Proceedings of the 10th International Symposium on Cavitation (CAV2018)* **90**, 474–480.

Shen, X., Sou, A., Wada, Y. and Ueki, H. [2025], 'Single string cavitation and swirling flow in a nozzle and hollow-cone spray.', *Journal of Fluid Science and Technology* .

Shibata, S., Nishio, S., Sou, A., Akayama, D. and Mashida, M. [2015], 'Evaluation of cavitation in injector nozzle and correlation with liquid atomization', *Journal of Visualization* **18**, 481–492.

Shima, A. [1997], 'Studies on bubble dynamics', *Shock Waves* **7**, pp. 33–42.

Singhal, A., Athavale, M., Li, H. and Jiang, Y. [2002], 'Mathematical basis and validation of the full cavitation model', *Journal in Fluid Energy Transfer, ASME* **124**, pp. 617–624.

Soteriou, C., Andrews, R. and Smith, M. [1995], 'Direct injection diesel sprays and the effect of cavitation and hydraulic flip on atomization', *SAE Technical Paper* **950080**.

Sou, A., Hosokawa, S. and Tomiyama, A. [2007], 'Effects of cavitation in a nozzle on liquid jet atomization', *International Journal of Thermal Sciences* **50**, pp. 3575–3582.

Spiteri, R. and Ruuth, S. [2002], 'A new class of optimal high-order strong-stability- preserving time discretization methods', *SIAM J Numer Anal* **40(2)**, 469–491.

Stavropoulos Vasilakis, E., Rodriguez, C., Kyriazis, N., Malgarinos, I., Koukouvinis, P. and Gavaises, M. [2019], 'A direct forcing immersed boundary method for cavitating flows', *Int J Numer Methods Fluids* **93(10)**, 3092–3130.

Stavrou, M., Bardow, A. and Gross, J. [2016], 'Estimation of the binary interaction parameter kij of the pc-saft equation of state based on pure component parameters using a qspr method', *Ind Eng Chem Res* **47(15)**, 5092–5101.

Streller, J., Krella, A., J., K. and Janicki, W. [2005], 'Towards quantitative assessment of material resistance to cavitation erosion', *Wear* **258**, pp. 604–613.

Strotos, G. e. a. [2014], 'Fuel heating in high-pressure diesel nozzles.', *International Conference Thiesel* .

Sun, Y., Guan, Z. and Hooman, K. [2019], 'Cavitation in diesel fuel injector nozzles and its influence on atomization and spray', *Chemical Engineering & Technology* **42**, pp. 6–29.

Tekawade, A., Sforzo, B., Matusik, K., Fezzaa, K., Kastengren, A. and Powell, C. [2020], 'Time-resolved 3d imaging of two-phase fluid flow inside a steel fuel injector using synchrotron x-ray tomography', *Scientific Reports* **10:8674**, pp. 1–9.

The Economist [2022], https://www.economist.com/special-report/2021/10/27/what-the-paris-agreement-of-2015-meant. Accessed: 01.05.2022.

Tihic, A., Kontogeorgis, G., von Solms, N., Michelsen, M. and Constantinou, L. [2008], 'A predictive group-contribution simplified pc-saft equation of state: application to polymer systems', *Ind Eng Chem Res* **47(15)**, 5092–5101.

Torelli, R. e. a. [2018], 'Evaluation of shot-to-shot in-nozzle flow variations in a heavy- duty diesel injector using real nozzle geometry.', *SAE Int J Fuels Lubr* **11(4)**, 379–396.

Toro, E. [2009], *Riemann Solvers and Numerical Methods for Fluid Dynamics*, Springer.

Trummler, T., Bryngelson, S., Schmidmayer, K., Schmidt, S., Colonius, T. and Adams, N. A. [2020], 'Near-surface dynamics of a gas bubble collapsing above a crevice', *Journal of Fluid Mechanics* **899**, pp. A16.

Trummler, T., Schmidt, S. J. and Adams, N. A. [2021], 'Effect of stand-off distance and spatial resolution on the pressure impact of near-wall vapor bubble collapses', *International Journal of Multiphase Flow* **141**, pp. 1–15.

Tryggvason, G., Scardovelli, R. and Zaleski, S. [2011], *irect Numerical Simulations of Gas–Liquid Multiphase Flows*, Cambridge University Press.

Tumakaka, F. and Sadowski, G. [2004], 'Application of the perturbed-chain saft equation of state to polar systems', *Fluid Phase Equilib* **217(2)**, 233–239.

Tzanetakis, T., Medina, R., Garg, R. and Peng, Q. [2019], 'Durability study of a high pressure common rail fuel injection system using lubricity additive dosed gasoline-like fuel - additional cycle runtime and teardown analysis', *SAE International Journal of Advances and Current Practices in Mobility* **16**, 237–251.

United Nations [1992], 'United nations framework convention on climate change', **url**: https://web.archive.org/web/20050404103328/http://unfccc.int/not_assigned/b/items/1417.php.

van Oostrum, P. [2004], 'Phancyhdr package documentation', **url**: http://texdoc.net/texmf-dist/doc/latex/fancyhdr/fancyhdr.pdf.

Vaz, M., Koukouvinis, P. and Gavaises, M. [2022], 'Numerical simulation of multicomponent diesel fuel spray surrogates using real-fluid thermodynamic modelling', *SAE Technical Paper* .

Vera-Tudela, W., Haefeli, R., Barro, C., Schneider, B. and Boulouchos, K. [2020], 'An experimental study of a very high-pressure diesel injector (up to 5000 bar) by means of optical diagnostics', *Fuel* **275:117933**.

Vidal, A., Kolovos, K., Gold, M., Pearson, R., Koukouvinis, P. and Gavaises, M. [2021], 'Preferential cavitation and friction-induced heating of multi-component diesel fuel surrogates up to 450mpa.', *Int J Heat Mass Transf* **166:120744**.

Vidal, A., Koukouvinis, P. and Gavaises, M. [2020], 'Vapor-liquid equilibrium calculations at specified composition, density and temperature with the perturbed chain statistical associating fluid theory (pc-saft) equation of state', *Fluid Phase Equilib* **521:112661**.

Vidal, A., Rodriguez, C., Koukouvinis, P., Gavaises, M. and McHugh, M. [2018], 'Modelling of diesel fuel properties through its surrogates using perturbed-chain, statistical associating fluid theory', *Int J Engine Res* .

Wang, Q. [2014], 'Multi-oscillations of a bubble in a compressible liquid near a rigid boundary', *Journal of Fluid Mechanics* **745**, 509–536.

Wilson, G. [1969], 'A modified redlich-kwong equation of state, application to general physical data calculations', *65th National AIChE Meeting* **47(15)**, 5092–5101.

Wrona, F., Adamidis, P., Iben, U., Rabenseifner, R. and Munz, C. [2003], 'Dynamic load balancing for the parallel simulation of cavitating flows', *Recent advances in parallel virtual machine and message passing interface. Lecture notes in computer science* **2840**, 545–9.

Wu, Y. e. a. [2011], 'Experimental measurements and equation of state modeling of liquid densities for long-chain n-alkanes at pressures to 265 mpa and temperatures to 523 k', *Fluid Phase Equilib* **311**, 17–24.

Yakubov, S., Maquil, T. and Rung, T. [2014], 'Experience using pressure-based cfd methods for eulereuler simulations of cavitating flows', *Comput. Fluids* **111**, pp. 91–104.

Yan, F., Du, Y. and Liu, C. [2016], 'Effects of injection pressure on cavitation and spray in marine diesel engine', *International Journal of Spray and Combustion Dynamics* **9**, 1–20.

Young, F. [1999], *Cavitation*, Imperial College Press.

Yuan, W. and Schnerr, G. [2003], 'Numerical simulation of two-phase flow in injection nozzles: Interaction of cavitation and external jet formation', *Journal of Fluids Engineering* **125**, pp. 963–969.

Yunfei, M., Yong, P. and Jianmin, Z. [2018], 'Study of cavitation bubble collapse near a wall by the modified lattice boltzmann method', *Water* **26-4**.

Zhang, L., He, Z., Guan, W., Wang, Q. and Som, S. [2018*a*], 'Application of x-ray micro-computed tomography on high-speed cavitating diesel fuel flows', *Int J Heat Mass Transf* **124**, 900–911.

Zhang, L., He, Z., Guan, W., Wang, Q. and Som, S. [2018*b*], 'Simulations on the cavitating flow and corresponding risk of erosion in diesel injector nozzles with double array holes', *Int J Heat Mass Transf* **124**, 900–911.

Zhang, Y. e. a. [2025], 'Experimental study on cavitation pattern and near-field spray characteristics of methanol in the scaled-up fuel injection nozzle.', *Fuel* .

Özgünoğlu, M., Mouokue, G., Oevermann, M. and Bensow, R. E. [2025], 'Numerical investigation of cavitation erosion in high-pressure fuel injector in the presence of surface deviations', *Fuel* .